FUNDAMENTALS OF MATERIAL REMOVAL IN SILICON CARBIDE FOR FREEFORM OPTICS

by

Prithiviraj Shanmugam

A thesis submitted to the faculty of
The University of North Carolina at Charlotte
in partial fulfillment of the requirements
for the degree of Master of Science in
Mechanical Engineering

Charlotte

2019

Approved by:

_____
Dr. Matthew A. Davies

_____
Dr. Christopher J. Evans

_____
Dr. Joseph D. Owen

_____
Dr. Thomas J. Suleski

ABSTRACT

PRITHIVIRAJ SHANMUGAM. Fundamentals of material removal in silicon carbide for freeform optics. (Under the direction of DR. MATTHEW A. DAVIES)

The mechanical and thermal properties offered by Silicon carbide (SiC) make it an ideal material for reflective freeform optics. However, the hardness, brittleness and fracture toughness of the material pose a challenge to manufacturing. The manufacturing process must attain the desired surface finish and form tolerances with the least possible subsurface damage. From the optical fabrication standpoint, two out of the three above-mentioned surface response behaviors are studied in this thesis; surface roughness and subsurface damage. The goal of this research is to grind different grades of SiC under identical sets of parametric conditions and study the surface and subsurface response behaviors. Five different grades of SiC were procured from different suppliers and were ground under identical conditions on a Makino A55 machining center and on an Optisonic 1250x grinding machine with different grinding configurations. The subsurface damage was studied using a recently developed method called MRF spotting. The results of this study add to existing literature on the understanding of the process mechanics in grinding SiC and allow for more effective selection of process parameters to efficiently grind SiC optics while maintaining surface and subsurface integrity. The thesis analyzes the surface mechanics and provides a baseline understanding of the effect of process parameters on surface roughness and subsurface damage. The thesis concludes with preliminary tests conducted to understand surface mechanics in grinding complex optics, starting with test spheres ground with cup grinding wheels.

DEDICATION

I would like to dedicate this work to my parents who have constantly supported me and put me through the best education. I wouldn't be who I am without them. I would also like to dedicate this work to my advisor/mentor, Dr. Matthew A. Davies, who has constantly motivated me and has been a source of inspiration.

ACKNOWLEDGMENTS

I would like to express my sincere gratitude to my mentor and thesis advisor, Professor Matthew A. Davies for his valuable and continuous guidance, dedicated support and encouragement which were elemental in my learning process and in completing my thesis. His continuous encouragement and support helped me develop my knowledge and skills. I would like to extend my thanks to Dr. Joseph Owen and Dr. John Troutman for their technical insights, training and for conducting the initial phase of grinding experiments. I am also grateful to Dr. Christopher J. Evans with whom I have had multiple discussions to understand the standards and metrology aspects of this research and for his insights on SiC grinding and subsurface damage. I thank Dr. Thomas J. Suleski for his insights on mid-spatial frequency errors and his support of my work in the Center for Freeform Optics. I am also thankful to Dr. John Lambropoulos and Dr. Sivan Salzman from University of Rochester for sharing their valuable insights from prior grinding tests on ceramics and subsurface damage estimation.I would like to extend my gratitude to Brian Dutterer for machining necessary components required for the project and also for providing CNC training. I am also thankful to Dr. Hossein Shahinian for training me on the magneto-rheological finishing (MRF) machine. I would also like to thank Nicholas Sizemore, Nicholas Horvath, Clark Hovis and Zachary Reese for the several discussions and assistance. I would like to thank the industries Poco Graphite, Coorstek, AFRL, L3 Optical system and Aperture Optical Sciences for providing us with samples of different grades of silicon carbide for our grinding tests. Special thanks to Poco Graphite, Aperture Optical Science, OptiPro, Eminess Technologies and Scomac

for sharing their insights and experience in conducting our preliminary grinding tests on Silicon carbide. Also, special thanks to Mr. Ed Fess and Mr. Josh Hamilton from OptiPro who helped conduct the second phase of grinding tests.

Finally, I would like to thank the Center for Freeform Optics and its Director, Dr. Jannick Rolland for financial support without which this thesis wouldn't have been possible.

TABLE OF CONTENTS

LIST OF TABLES

LIST OF FIGURES

LIST OF ABBREVIATIONS

SiC	Silicon carbide
CSI	Coherence Scanning Interferometer
SEM	Scanning Electron Microscope
MRR	Material Removal Rate
CVC	Chemical Vapor Composite
CVD	Chemical Vapor Deposited
RB	Reaction bonded
DS	Direct Sintered
Si inf	Silicon infiltrated
Si	Silicon
MRF	Magneto-rheological Finishing
SEI	Secondary Electron Imaging
BEC	Backscatter Electron Imaging – Composition Mode
BET	Backscatter Electron Imaging – Topographical Mode
BES	Backscatter Electron Imaging – Shadow Mode
PSD	Power Spectral Density
NaN	Not-a-Number

PREFACE

This study is a 3-year project on silicon carbide optics fabrication to understand (i) the effect of grinding parameters on the surface finish and subsurface damage, (ii) surface mechanics between the grinding wheel and silicon carbide (SiC) sample, (iii) form based localized interactions to identify optimized set of parameters to produce freeform optics with desirable surface finish and subsurface damage and (iv) the effect of sub-aperture grinding on waviness which may contribute to mid-spatial frequency errors in freeform optics. This thesis will discuss in detail, the experiments conducted on the first phase of the project with a major focus on studying the effect of grinding parameters on surface finish and subsurface integrity. Chapter 1 provides a background on the current understanding of machining SiC. Chapter 2 discusses the grinding setup, process parameters and configurations used for the grinding experiments, the Magneto-Rheological Finishing (MRF) spotting test setup, and the parameters for subsurface damage assessment. The measurement setup and the procedure to assess the surface using a coherence scanning interferometer (CSI) and a scanning electron microscope (SEM) is explained in Chapter 3. Chapter 4 analyzes the results and interprets them with respect to process parameters and grinding configuration. In addition to this, Chapter 4 also discusses the effect of grinding parameters on the spatial frequency content of the ground surface using power spectral density (PSD) calculations. Chapter 5 uses surface roughness measurements of spots on the surfaces generated with MRF to study subsurface damage. In addition, Chapter 5 also critically discusses the validity of the MRF spotting technique by comparing results obtained in different grades of SiC, and it also includes a baseline study to understand interaction between MRF process with two-

phase grades of silicon carbide. The thesis concludes with Chapter 6 discussing directions on possible future work aimed at increased understanding of form-based localized surface and subsurface response characteristics when grinding freeform geometries in silicon carbide.

CHAPTER 1: BACKGROUND AND MOTIVATION

1.1 Introduction

Freeform optics have become a subject of great interest among optical researchers in both academia and in industry. Research has demonstrated that freeform designs in optical systems can enable more compact and unobscured systems which may even be less sensitive to alignment tolerances [1]. Alternatively, performance can be improved for a given package size, ultimately reducing size, weight and potentially also operating power (SWaP reduction) in many optical systems. Examples include three-mirror anastigmat (TMA) designs in telescopes and imaging spectrometers [2]. Reflective mirrors can be fabricated from many materials, but, depending on the application, it may be required that the mirror material have high mechanical and thermal stability. In diffraction limited imaging systems, mechanical and thermal stability are critical. For such systems, there has been increased interest in the use of advanced ceramic materials. Ceramics exhibit high hardness, thermal shock resistance and chemical stability which make them ideal materials for system components that perform in extreme environments. In particular, silicon carbide (SiC) is of great interest for space applications due to its high strength to weight ratio, robustness in harsh environments and relatively high thermal diffusivity and therefore thermal stability. However, the properties that make SiC a good candidate for optical elements pose manufacturing challenges. Due to high hardness with low fracture toughness and high brittleness, it is difficult to machine silicon carbide. First, the machining causes significant dimensional changes in the tool (e.g. grinding tool wear) which causes significant challenges in maintaining overall form. Second, the local interactions between the tool and workpiece can cause significant

fracture and subsequent degradation in surface roughness and subsurface integrity [3]. Poor surface roughness leads to scatter and poor reflectivity and subsurface damage can lead to premature component degradation and potentially even failure. Efficient machining of silicon carbide thus requires an understanding of tool wear rates, a baseline understanding of tool-workpiece interactions at the surface level and an understanding of the material properties of SiC in general. With this, the goal is to choose suitable operating parameters that maximize material removal rate while controlling surface roughness and maintaining subsurface integrity and form.

Due to their versatility and relative speed, commonly used methods for machining freeform surfaces in optical materials are coordinated axis diamond turning, diamond milling and diamond grinding. However, these processes are only viable when there is no rapid wear of diamond tools [4]. Studies in diamond turning [5][6] and diamond milling [7] of silicon carbide indicate that these processes are successful in producing near optical finishes only at lower feed rates and extremely small depths of cut with little usable surface area. The costs involved are prohibitive due to high tool wear. Studies [5][7] suggest that, with increased cutting lengths, the tool undergoes rapid wear due to abrasion and the surface roughness degrades rapidly. These factors affect the surface/subsurface characteristics of the part significantly. Although there is some anecdotal evidence that laser assistance can prolong tool life in single crystal diamond machining of silicon carbide, the process remains a scientific curiosity rather than a practical process for producing optics [8][9]. Thus, diamond grinding, most often followed by a fine finishing process such as polishing remains the only viable process chain for producing optical surfaces in SiC.

During grinding, the diamond grits serve as cutting edges. The bond material that holds the grits wears continuously and exposes new grits during machining as old grains are removed. The literature on grinding of SiC is substantial. However, to our knowledge there is no study on the surface/subsurface response when different grades of silicon carbide are ground under identical parameters. This is the focus of this thesis.

The literature on grinding of silicon carbide shows that the process is viable for producing optics when coupled with a finishing operation to improve surface roughness and correct form. Indeed, in this work we show that under some conditions and with certain grades of SiC, grinding alone can produce surface roughness that might be suitable for some infrared applications. However, to understand and eventually predict the grinding conditions under which suitable surface and subsurface characteristics are obtained, we must first understand the mechanics of the grinding process and the effect of different material grades on that process.

Conventional grinding involves simultaneous workpiece material removal and wear of the grinding wheel to expose new cutting edges. Dressing of the wheel is often required to further expose new cutting edges if grinding along is not sufficient or if material becomes packed around the existing cutting edges. Because SiC is such a hard material – often used to dress grinding wheels in other operations – self dressing during SiC grinding is possible and often desirable. To understand this in more depth we must understand grinding wheel wear.

Conventional grinding wheel wear occurs in three stages [10]. Attritious wear occurs at the individual grit-workpiece level and refers to a dulling of the grits and appearance of wear flats [11]. This dulling of the edges leads to greater forces on the grits

and cause grit fracture or dislodgement. Then at the macroscopic level, forces can become high enough to cause local failure or fracture of the grinding wheel binder resulting in further wheel wear.

In the case of diamond grinding of silicon carbide, some studies suggest that the diamond grits are more susceptible to bond fracture than grain fracture [12]. Hence, these studies suggest that when diamond grinding silicon carbide, wear takes place in two stages: attritious wear and bond fracture. The most commonly used bonds are bronze metal bonds for rough cutting and precision grinding applications and phenolic resin bonds for finishing applications. During attritious wear, as the grits become dull, debris from the grinding process tend to build up between the grits. Also, due to grit or bond fracture, the diamond grains are removed from the bond material. If new grits are not exposed quickly enough, this leads to a decline in the efficiency of the grinding [13]. As stated above, this is overcome by periodically dressing the wheel, thus removing the built-up material and the bond material to exposing fresh grits. The most commonly used dresser when diamond grinding silicon carbide is aluminum oxide. However, silicon carbide sticks are also often used to dress super abrasive wheels such as diamond and CBN wheels. Further investigations in the literature [14][15][16] on dressing have shown that the silicon carbide workpiece itself can act as a dresser. This method of dressing the wheel by the grinding process itself is known as ‘self-dressing’. It was concluded in literature [16] that an increase in depth of cut during the grinding of silicon carbide can enhance self-dressing. Hence, under the right conditions, minimal dressing is often sufficient for grinding ceramics like silicon carbide using diamond wheels.

The major limitation in using grinding process for optics manufacturing is to achieve high material removal rates to lower machining cost while maintaining surface and subsurface integrity. Material properties such as low fracture toughness, high hardness and high brittleness make ceramics challenging to grind. The presence of surface and subsurface cracks can act as stress concentrators and further propagate cracks into the subsurface [17]. Stress concentrations due to existing subsurface damage coupled with further propagation due to low fracture toughness make the material difficult to machine while maintaining surface/subsurface integrity. A better understanding of the surface mechanics and effect of process parameters on surface and subsurface integrity is required to efficiently grind silicon carbide to achieve suitable tolerances in form, waviness and surface roughness while not introducing excessive subsurface damage. Finally, the surface form, waviness, roughness and the subsurface damage produced by the grinding operations determine the requirements for time-consuming post-processing/ polishing. The goal is to choose grinding parameters that minimize the overall production time and cost.

1.2 Surface Mechanics in Grinding

The mechanics of surface generation during grinding of ceramics has been studied throughout the literature. From the standpoint of grit-workpiece interaction, grinding can be viewed as multiple nanoindentation events with a moving indenter. Malkin et. al. [18] studied the abrasive workpiece interaction from the standpoint of indentation fracture mechanics. During an indentation event, cracks develop both radially and laterally as shown in Figure 1a.

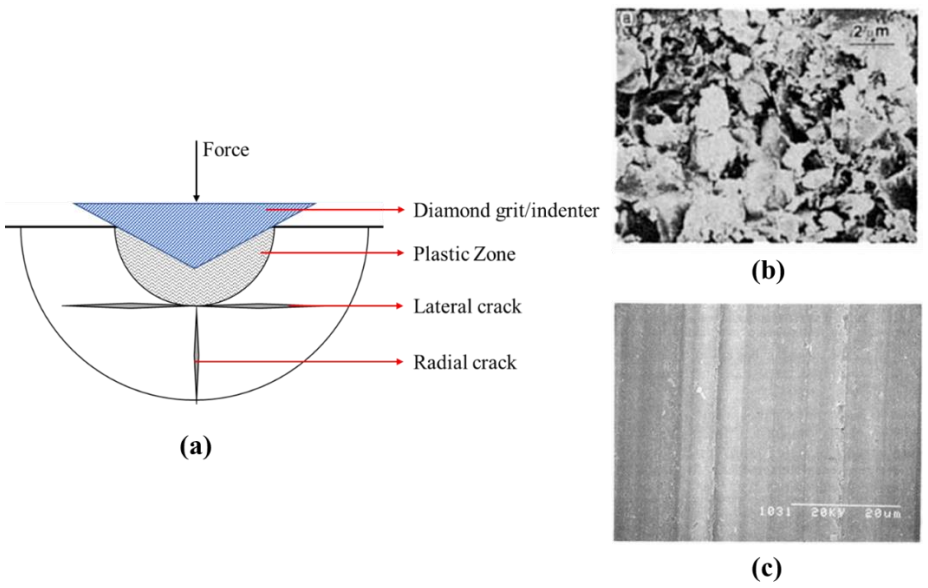

FIGURE 1: (a) Lateral and Radial cracks during indentation,
(b) SEM image of brittle fracture dominated ground surface [19],
(c) SEM image of ductile dominated ground surface [20]

Lateral cracks promote material removal at the surface level and radial cracks promote subsurface damage. Indentation fracture mechanics suggest a critical threshold force below which lateral cracks should be insignificant. This is also explained by plasticity theory [5] which suggests that the magnitude of hydrostatic pressure between the indenter and workpiece determines the extent of ductile deformation before fracture. The state of stress under a grit is also dependent on the machine stiffness, grit geometry and cutting direction.

Most literature discuss grinding mechanisms as a combination of brittle fracture and ductile deformation. Figures 1b and 1c provide examples of SEM images of brittle fractured and ductile deformation dominated surfaces respectively from literature [19][20]. To study the brittle fracture occurring in grinding, Malkin et. al. [18] performed single point and multi point scratch tests in ceramics and glasses. The surface response

with increasing load was characterized by observed crack lengths in silicon nitrate and glass. Though this study provided insights into the mechanics on the surface level, it was not applicable for realistic grinding operations because the tests were conducted using known grit geometries at fixed depth of cut. It did not account for factors such as grit geometry and orientation, spacing between grits on the wheel, variation in temperature between surface and wheel, etc. Similar tests were also conducted by Kirchner [21] where single and multi-point grit surface interactions were studied using diamond grits mounted on the periphery of a wheel. The number of grits interacting with the surface during the multi-grit test was reduced to study the surface response due to individual, randomly oriented grits interacting with the surface. It was concluded that, during multi-grit interaction, an increase in the number of grits led to a decrease in the load experienced by the individual grits during grinding. Hence for constant load, the average crack length was reduced in multi-grit interaction compared to that of single grit interaction. The interactions between neighboring grits has not been explored much in detail in the literature for grinding ceramics.

Experiments conducted by Bifano et. al. [20] studies the material removal mechanisms as brittle mechanism, caused by fracture propagation, and ductile mechanism, caused by plastic flow. Alternative theories also exist in the literature to explain the material removal mechanisms during grinding when producing smooth surfaces. Bi Zhang et. al. [22] conducted experiments on single point diamond grinding tool and a diamond grinding wheel to grind hot-pressed silicon nitride and hot-pressed alumina ceramics. It was reported that, during grinding at smaller depth of cut, under certain parameters, the surface mechanics was dominated by pulverization. Pulverization

is characterized by the formation of a powder region compacted under high pressure. The researchers hypothesize that this compaction of material under high pressure can produce a smooth surface. Previously, smooth surfaces were presumed to be formed by ductile material deformation. According to this theory, the shear stress between the wheel surface and workpiece causes dislocation motion along certain slip planes. With increasing shear stress between the wheel and workpiece, bond rupture occurs on the workpiece surface resulting in pulverization of the material. The hydrostatic pressure between the wheel and workpiece surface recompacts the pulverized material to form the smooth powder region.

With respect to silicon carbide, much research has been done to study surface and subsurface level interactions. Agarwal and Rao [23] studied the forces from high material removal rate (MRR) grinding in a direct sintered silicon carbide. It was concluded that material removal at high MRR occurred by microfracture and lateral cracking along grain boundaries. It was also observed that the surface roughness during high material removal rate grinding did not change significantly as specific MRR increased. Agarwal also studied [24] the effect of different parameters such as depth of cut, feed rate, grit size and grit density on the surface integrity of the ground silicon carbide sample. Optimized sets of parameters were discussed by adopting a genetic algorithm to achieve high material removal rate while maintaining surface integrity.

1.3 Modeling and Prediction of the Grinding Process

While of critical importance, empirical studies to identify grinding parameters are time consuming and expensive. Thus, much research has been dedicated towards analytical modelling of grinding process and predicting surface quality. During grinding,

the diamond grits which are assumed to be randomly placed over the periphery of the wheel interact with the surface being ground forming randomly distributed grooves. The randomness in the size and location of the diamond grits makes it challenging to characterize the wheel for the model. Agarwal and Rao [25] modeled the undeformed chip thickness generated during a grit-workpiece interaction. Using the undeformed chip thickness model along with other data such as wheel microstructure, kinematic and dynamic grinding conditions, and material properties, a more realistic model capturing the effect of overlapping of grooves was developed. The advantage of this model was that it was able to incorporate more process and wheel parameters and predict the effects of workpiece and wheel speeds. With respect to silicon carbide, an attempt was made to study the grinding performance using a new chip thickness model [26]. An existing chip thickness model based on a random distribution of grain protrusion heights was considered. This base model assumed the transverse shape of the groove to be triangular. The new method included the elastic properties of wheel and workpiece to account for the deflection in the contact zone to more accurately predict the contact length. It was concluded that the prediction from this new model was more accurate than the base model.

1.4 Subsurface Damage Analysis

The second aspect of this thesis is to characterize subsurface damage (SSD) in the grinding of silicon carbide. Measurements of SSD help to quantify the quality of grinding process and can also be linked to the reliability and lifetime of the ground optical components. Several techniques have been adopted throughout the literature to measure SSD in ceramics. A common method is to expose the subsurface damage using chemical

etchants. This method was used by Zhou et. al. [27] in which different types of glass were ground using different parameters and etched using hydrofluoric (HF) acid solutions of various concentrations to reveal subsurface cracks. Following the etching process, a steel ball was used to polish a dimple in each etched region and the surface was observed under an optical microscope and a scanning electron microscope (SEM). The variation in damage was observed along the rim of the dimple, which essentially formed a taper section. The SSD depths were then calculated by measuring the distance from rim where the damage vanished and estimating depth from the slope of the surface. It was concluded that this method was suitable to estimate subsurface damage as long as the samples were not over-etched. This is an example of a destructive technique. However, silicon carbide is chemically inert, making it a challenging task to identify a suitable etchant solution for room temperature conditions.

Xu et. al. [28] used a bonded sectioning technique to study subsurface damage in ceramics. Two pieces of alumina were used as test samples. The samples were polished on one side and the polished faces were bonded together with a thin layer of superglue. The interface of the bonded samples was then ground, and the samples were separated by melting the glue. After cleaning, the polished surfaces were coated with gold and viewed using a Nomarski microscope to study SSD.

Some researchers have also attempted to model and predict subsurface damage in grinding. Zhang et. al. [29] studied SSD in grinding silicon nitride, alumina and silicon carbide. It was proposed that subsurface damage was a function of material properties, grinding conditions, grinding wheel specifications, wheel truing and dressing conditions, and the brittleness of the material. Brittleness was defined as the ratio of hardness to

toughness of the material under test. The normal force from grinding was correlated to the subsurface damage, and an analytical model was developed which predicted the subsurface damage depth as a function of aforementioned parameters. It was found that the model was in good agreement with the experimental results in [29].

In a study conducted by Lambropoulos et. al. [30], a method similar to ball dimpling, as discussed before, was used. Instead of using a steel ball to polish and penetrate through the ground surface, the magneto-rheological finishing (MRF) process was used to penetrate the surface by generating a spot/dimple. Based on surface measurements at the base of the spots, a correlation was made between the subsurface damage depth and the peak to valley roughness (Rz). This method has the practical significance that the subsurface damage height along with its statistical variance can be estimated directly from the peak to valley roughness values. Shafrir et. al. [31][32] further studied the concept of using the MRF spotting technique to study subsurface damage in aluminum oxynitride (ALON), polycrystalline alumina (PCA) and chemical vapor deposited (CVD) silicon carbide. In this work, Sharfir et. al. characterized subsurface damage by studying the evolution of peak to valley surface roughness parameters at the base of the spots. Thus far, this method has been tested only in CVD grade SiC. This thesis applies this method to estimate subsurface damage across different grades of silicon carbide by studying the evolution of average roughness (Sa), RMS roughness (Sq) and peak to valley roughness (Sz) at the base of spots of varying depths.

1.5. Grades of silicon carbide

We believe this thesis is the first study to examine the surface and subsurface characteristics of different grades of SiC ground under a range of identical conditions.

This is important because silicon carbide grades vary significantly in their mechanical properties and subsequently in their response to grinding. The properties of SiC depend on the method of manufacturing of the grade. Hence, it is essential to have an overall understanding of the surface mechanics in grinding different grades of silicon carbide to effectively control the process parameters to achieve high material removal rates while maintaining surface integrity. This thesis investigates the effect of machining parameters on surface and subsurface features in different grades of silicon carbide under the same grinding conditions.

The crystal structure of silicon carbide can be classified as α-type (hexagonal close packed structure) and β-type (face centered cubic structure). Most grades used for the manufacture of optical components are polycrystalline grades combining both α- and β-type SiC [33]. The majority of silicon carbide samples used for this thesis were procured from two different suppliers, Poco Graphite and CoorsTek. The chemical vapor deposited (CVD) and silicon infiltrated (Si Inf) grades were produced by Poco Graphite. The grades procured from Coorstek included CVD, reaction bonded (RB) and direct sintered (DS). Reaction bonded was also procured from L3 Optical Systems. Chemical vapor composite (CVC) SiC was procured from Trex Enterprises through Aperture Optical Sciences.

1.5.1 Chemically Converted Silicon Carbide

A chemical conversion process that converts graphite to silicon carbide was developed by Poco Graphite to manufacture base SiC optical substrates. These substrates are further processed by Poco Graphite to produce different grades. This process starts with graphite being machined to near net shape. The graphite part is then chemically

converted to silicon carbide by exposing it to silicon carrying gases such as silicon monoxide gas at high temperatures (1500° C). The silicon monoxide is produced using a mixture of high purity silica and carbon powders [34]. The chemically converted silicon carbide serves as the base material for Poco Graphite and is subjected to other processes to produce different grades of silicon carbide.

1.5.2 Chemical Vapor Deposited Silicon Carbide

This grade is one of the most common grades used for optical applications. The grade is usually used as a cladding on a substrate material of a different grade. After machining the substrate material to near net shape, layers of silicon carbide are deposited using chemical vapor deposition. The CVD layer is limited to a total thickness of approximately 100 to 200 μm. The major factors contributing to this limitation are uniformity of CVD growth across the whole surface area and the adhesion between the coating and the substrate [35][36]. CVD grade is a 100% pure β-type silicon carbide [33]. Due to the purity, homogeneity and material properties, grinding and polishing of the grade can produce very low rms roughness of less than 5 Å [37].

1.5.3 Silicon Infiltrated Silicon Carbide

This grade is manufactured by Poco Graphite. After the base material is prepared by the chemical conversion process, the sample is exposed to molten silicon which then fills or infiltrates the porous region in the material. This process densifies the sample [38]. The process improves the efficiency of the CVD coating process. However, the material does not respond well to grinding which tends to pull out silicon or silicon carbide grains from the surface, increasing the surface roughness and potentially causing surface and subsurface fracture.

1.5.4 Reaction Bonded Silicon Carbide

This grade is manufactured by Coostek and L3 Optical Systems. This is also known as siliconized silicon carbide (SiSiC). This is very similar to the silicon infiltrated grade discussed above. Instead of chemically converted silicon carbide, a block of graphite is machined to near net shape and then directly treated with molted silicon. The graphite reacts with silicon to form silicon carbide and in parallel, the molten silicon also fills the porous regions. The material properties depend on the ratio of composition of silicon and silicon carbide in the final material, and on the grain size of silicon carbide.

1.5.5 Direct Sintered Silicon carbide

This grade is also manufactured by Coorstek. This grade is prepared by a direct sintering process converting powdered silicon carbide to a near net shape silicon carbide blank. Due to the method of manufacturing, this grade has higher hardness and thermal shock resistance that is comparable to that of reaction bonded grade.

1.5.6 Chemical Vapor Composite (CVC)

This grade was prepared by Fantom Materials which was formerly known as Trex Enterprises. CVC SiC has material properties similar to those of the CVD grade. The manufacturing process involves the introduction of high purity silicon carbide fibers into the chemical vapor stream during chemical vapor deposition. These particles in the stream act as nucleation sites which alter the microstructure of the material [39]. Trex [39] has reported that an RMS surface roughness of 0.9 Å was achieved in CVC SiC after polishing.

This chapter summarized the major research on surface mechanics during grinding ceramics, and experimental study and theoretical predictions on surface

response to process parameters. It also discussed the different methods used to study subsurface damage depth in ceramics. The major focus of this thesis is to study the surface and subsurface response of SiC to grinding. We believe this thesis is the first study on the grinding of different grades of silicon carbide under identical conditions. The surface is studied using Coherence Scanning Interferometry (CSI) and Scanning Electron Microscopy (SEM). The CSI measurements are analyzed using surface roughness maps, waviness maps and power spectral density (PSD) plots. The definition of mid-spatial frequency is not well defined and is ambiguous in the literature [40]. Since the effect of process parameters on surface and subsurface response are studied from the standpoint of large-scale optics fabrication, the waviness from the machine errors and the stepovers during grinding are considered to be in the mid-spatial frequency regime for this thesis. Hence, the terms, “waviness” and “mid-spatial frequency” are used interchangeably throughout this thesis. In addition, the MRF spotting technique is used to study the subsurface damage across the different grades of SiC.

The concept of surface integrity has been broadly defined in literature and there has been several discussions in understanding surface integrity problems and how to characterize them [41] [19]. The key to understanding the surface integrity is to identify the underlying “surface integrity problem” for the process/component under study. With regard to this thesis, the term surface integrity is used to describe both the surface characteristics and the subsurface characteristics that are expected to affect the performance of the optical component. For grinding of a material like SiC, the surface integrity is often compromised by brittle fractures in the near surface which may or may not propagate all the way to the top surface and affect surface roughness. However,

because there is clearly both ductile and brittle deformation in finish grinding of SiC, other types of surface and subsurface modification that affect the crystal structure such as dislocation generation and propagation, and the generation of residual stresses are also of interest. Further, in two-phase materials, the problem is even more complex in that the different phases may undergo different mechanical removal mechanisms. For example, in silicon infiltrated silicon carbide, it can clearly be seen that the silicon may undergo a ductile deformation simultaneous with brittle fracture occurring in the silicon carbide. Grain pull out also affects both the surface and subsurface and hence the surface integrity. While the SEM can reveal some other aspects of the surface and subsurface characteristics, the MRF spotting technique is most well suited to revealing subsurface fracture in single phase grades of SiC. Based on this background, when the term "subsurface damage" is used in this thesis it mainly refers to the presence of brittle fracture, but we acknowledge that there are other forms of subsurface damage present that we cannot measure with the techniques available to us. A good direction for future work would be to apply other techniques to characterize other aspects of the subsurface in SiC grinding.

The next chapter details the setups and procedures used to conduct the experiments. Chapter 2 describes the machines and the process parameters used to conduct the surface and subsurface study. The chapter also discusses the theory behind the MRF spotting technique to estimate subsurface damage depth.

CHAPTER 2: EXPERIMENTAL SETUP AND PROCEDURE

2.1 Introduction

This chapter focusses on the selection of grinding parameters, the grinding setups in the Makino A55 and the Optisonic 1250X, and the procedures used for grinding tests. It also includes the setup and procedure for conducting MRF spotting technique to study subsurface damage.

2.2 Grinding Process, Sample and Wheel Specifications

The samples were ground using a Makino A55 machining center and an Optisonic 1250X grinding machine. The grades used for the experiments on the Makino A55 include CVC, CVD, silicon infiltrated (Poco Graphite trade name: SUPERSIC-SI) and direct sintered. The grades used for the experiments on the Optisonic 1250x include CVD and reaction bonded. The samples were obtained from Poco Graphite, Coorstek Inc., Aperture Optical Sciences and L3 optics. The sample dimensions varied between 50 mm and 76 mm in diameter and between 5 mm and 15 mm in thickness.

Based on a comprehensive literature survey and after extensive discussions with Optipro, Aperture Optical Sciences, the University of Rochester and Eminess Technologies, the process parameters were classified into 3 categories, Rough, Medium and Finish as shown in Table 1. For the three different classifications, the wheel specifications were varied in mesh size of the diamond grits and the bond materials for holding the grits. These specifications are shown in Table 2 and are discussed as per US wheel specifications.

TABLE 1. Grinding Experiment Parameters for raster configuration

Mode of grinding	Grit Size in Mesh	Grit Size in µm	Feed (mm/min)	Step (mm/pass)	Depth (mm)
Rough	320	40	1000	0.5	0.1
Medium	600	10-20	1000	0.2	0.02
Finish (Makino A55)	6000	2-4	100	0.2	0.02
Finish (Optisonic 1250X)	6000	2-4	100	0.05	0.02

TABLE 2. Grinding Wheel Specifications

Mode of grinding	Arbor Size	Grit Size (Mesh)	Grit Size (Microns)	Bond type
Roughing		320	40	Metal
Medium	0.5"	600	10-20	Metal
Fine		6000	2-4	Copper-Resin / Resin

Tables 1 and 2 define the identical sets of parameters used to the surface and subsurface damage across different grades of silicon carbide. From an industrial standpoint, this classification also provides information on the effect of different grades of SiC on the surface roughness obtained in finish grinding operations before proceeding towards other post-processing like polishing. Other specifications for the grinding wheels include the wheel diameter, the bond grade and the grit concentration number. The bond grade provides a relative indication of the strength or hardness of the bond. The grit concentration number is based upon a proportional scale with a value of 100 corresponding to 4.4 carats of abrasive content per cubic centimeter of bond material. In terms of volume percentage, the concentration number divided by four gives the volumetric percentage of grit in the bond material. For example, a concentration number

of 100 would refer to 25% grit concentration by volume [42]. The grinding wheels used for the experiments were acquired from Scomac Inc. and Eminess Technologies. The rough and medium wheels from Scomac were 2-inch in diameter with a metal bond grade 'N' and the finish wheels had copper-resin bond grade 'R'. All wheels from Scomac had a grit concentration number of 75. The wheels acquired from Eminess Technologies were 1-inch in diameter with a bond grade of 'N' for all wheels. The grit concentration numbers were 75 for the rough and medium (metal bond), and 100 for the finish (resin bond) wheels. Both the Scomac and Eminess wheels had flat profiles. The wheels were dressed using Alumina oxide dressing sticks using the same parameters as used for the grinding process (discussed in Table 1).

2.3 Coolant

The surface interactions between the workpiece and grinding wheel generates tremendous amount of heat. Lack of thermal equilibrium at higher temperatures could result in adverse effects such as adhesion, tribo-chemical reactions, rapid wheel wear, thermal damage to the wheel and workpiece causing workpiece burn, and enhanced abrasion due to interactions between debris and work material [13]. These factors adversely affect the life time of the grinding wheel, the work material as well as the surface finish of the final product. All these factors are taken into consideration in selecting coolant and coolant configuration for the grinding tests. The primary functions of the coolant during grinding are dissipation of heat, cleaning debris off the active zone and reduction in friction [43]. Different coolants and different modes of coolant delivery have been explored and studied in the literature [43][44]. The experiments conducted in

this thesis used water soluble coolants with a flood configuration in both the Makino A55 and the Optisonic 1250X grinding systems.

2.4 Grinding Experiments on the Makino A55

2.4.1 Makino A55 Machining Center

The first set of experiments were done on a Makino A55. The Makino A55 used for these grinding tests is located in Duke Centennial Hall of University of North Carolina at Charlotte. This is a 3-axis horizontal milling machine with three linear axes (X-Y-Z). The machine has an indexable rotary pallet in the B-axis to hold the workpiece. The main spindle (C-axis) has a maximum speed of 20000 rpm.

2.4.2 Coolant system

As aforementioned, the selection of coolant has a direct effect on the mechanical, thermal and chemical stresses imparted on both the workpiece and tool. For the preliminary study, the default coolant used for Makino A55 in regular operation was used for conducting the grinding tests. The coolant used was Hysol MB 50, a water-soluble oil-based coolant with a concentration of 5%. The coolant system has a set of nozzles mounted around the spindle as shown in Figure 2. The coolant jets are directed towards the grinding wheel flooding the active zone between the grinding wheel and workpiece surface. This ensures that the debris generated during the grinding process is continuously flushed while simultaneously controlling the temperature and the lubrication at the active zone.

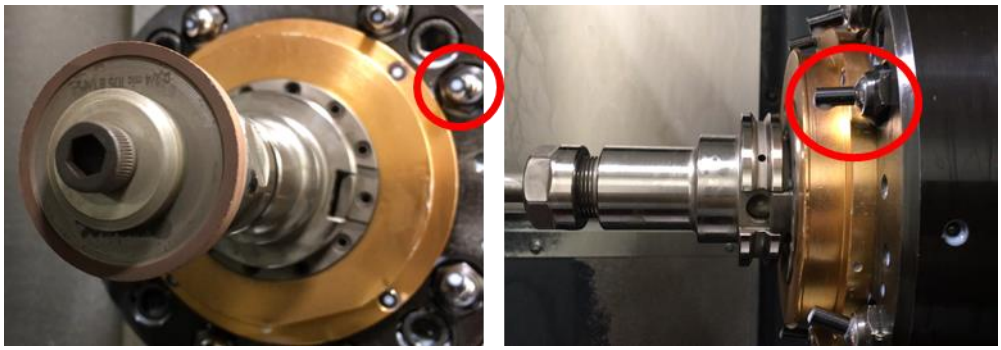

FIGURE 2: Coolant system setup (Red circles indicate the nozzles)

2.4.3 Experimental Setup and Grinding Procedure

The different grades ground on the Makino A55 were silicon infiltrated (Si inf), direct sintered (DS), chemical vapor deposited (CVD) and chemical vapor composite (CVC). The workpiece for each grinding test was waxed to a metal plate and mounted vertically on the indexable pallet in the machine. The grinding wheel was mounted on to an arbor and the arbor was mounted onto the main spindle. The machining was done by raster grinding with the feed along the Z direction and step over along Y direction (as shown in Figure 3) using parameters mentioned in Table 1. Figure 3 shows the setup in Makino A55 and the grinding process. After grinding each sample, the grinding wheels were dressed using aluminum oxide dressing sticks. The dressing process was done by mounting the dressing stick and rastering the grinding wheel against the dressing stick using parameters corresponding to the grit size as mentioned in Table 1.

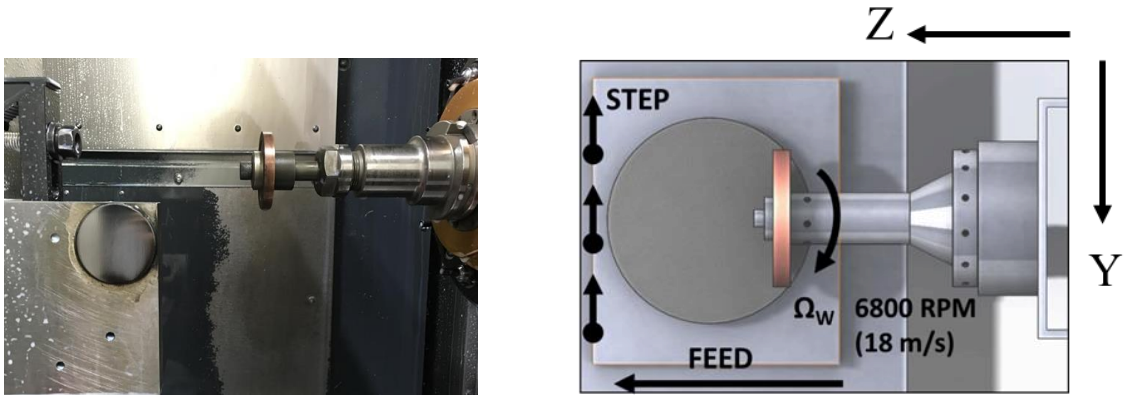

(a) (b)

FIGURE 3: (a) Grinding setup in Makino A55. (b) Grinding process representation

All the above-mentioned grades were ground using the rough, medium and finish parameters as mentioned in Table 1 except CVD. The thickness of the CVD layer on the samples was between 70 µm and 100 µm. Due to this limitation, the grinding parameters were confined to the finish parameters in Table 1. Multiple raster passes were made using the finish parameters to remove the tilt. A final finish pass was then taken to obtain the final surface for analysis. After the grinding tests were completed, the samples were heated to melt the wax and removed from the metal base. The samples were then rinsed with acetone and ethyl alcohol.

2.5 Grinding Experiments on Optisonic 1250X

2.5.1 Optisonic 1250X Grinding Machine

The second set of grinding experiments were conducted on the Optisonic 1250X. The machine used for this phase of tests is located at Optipro Systems, LLC, Ontario, NY, USA. It is a 5-axis grinding machine with three linear axes (X-Y-Z) and two rotary axes (B-C). The main spindle (B-Axis) has a maximum speed of 18000 rpm and the C-

spindle has a maximum speed of 200 rpm. The machine can perform coordinated axis machining with all axes engaged simultaneously.

2.5.2 Coolant System:

The grinding tests conducted on the Optisonic 1250X also used a flood coolant system. The coolant used was Ultracool 2000, a water-soluble, water based synthetic coolant developed by OptiPro for optical fabrication. The coolant was used at 10% concentration. Before the grinding operation, the coolant was circulated through the system until the temperature of the coolant reached 71° F. The machine used a built-in filtration system to remove the grinding debris from coolant during the process. The concentration of the coolant fluid was checked periodically with a viscometer and water or coolant was added periodically to maintain the concentration. The coolant was pumped into the grinding area and the coolant jets were manually directed using a series of loc-line hoses as shown in Figure 4. Two loc-lines were directed towards the interface between the grinding wheel and workpiece surface, and two loc-lines were directed towards the grinding wheel.

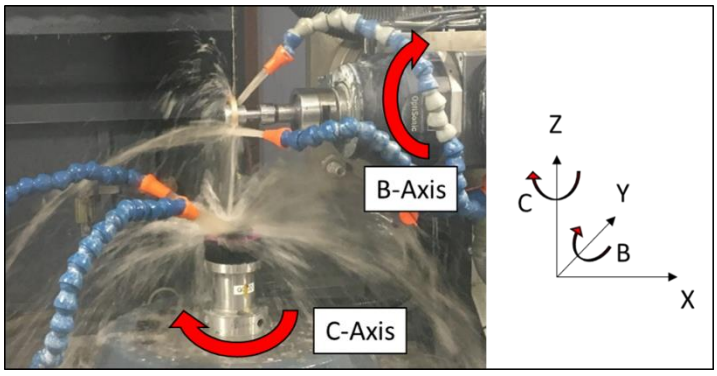

FIGURE 4: Flood cooling system in Optisonic 1250X

2.5.3 Experimental Setup and Grinding Procedure

Raster grinding was performed on direct sintered (DS), chemical vapor deposited (CVD), silicon infiltrated (Si inf) and reaction bonded (RB) grades of SiC. Along with the raster tests using parameters from Table 1, spiral grinding tests were also conducted with the workpiece rotating at a constant speed of 100 rpm and a feed rate of 1 mm/min. Also, ultrasonic grinding was tested in raster mode using parameters from Table 2 and spiral mode using the above-mentioned workpiece rotation speed and feed rate. Table 3 summarizes the parameters used for spiral grinding configuration.

TABLE 3. Grinding experiment parameters for the spiral configuration

Mode of grinding	Grit Size in Mesh	Grit Size in µm	Feed (mm/min)	Workpiece rotation (RPM)	Depth (mm)
Rough	320	40	1	100	0.1
Medium	600	10-20	1	100	0.02
Finish	6000	2-4	5	100	0.005

The grinding wheel was mounted to the arbor and the arbor was mounted on the B-axis main spindle as shown in Figure 4. The workpiece was mounted on the C-axis spindle using a vacuum chuck and the workpiece was held with a vacuum pressure of 25 inches of Hg (≈ 85 kPa). After grinding, the samples were removed from the vacuum chuck and rinsed with ethyl alcohol. The wheels were dressed before starting the next test as shown in Figure 5 using aforementioned procedure with the parameters from Table 2.

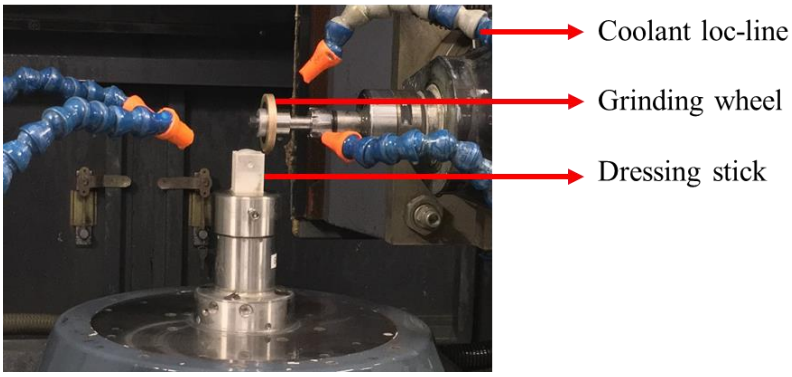

FIGURE 5: Dressing of wheel in Optisonic 1250X

The vacuum chuck used in the initial tests on the Optisonic 1250X supported the workpiece only on the periphery. Hence during the grinding process, the resultant of the vacuum force and grinding forces caused the workpiece to deflect. As a result, the tests performed using a set depth of cut showed a reduced depth of cut in the unsupported regions, indicating a continuous change in the depth of cut during the process. Thus, the vacuum chuck was redesigned to avoid this deflection. The new design supported the workpiece better and reduced grinding induced deflections. The old and new design of the vacuum chuck are shown in Figure 6.

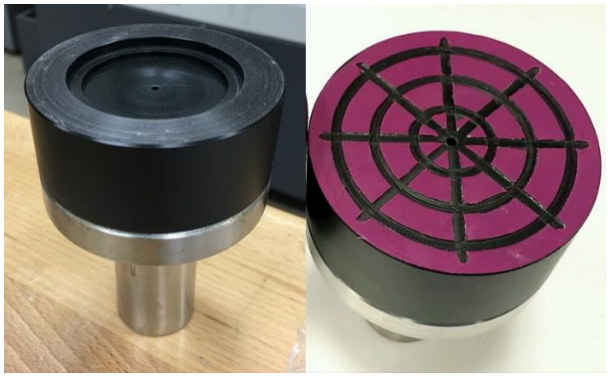

(a) (b)

FIGURE 6: (a) Initial chuck design. (b) Final chuck design

In the earlier tests in Makino A55, only finish passes were performed on the CVD SiC. In the Optisonic 1250X tests, the CVD grade was ground with medium parameters on one side and finish parameters on the other side of the sample. The samples used for these tests were of different diameters. The 2-inch and 3-inch samples were raster ground completely in one cycle using 2-inch wheels. However, when using 1-inch wheels on 3-inch samples, the diameter of the sample was larger than the arbor length limiting reach and access to the whole surface. Thus, half of the sample was raster ground and then rotated by 180 degrees to grind the other half.

2.6 Subsurface Assessment Using Magneto-Rheological Finishing (MRF) Spotting Technique

2.6.1 Introduction:

Production of a quality optic requires the control of surface integrity. Surface integrity is a broad term as discussed in chapter 1, but here we refer mainly to surface roughness parameters and the presence of subsurface damage including machining induced residual stresses and subsurface damage caused by brittle fracture. These are

critical parameters to control in order to produce a high-quality optic. Subsurface damage is difficult to assess and is an important parameter that affects the structural integrity of the optic being ground. Chapter 1 discussed several techniques studied through literature to determine subsurface damage. In this thesis, the subsurface damage is studied using an MRF spotting technique. This method was originally proposed by Shafrir et. al. [32] and tested in CVD grade silicon carbide and in other ceramic materials including aluminum oxynitride (ALON) and Polycrystalline Alumina (PCA). In this thesis, this method is studied extensively and applied to different grades of silicon carbide. This method correlates the evolution of the roughness in at the base of MRF spots, which vary in depths, to assess subsurface damage. Its ability to evaluate subsurface damage from the grinding process is critically assessed and indeed we conclude that while it may be useful in some grades of SiC, it is not useable in others.

2.6.2 Magneto-rheological finishing process

The Magneto-rheological finishing (MRF) is a sub-aperture polishing process used commercially for post-processing of optical surfaces and is able to correct form, waviness and roughness. Figure 7(a) [45] shows the main components of the MRF setup and the process. The fluid is a combination of abrasives, solvents and carbonyl iron particles along with emulsifying agents to stabilize the mixture. Because the carbonyl iron particles are magnetic, the viscosity of the fluid is affected by a magnetic field. The changing viscosity and the presence of abrasive particles in the fluid are used to remove material from the surface by MRF polishing.

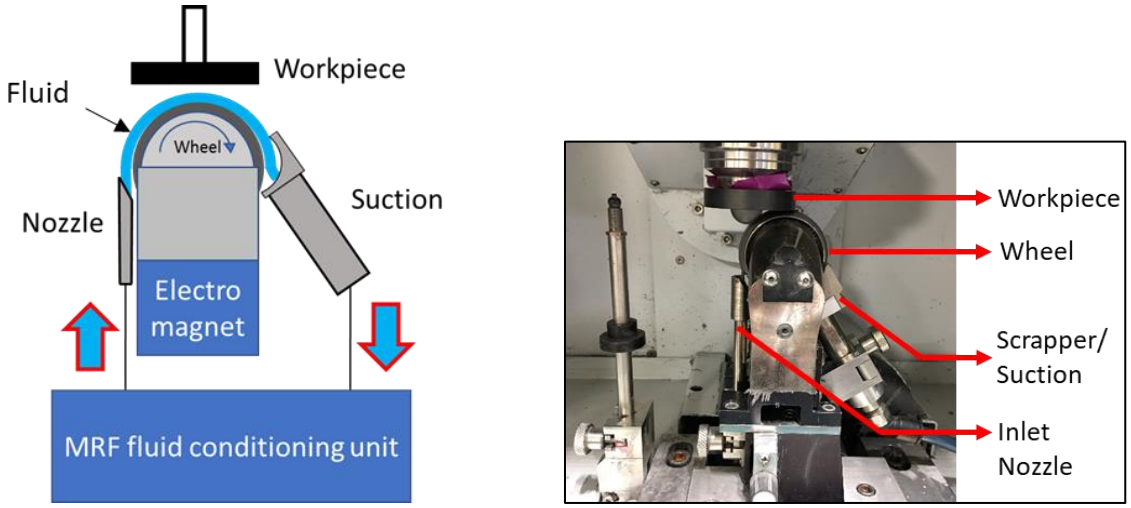

(a) (b)

FIGURE 7: (a) Basic components of MRF machine and MRF polishing process (modified from [45]) (b) QED Q22 – XE CNC MRF machine

The MRF process proceeds as follows. The fluid exits the nozzle and is delivered to the wheel. The electromagnet generates the magnetic field that is concentrated in the gap between the wheel and workpiece. When the fluid enters the magnetic field, its viscosity increases. The fluid becomes a tightly packed ribbon which moves over the rotating wheel and returns into the fluid conditioning unit. The magnetic iron particles in the ribbon are attracted towards the wheel surface while the non-magnetic part of the fluid containing the abrasives and water are pushed away from the wheel forming a thin layer between the bulk fluid and the workpiece. As the workpiece comes in contact with the ribbon, the abrasive particles remove material and thus the surface is polished. With the wheel speed and pump speed constant, the amount of material removed becomes a function of ribbon height, depth of penetration and dwell time at each position.

2.6.3 QED Q22-XE MRF Machine

MRF spotting was performed on a QED Q22-XE, located in Duke Centennial Hall at the University of North Carolina at Charlotte, Charlotte, NC, USA. Figure 6(b) shows the MRF setup on the QED Q22-XE. The MRF fluid used was D10, a diamond based commercial product of QED which consisted of an aqueous mixture of non-magnetic sub-micrometer sized diamond abrasives, magnetic carbonyl iron, water and stabilizers [32]. The parameters such as depth of penetration, spotting time, wheel speed, pump speed and orientation of the workpiece with respect to the MRF wheel can be adjusted through a software interface in the machine.

2.6.4 Theory of SSD Estimation Using MRF Spotting Technique

The MRF spotting technique is based on the work of Shafrir and Lambropoulos [32]. According to these researchers, the subsurface damage depth can be estimated by using MRF to polish spots of varying depths into samples. The hypothesis is that the MRF process only reveals underlying damage without changing the surface or introducing additional subsurface damage. To make a quantitative assessment of SSD the roughness parameters are measured at the base of the spots and the evolution of surface roughness as a function of spot depth is used to estimate subsurface damage. The hypothesis is that the roughness parameters will decrease with depth from those of the ground surface and approach some reduced limiting value. Beyond this point, any change in roughness values is a signature of the grain level interactions between the MRF process and silicon carbide, and also the effect of unidirectional fluid flow on the sample surface. We demonstrate the technique with a ground CVC SiC sample. In Figure 8, the SEM images of the surface at the base of 1-minute, 2-minute and 3-minute spots reveal,

qualitatively, the surface structure at the bottom of the spots at different depths. Figure 9 shows the corresponding change in surface roughness values with varying spotting time (and hence depth) in the same sample. The roughness values presented in figure 8 and 9 were acquired using CSI with 20x objective (Field of View: 418 µm x 418 µm) and after processing the data with a 4th order form removal and an 80 µm high pass Gaussian filter.

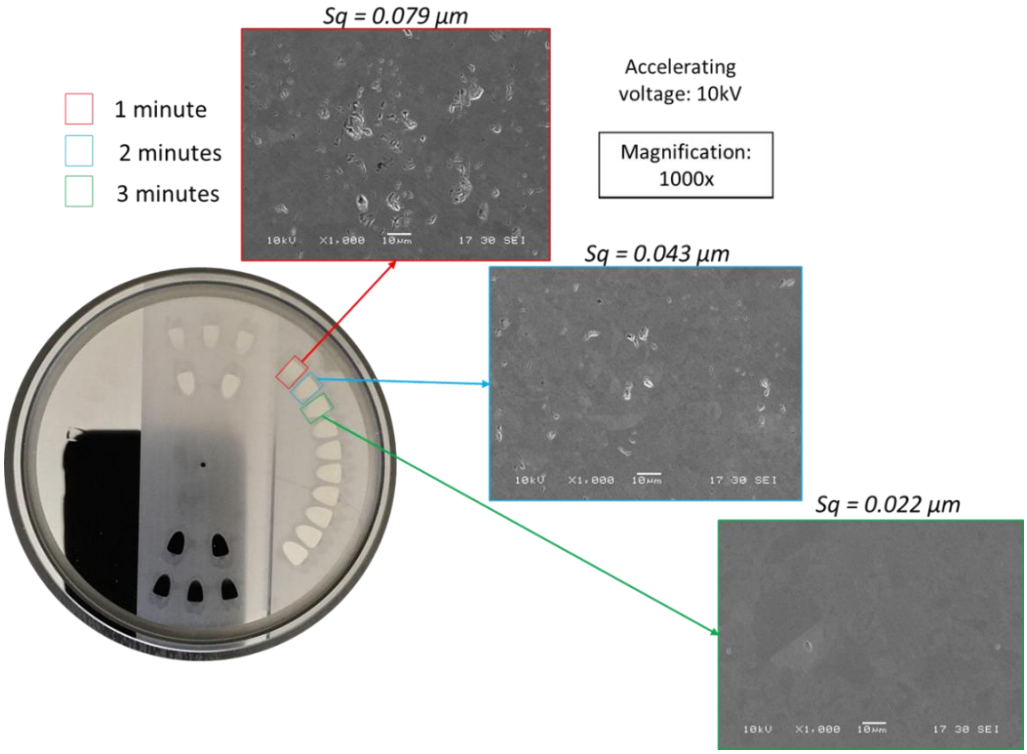

FIGURE 8: Evolution of surface damage and surface roughness with spotting time.

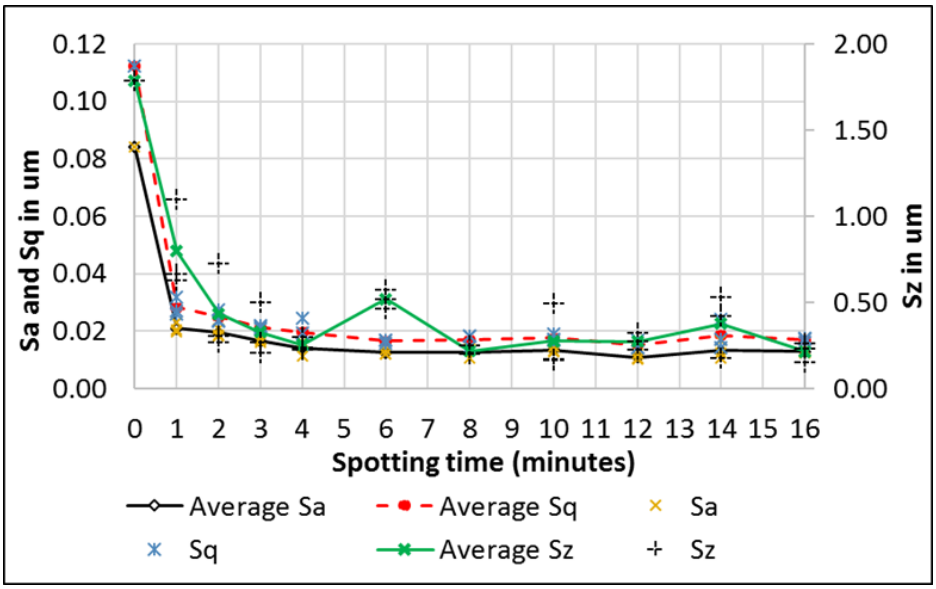

FIGURE 9: Evolution of roughness values with spotting time in CVC grade SiC.

The roughness values initially decease rapidly but then reach a stable value after an 8-minute spotting time. As per the aforementioned theory, the spot height corresponding to this time gives the approximate estimate of the subsurface damage. There are two major assumptions associated with the technique: (1) the evolution is not simply showing the removal of the initial rough surface structure but also reveals subsurface damage and (2) the MRF process itself introduces negligible additional damage and/or surface structure when compared to grinding. As will be seen later, the validity of assumption (2) is dependent on the grade of SiC being studied. This thesis thus provides a critical look at the technique and its validity and limitations.

2.6.5 Machine Setup

D10 fluid from QED consisted of two parts, solvent and powder. The contents were mixed as per QED's instructions and tumbled for 30 minutes. There were two circuits for fluid flow. In the first circuit, the fluid chamber, delivery pump and damper

were connected through tubes to the fluid outlet nozzle which delivered fluid to the wheel. The fluid then returned through the return inlet and suction pump to the fluid conditioning chamber. In the second circuit, the fluid from the conditioning chamber was recirculated back into the chamber by a nozzle using a viscosity pump where a pressure sensor was used to monitor the viscosity of the fluid. If the fluid viscosity was above a cutoff value, distilled water was added in drops using options available in the software interface to maintain the desired viscosity. Peristaltic pumps were used in both circuits. The tubes were lubricated periodically during operation using silicone lubricants to avoid tube rupture. In summary, the fluid from the first circuit polished the workpiece and the second circuit monitored the viscosity of the fluid.

Prior to operation, the fluid conditioning chamber was filled, and the machine was turned on in Standard Operation Mode. The machine was left running for 30-40 minutes to stabilize the viscosity before polishing. Once prepared, the MRF fluid was usable for a period of three weeks [46]. When the machine was not in operation for polishing, the machine was set to operate in bypass mode which kept the fluid circulating without contamination or oxidation.

2.6.5 Experimental Procedure

Once the machine was operational with the fluid, the ribbon height flowing over the wheel was measured using a capacitance probe. The height of the ribbon was adjusted using the knob under the delivery pump to 1.6 mm to maintain consistency throughout the experiments. The MRF machine also has a built-in camera to observe and adjust the ribbon height. Parameters such as wheel speed (600 RPM), wheel radius (25 mm), delivery and return pump speed (85 RPM), viscosity pump speed (60 RPM), ribbon

height (1.6 mm) and depth of part penetration into ribbon (0.7 mm) were maintained constant for all experiments.

Based on the works presented by Shafrir et. al. [32] in silicon carbide, a maximum spotting time of 16 minutes was used for the initial tests on samples ground on the Makino A55. The spotting times used for CVC and the two CVD samples were varied as follows: 1, 2, 3, 4, 6, 8, 10, 12, 14 and 16 minutes. Due to limited space for spotting on the direct sintered sample, the spotting times used in this sample were 1, 2, 3, 6, 9, 12 and 16 minutes. The part was rotated after the generation of each spot producing the patterns shown in Figure 8. Angular orientation was tracked by a fiducial point on each sample referenced to 0°. For each experiment, the samples were mounted on the vacuum chuck and the spots were polished on the samples for the above-mentioned spotting times by entering the corresponding angles in the software after each spot. Figure 10 shows a CVC grade sample after the MRF spots were made on the rough, medium and finish ground regions.

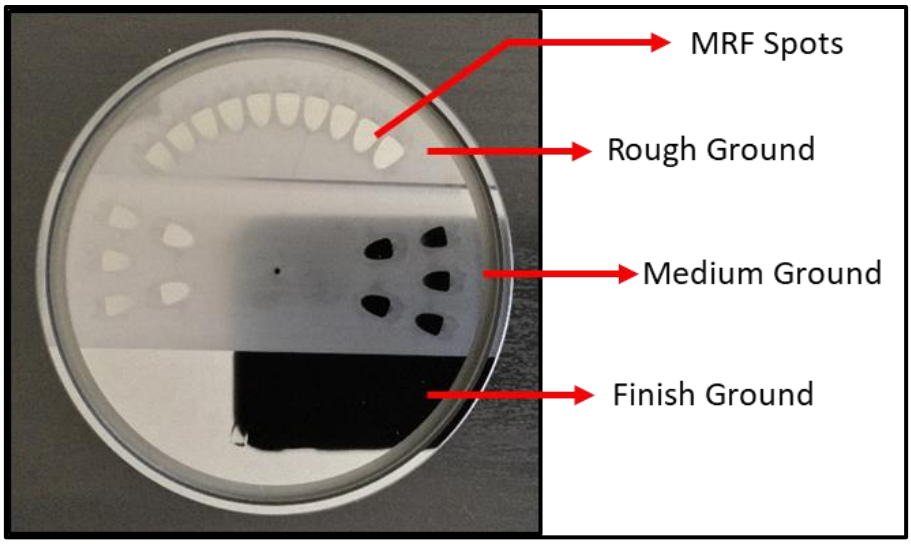

FIGURE 10: CVC grade silicon carbide sample with MRF spots with different spotting times

The fluid viscosity of the MRF fluid was maintained between 63 cP and 69 cP during the spotting experiments in all samples. After polishing all the spots on a sample, the sample was rinsed in ethyl alcohol. The surface roughness values were measured at the deepest region of the spots and the roughness parameters were plotted as a function of spotting time. The presence of subsurface damage was characterized by studying the change in roughness parameters with spotting time as previously described. Spotting time was correlated to spot depth by making quantitative depth measurements using CSI 2.75x objective (Field of View: 3 mm x 3 mm).

Chapter 3 discusses in detail the procedures used for assessing the surface and characterizing the subsurface damage present in the ground samples.

CHAPTER 3: SURFACE ASSESSMENT SETUP AND PROCEDURE

3.1 Introduction

This chapter discusses the acquisition of images using scanning electron microscopy (SEM) and the generation of surface height maps using coherence scanning interferometry (CSI). These instruments allowed for both qualitative and quantitative assessment of the ground sample surfaces and the spot surfaces. Data from these instruments were used to characterize the effect of grinding parameters and grinding configurations on surface texture and compare the surface appearance between the different grades. In some cases, observation of the surface character could be used to make hypotheses about the material removal mechanisms active in the grinding process.

3.2 Scanning Electron Microscopy

The SEM used for this study is a JEOL JSM 6480. The microscope enabled qualitative study of surface texture as a function of the grinding parameters (Chapter 4) and also validation of MRF technique by studying the surface texture at different spotting times (Chapter 2). This section describes the procedure for loading samples, acquiring images and then removing samples from the SEM. SEM settings are given in detail to allow others to repeat the measurements.

3.2.1 Sample preparation, setup and procedure

The sample surface to be imaged was rinsed with ethyl alcohol to prevent any dirt or impurities from contaminating the system. The sample was fixed to the specimen holder using double sided copper tapes. Since silicon carbide is partially conductive, it was not necessary to coat them before imaging in the SEM. Using the software interface and video feed from an IR camera (IR Chamber Scope) located inside the SEM chamber,

sufficient space was made in the specimen chamber by altering the Z position of the specimen stage. As a safety precaution, fundamental setup height was set as a safety stop along the Z direction based on sample height. The stage must be in ‘Exchange’ position (X = 0 mm, Y = -25 mm) before loading the sample. The specimen chamber was vented, and the specimen holder with the sample was placed inside. The specimen chamber was then locked and evacuated. Figure 11 shows a sample placed on a specimen holder and Figure 12 shows the setup inside the SEM chamber.

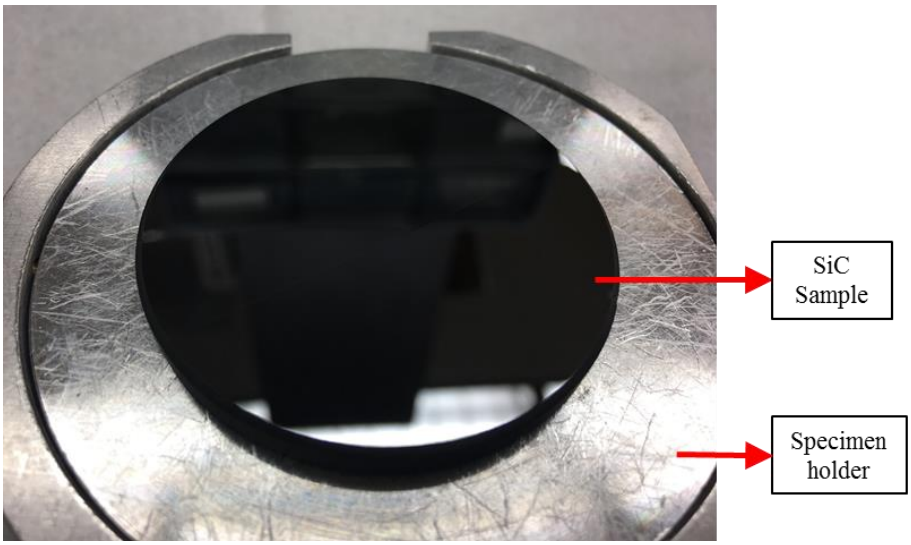

FIGURE 11: Specimen holder with SiC sample

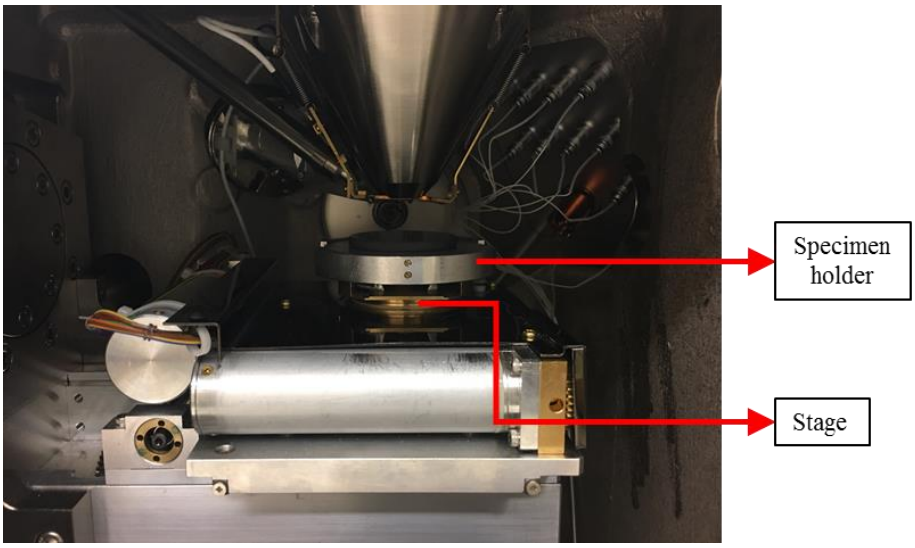

FIGURE 12: SEM specimen chamber

The stage was moved to center position (X = 0 mm, Y = 0 mm). A working distance of 10 mm was selected. The Z height was moved to a distance which is the sum of the working distance and sample height. The SEM has 3 objective aperture sizes. The second aperture size was selected since it is the default for routine imaging. An accelerating voltage of 10 kV and a spot size of 30 (no units) was selected. The electron beam was turned on. Using the features present on the surface, the magnification, focus, contrast and brightness were adjusted to get the best possible image of the surface features. At a magnification above 10000x, aperture alignment was performed using the wobbler option and astigmatism correction was performed using the controller. Images of the surfaces were recorded at different magnifications and at different locations on the rough, medium and finish ground samples using the secondary electron imaging (SEI) mode.

The sample was further analyzed using the backscattered electron modes. The backscattered electron imaging consists of three modes: composition (BEC) mode,

topographical (BET) mode and shadow (BES) mode. Composition mode produces images that differentiates the densities of the material on the surface. This reveals the presence of different materials on the surface, particularly useful studying two-phase grades of SiC. Topographical mode reveals different features on the surface. Shadow mode combines the results of composition mode and topographical mode to produce images for better characterization of the surface. After adjusting spot size, contrast and brightness for clear images, backscatter electron images were acquired at same locations as SEI. Once imaging was complete for a sample, the electron beam was turned off and the specimen chamber was vented. The stage was moved to the exchange position (X = 0, Y = -25 mm) and the specimen holder was then removed from the specimen chamber. The same steps were repeated for imaging all the samples.

3.3 Coherence Scanning Interferometry (CSI)

The CSI used for this study was a Zygo Nexview. The software interface used for data acquisition was Zygo Mx. CSI measurements enabled quantification of surface texture in terms of roughness parameters as well as allowing for further characterization of spatial wavelengths through the calculation of the power spectral density (PSD).

3.3.1 Measurement setup

The sample was cleaned using ethyl alcohol to remove any dirt from the surface being measured. The sample was placed on a motorized stage. Using the controller, the stage was moved to the measurement location. As a safety precaution, a Z stop limit was set and the objective was moved along Z direction to bring the sample surface into focus. Alternate light and dark fringes appear on the screen due to interference between light reflected from sample surface and the reference plane in the objective. The stage was

tilted about X and Y directions to spread the fringes, forming a null fringe as the surface becomes parallel to the reference plane in the objective. The scan length was set according to surface features with scan origin at the center of scan length. The measurement mode was set to 'CSI' and Z resolution was set to 'high'. The number of averages was set to 5 to reduce errors due to noise. Once the setup was ready for measurement, the measure option was selected to start the measurement process. The procedure was repeated at 30 different locations for each ground sample. The height maps were acquired using 20x Mirau objective for roughness analysis and 2.75x Michelson objective for PSD analysis, both using 1x zoom. Figure 13 shows the measurement setup in Zygo Nexview CSI instrument. The data collected from the instrument were exported as .dat files and processed in MATLAB. The MATLAB code for processing the data are in Appendix A.

FIGURE 13: Measurement setup in Zygo Nexview

3.4 Data Processing

The raw data (.dat files) were imported into MATLAB using the function 'readmetropro' which converted the .dat files to height matrices [47] (See Appendix B).

For imported height matrices with NaN (Not a Number) values caused by data loss during measurement, the data were processed with an additional function [48] from MATLAB Central File Exchange. The function filled the NaN values by interpolating values from the surrounding cells of the raw height matrix data. This function has options to use multiple approaches to perform the interpolation. The method used for processing these raw height data was the default method of the function which used interpolation by least squares approximation.

The surface data was then fit with a first order polynomial in both the x and y directions to remove piston and tilt from the height data. The data thus processed were then further analyzed.

The CVD samples showed significant waviness at surface wavelengths between 200 µm and 250 µm while the CVC showed significant waviness at wavelengths approximately 200 µm in the medium and finish ground regions. The CVC rough ground region had spatial wavelengths dominated by the step over and the feed per revolution of the tool. The direct sintered sample showed similar variability in the same spatial wavelengths. Based on these observations, a Gaussian filter with a wavelength cutoff of 80 µm was chosen for all surfaces to filter the waviness and study the surface roughness data. The Gaussian filter was defined as per ISO 16610-21-2012 [49] with a wavelength cutoff of 80 µm based on the standard wavelength cutoffs predefined in ISO 25178-3-2012 [50].

The weighting function used for the Gaussian filter is a product of two Gaussian filters, one in the *x* direction and one in *y* direction as per Equation (1) [51],

$$S(x,y) = \frac{1}{\alpha^2.\lambda_{xc}.\lambda_{yc}} \exp\left[-\left[\pi\left(\frac{x}{\alpha.\lambda_{xc}}\right)^2 + \pi\left(\frac{y}{\alpha.\lambda_{yc}}\right)^2\right]\right] \quad (1)$$

where λ_{xc} and λ_{yc} are the wavelength cutoffs in *x* and *y* direction.

$$\alpha = \sqrt{\ln 2/\pi} = 0.4697$$

The waviness data thus obtained by convolution was subtracted from the form-removed height data to obtain the roughness data. The final plot generated by the MATLAB code creates pdf files with 3d waviness, 3d roughness, *x*-direction 2d roughness and *y*-direction 2d roughness data and the corresponding roughness parameters. The code used to process and generate the surface roughness parameters is given in the Appendix A. The waviness data and roughness data were studied for all grades of silicon carbide ground using different parameters.

The MRF spot surfaces were also processed with the same set of MATLAB codes, but a fourth order polynomial surface was used (instead of first order) to remove the form of the spot surface. The same procedures were then followed to obtain the roughness parameters. The same 80 µm cutoff wavelength was chosen to have comparable data between the spot surfaces and the ground surfaces. The roughness data obtained after processing in MATLAB were analyzed further.

3.5 Data Uncertainty

Two sources of uncertainty are taken into consideration to present the roughness parameters from CSI measurements; uncertainty based on surface topography repeatability as per ISO 25178-604-2013 [52] and uncertainty from 30 measurements of a ground surface for each parameter set.

Surface topography repeatability tests were performed based on an example procedure given in annex-D of ISO 25178-604-2013 [52]. The surface topography repeatability was estimated for each ground sample to account for the uncertainty of the instrument for each surface topography. In each ground surface, a specific location was selected at random under the 20x objective in CSI to study the surface topography repeatability. 10 measurements were taken at each site with no averaging and no lateral smoothing. To perform this, the average was set to 1 and denoise was turned off in the Nexview during these measurements. Denoise is a 3x3 gaussian filter applied to the raw height data to reduce camera noise. The height data were exported to MATLAB for further processing. For each site, an average height map was calculated and subtracted from the corresponding individual height maps to produce the difference maps. Average roughness (Sa), RMS roughness (Sq) and Peak to Valley roughness (Sz) were calculated for each difference map and averaged. The average estimate of Sa, Sq and Sz thus calculated are the estimates of instrument's uncertainty for the ground surface under observation for the roughness parameters estimated using CSI measurements. The procedure was repeated for each ground surface to estimate the uncertainty corresponding to the respective surface topography. MATLAB code to estimate the uncertainties are available in appendix-C. Due to the unavailability of direct sintered ground surface for surface topography repeatability test, the surface topography repeatability estimated for CVC grade ground surfaces were assumed for direct sintered grade surfaces as well. This assumption was based on the similar levels of homogeneity that these grades exhibit in comparison and that both these grades comprise of single-phase silicon carbide grains in their composition.

To estimate the uncertainty from repeated measurements at different locations, the 30 measurements that were previously taken to estimate the average estimate of roughness parameters for each grinding test were used. Standard deviation was calculated for each ground surface which is a representation of the deviations from the average estimate over the entire ground surface.

The combined standard uncertainty was calculated for each roughness parameter by assuming the above mentioned two major sources of uncertainty were uncorrelated and thus could added in quadrature. Chapter 4 discusses in detail the results of surface measurement data of all ground samples along with their uncertainties and chapter 5 discusses the subsurface damage results using MRF spotting technique.

CHAPTER 4: RESULTS – SURFACE MEASUREMENTS

4.1 Introduction

Surface roughness was characterized on the CSI with a 20x objective. The data was exported to and processed in MATLAB as discussed in Chapter 3, and the roughness parameters Sa, Sq and Sz were calculated as per ISO 25178-2-2012 [53]. The height map from the CSI and surface images from the SEM were used to characterize the surface texture and to assess the material removal mechanics during grinding the different grades of silicon carbide. CSI measurements from 30 different locations were acquired for each ground sample and the roughness parameters were averaged to acquire average estimates of Sa, Sq and Sz as per ISO 4288-1996 [54]. This provided a comparison of the roughness data for the different grinding parameters and across the different grades of SiC. The Mx software was used to generate PSD plots of the surface data. The PSD plots characterized the spatial wavelengths of prominent features on the surfaces. A larger field of view, obtained with the 2.75 x objective, was used for the PSD calculations in order to capture a broader range of spatial frequencies.

4.2 Preliminary Tests on Makino A55

Before proceeding with grinding tests on different grades of SiC, rough, medium and finish raster grinding tests were conducted on the silicon infiltrated grade using the parameters given in chapter 2. First the surface was planarized with a rough grinding pass to remove tilt using rough grinding parameters. This ensured a constant depth of cut in subsequent grinding operations. Next, the entire surface of the sample was rough ground with a depth of 100 µm. Next two-thirds of the surface was ground with medium parameters to a depth of 20 µm twice. Finally, one half of the surface was ground surface

with the finish parameters to a depth of 20 µm twice. The medium and finish operations were performed twice to remove residual surface/subsurface damage from the previous operations.

The surfaces in the test sample were assessed using an SEM and a Zygo Zegage plus CSI. Figure 14 shows the SEM images of the rough ground surface in secondary electron imaging (SEI) and backscattered electron imaging (BEI) modes.

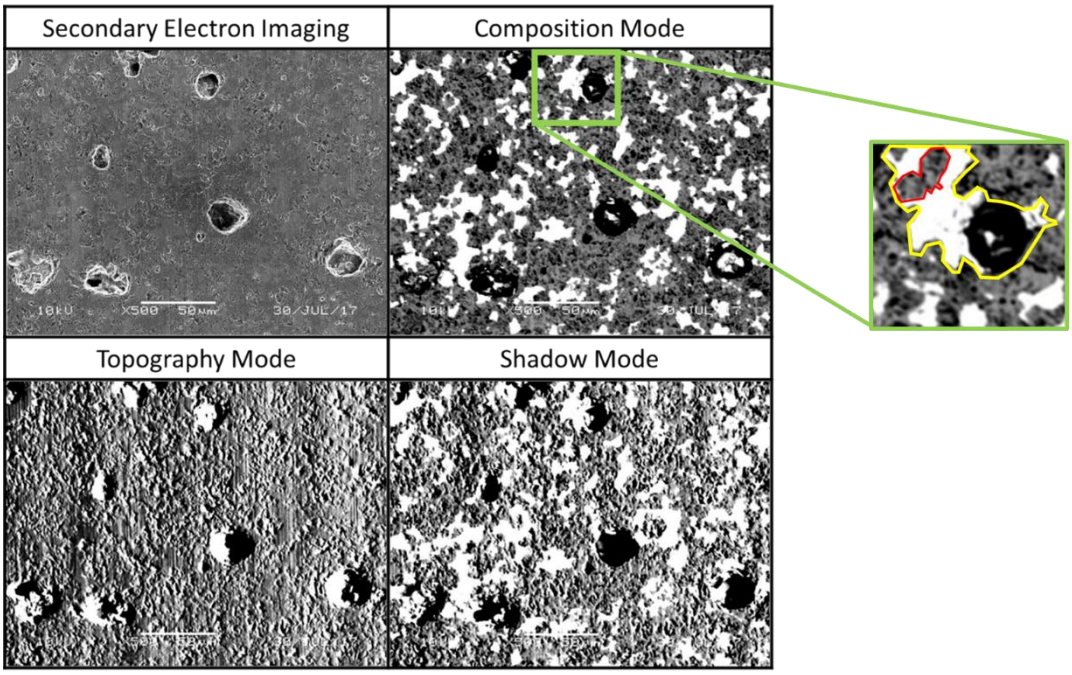

FIGURE 14: SEM images of silicon infiltrated sample (rough ground)

The SEM images from the different modes in Figure 14 allow us to make some hypotheses about the material removal mechanisms occurring in rough grinding of the silicon infiltrated silicon carbide.

First, the composition mode image (top right) indicates the presence of the two phases, SiC appearing as grey and silicon appearing as white. The first hypothesis is illustrated best in the topography mode image (lower left) from the fine rough features

shown. The fine scale roughness indicates a fracture-dominated material removal mechanism. In the composition mode, it appears that the silicon phase is “smooth” whereas the SiC phase is “rough” perhaps further indicating that the silicon is deforming in a ductile mode whereas the SiC is fracturing. While reasonable to assume this could be the case, this supposition needs to be backed up with further evidence.

The second hypothesis is that the large pits evident in the surface are due to grain pull out. As shown in the inset in Figure 14, it is possible that it is the silicon phase being pulled out of the surface. The yellow outline in the inset shows what may have previously been a continuous region of the silicon phase with a section of that region being pulled out and leaving a pit. Alternately though, the pits may be due to pull out of the SiC phase. The red outline surrounds a region of silicon with a grain of SiC in the center. If the SiC grain were pulled out of the region it would have an appearance similar to the yellow outlined region. Thus, it is impossible from appearance to make a conclusion of what is being pulled out. However, because the material is originally continuous but porous silicon carbide that is then infiltrated with molten silicon, it is reasonable to assume that the silicon would more easily be pulled out of the composite. Further, the same phenomenon is not seen in single phase SiC, so the presence of the silicon appears to be the major contributing factor. Further the relative ductility of the silicon versus the SiC might cause it to conform to and adhere to the grinding grits more readily and thus be pulled out the composite material. To more successfully grind two-phase SiC material, the phenomenon would require more study.

The third hypothesis is that some of the fine scale missing material within the SiC phase in the composition mode is due to residual material porosity on a scale that was not

infiltrated by the molten silicon. The density of the base SiC material before infiltration is only approximately 80 percent. This is improved to greater than 95% by silicon infiltration but does not make the material fully dense. Thus, fine scale residual porosity is expected. All of these phenomena are important for determining the surface integrity of the final component.

Interferometric measurements on the CSI provide further insights and begin to quantify the phenomenological observations made from the SEM images. Measurements were made with a 20x objective and processed as discussed in Chapter 3 with an 80 μm cutoff Gaussian filter. Figure 15 shows the waviness and roughness height maps after surface filtering. The average estimates of roughness values for the rough ground region were 0.5550 ± 0.1750 μm Sa, 1.5837 ± 0.4036 μm Sq and 33.2100 ± 8.6464 μm Sz. The surface waviness and the surface roughness are both dominated by the large pits that we hypothesize are due to material pull-out. When the large pits were isolated using region analysis in Zygo Mx, the surface appeared to be dominated by brittle fracture between the pull-outs.

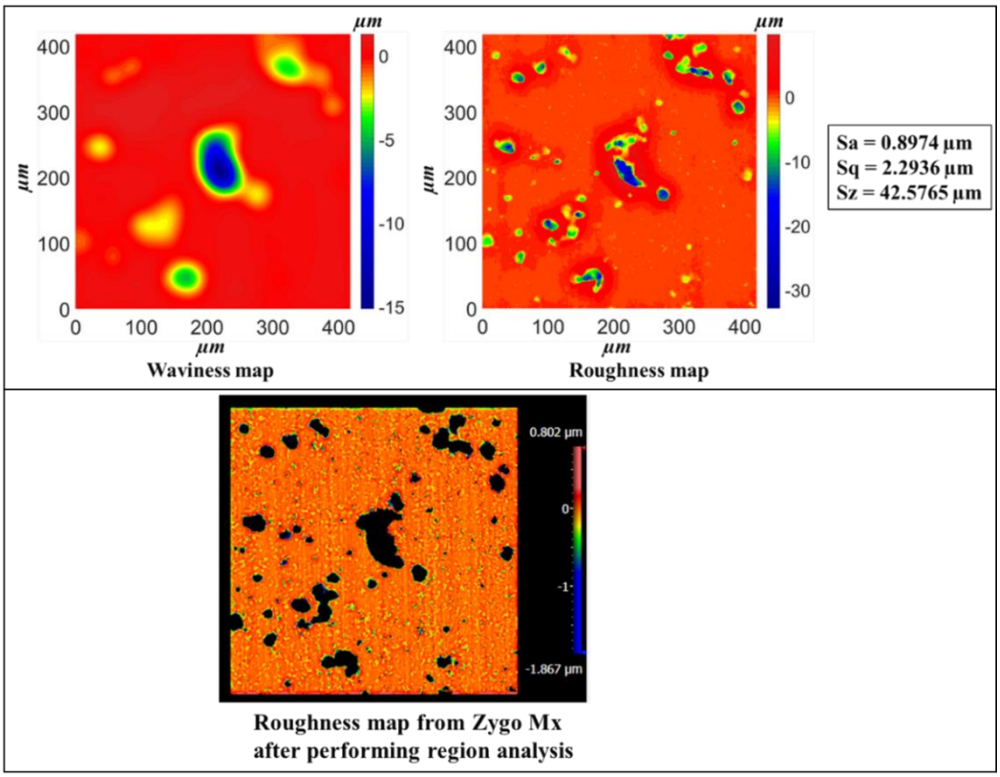

FIGURE 15: CSI height map of silicon infiltrated grade (rough ground)

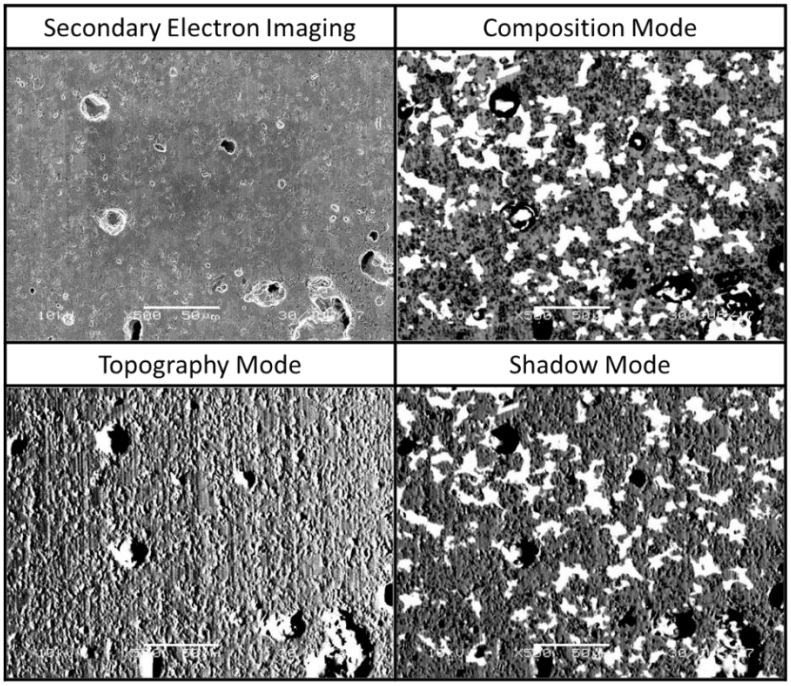

FIGURE 16: SEM images of silicon infiltrated sample (medium ground)

The surface ground with medium parameters that was analyzed using SEM images (Figure 16) also showed the presence of pits due to grain pullouts and surface fractures similar to the images observed from the rough ground region. This suggests that the roughness parameter values will be high for the medium ground region as well. Figure 17 shows 20x objective CSI measurements of the medium ground surface. Compared to rough ground surface, the medium ground surface showed relatively lower roughness values. The average estimates of roughness parameters were 0.3505 ± 0.1361 µm Sa, 1.1951 ± 0.3793 µm Sq and 28.6736 ± 12.4425 µm Sz. It was hypothesized that this was a result of the surface experiencing more ductile deformation in medium ground surface than in rough ground surface thus resulting in less fractured areas and also due to interactions of smaller grit size diamonds with the surface. Since the pits dominate the roughness parameters, an alternative hypothesis could also be made that the reduction in roughness parameters indicates a decrease in the average size and depth of the pits for medium grinding parameters.

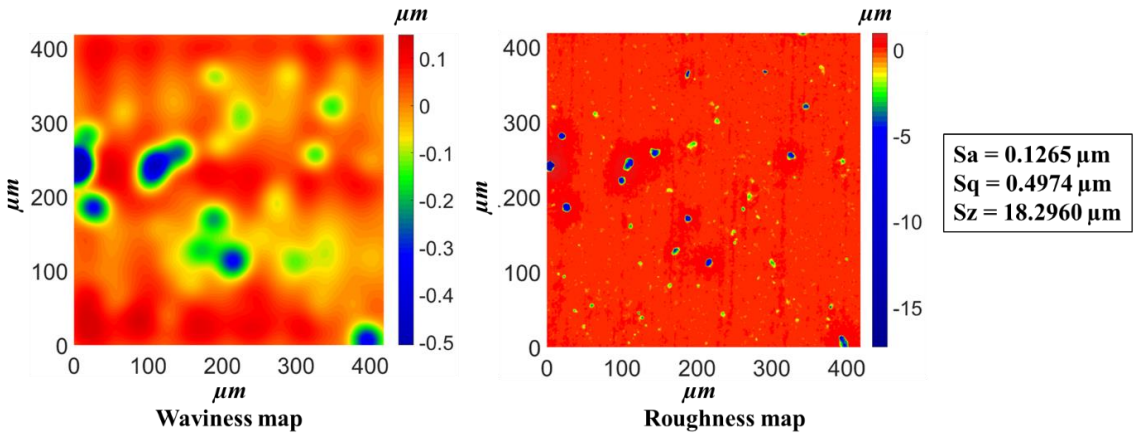

FIGURE 17: CSI height map of silicon infiltrated grade (medium ground)

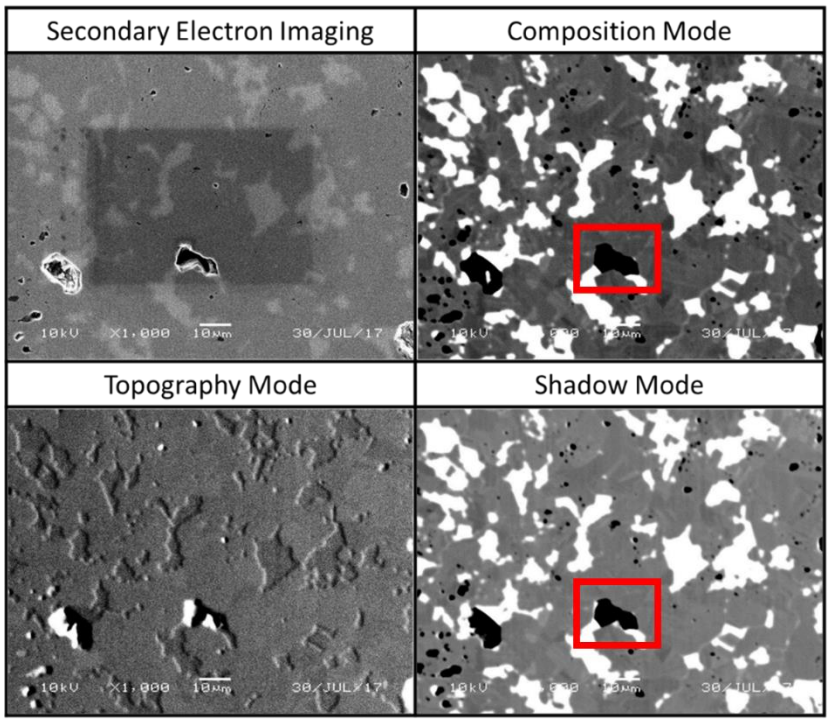

FIGURE 18: SEM images of silicon infiltrated sample (finish ground)

Figure 18 shows SEM images of the finish ground surface under higher magnification than that in Figure 14 and 16. Pits due to grain pull-out are still apparent but the size scale of the pull outs has decreased further from the medium grinding conditions. Also, for the pit in the red box in the composition and shadow mode images, it seems likely that the material that was pulled out of the surface was silicon and not SiC. The silicon carbide material also appears to have less fine structure than in the rough and medium ground surfaces possibly indicating a transition to a more ductile mode of deformation. The topography mode in Figure 17 showed the presence of step-like features across the finish ground region. Comparing the topography mode with composition mode, it could be observed that the boundaries of these step-like features align with the change in phases across the sample. It could be hypothesized that these

step features are due to one of two mechanisms: (1) different material removal rates in SiC versus silicon; or (2) differences in the elastic recovery of the two materials after unloading. Since the hardness and stiffness of silicon carbide are both higher than in silicon, the silicon phase may experience higher material removal rates and higher elastic deformation during grinding.

The grain differentiation is evident only in the finish ground surfaces and not in the rough or medium ground surfaces. There are several potential reasons for this. First, in the rough and medium ground samples, it appears that the material removal in silicon carbide is dominated by brittle fracture whereas in silicon, the material removal is dominated by ductile deformation. Brittle fracture of the SiC will generally produce lower local average forces than ductile deformation of SiC. Further, the material removal rates by brittle fracture will be larger than those when the material deforms in a ductile manner: brittle fracture is more energetically favorable than ductile deformation for more rough grinding conditions. This coupled with the fact that the brittle fracture will dominate the local surface texture would tend to suppress any evidence of grain differentiation. Hence, for the rough and medium grinding, any grain differentiation is lost in the "noise" of the other phenomena. However, for finish grinding where both materials appear to be deforming in a ductile manner due to lower local chip thicknesses and higher hydrostatic pressure, the energy and forces required to remove SiC would be much higher than those for silicon. A different material removal rate in the two materials would thus be expected. The higher forces in the SiC and the lower stiffness of the silicon would also lead to more elastic deformation and subsequent elastic recovery in the

silicon versus the silicon carbide. This is similar to the mechanism that leads to grain relief in precision diamond turning.

Another difference between the rough, medium and finish grinding processes are the properties of the grinding wheels. The rough and medium grinding wheels have a stiffer metal binder with larger grits than the finishing wheel which has a more compliant copper-resin binder and smaller grits. In finish grinding, we would expect higher local stresses that contribute to greater elastic deformation in both the wheel and the surface materials.

Figure 19 shows the 20x CSI measurements of the finish ground surface.

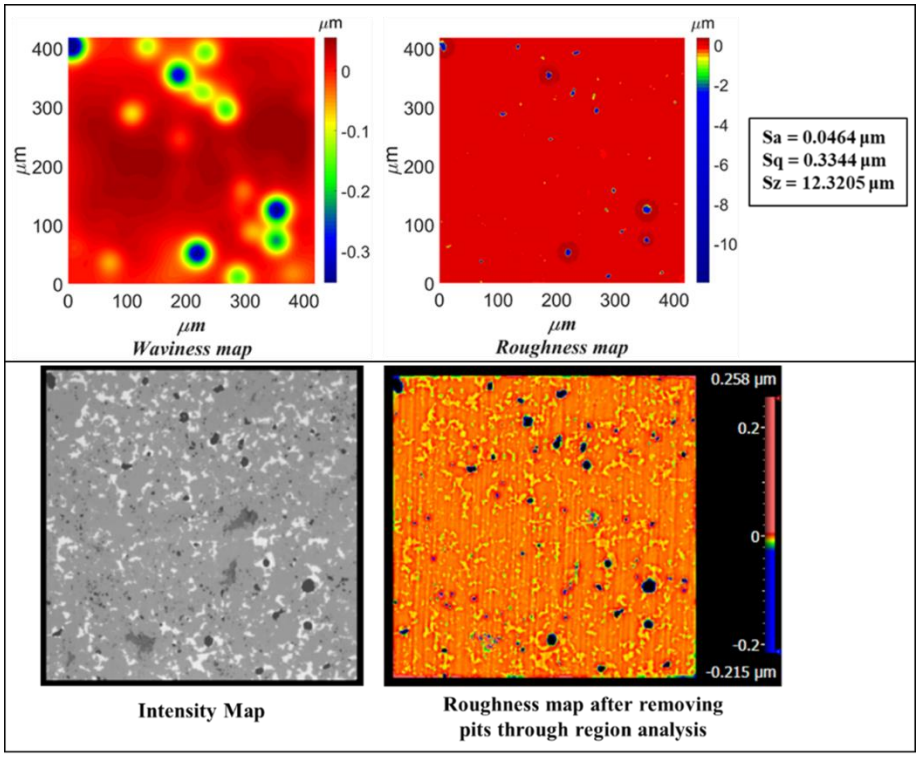

FIGURE 19: CSI height map of silicon infiltrated grade (finish ground)

The average roughness parameters were 0.1579 ± 0.0687 µm Sa, 0.7731 ± 0.2682 µm Sq and 22.5691 ± 7.6363 µm Sz. The high values of roughness parameters were

attributed to the pits from porosity and grain pullouts. Since the pits present on the sample were large (Sz = 22.5691 ± 7.6363 µm), the presence of step like features were not significantly visible on the surface on the CSI images. If the major pits were removed using Zygo Mx region analysis, it can be observed from Figure 19 that the grain relief would be the final factor limiting the attainable surface roughness in silicon infiltrated SiC.

The practical conclusion here is that two-phase SiC, while it has improved density and strength, the nature of the material significantly limits its grinding performance and makes it an unlikely candidate for optical surfaces. Later in the thesis we will see that the two-phase nature of the material also limits the ability of MRF to improve roughness.

4.3 Grinding Tests on the Makino A55

Direct sintered, CVD and CVC were ground on the Makino A55 in a raster configuration using parameters as discussed in Chapter 2.

4.3.1 Direct Sintered grade:

A direct sintered grade of SiC was acquired from Coorstek. The whole surface of the sample was ground using rough parameters, followed by grinding two-thirds of the surface with medium parameters and the final third of the surface was finish ground. The parameter sets are available in Table 1 of chapter 2. Figure 20 shows a photograph of the ground direct sintered silicon carbide sample.

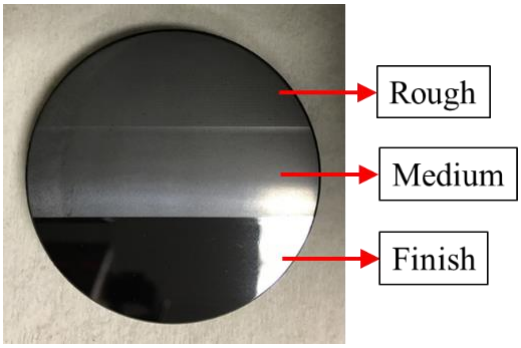

FIGURE 20: Ground direct sintered sample

The finish ground surface is showing a somewhat specular appearance, but further analysis is required to assess surface quality. Figure 21 shows SEM images of the rough ground surface in both, secondary electron imaging and backscattered electron imaging modes.

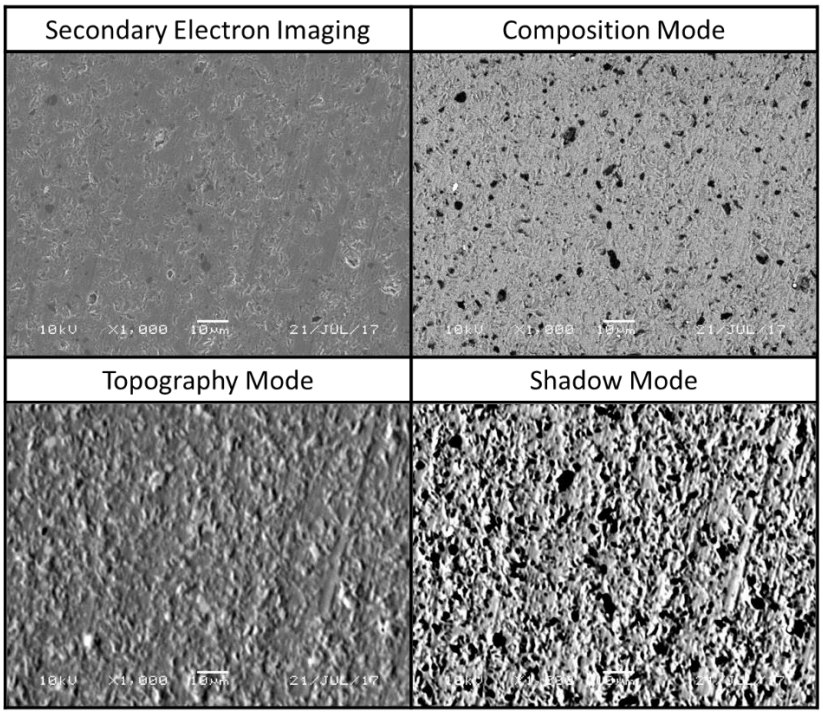

FIGURE 21: SEM images of Direct sintered sample (rough ground)

Both secondary electron imaging as well as different modes in backscattered electron imaging in Figure 21 showed a rough surface at a fine scale. This suggested that the local cutting mechanics was dominated by brittle fracture. Since the direct sintered grade is single phase, the composition mode in Figure 21 did not show significant contrast variations as in the silicon infiltrated grade. Comparing SEI images with backscattered electron images, the dark spots in shadow and composition mode indicated the presence of voids due to either grain pull out or porosity. However, compared to the silicon infiltrated, the surface had smaller pits/voids owing to the grade's method of manufacturing. Thus, the SEM images suggest that we will see lower surface roughness values when compared to silicon infiltrated grade due to smaller pits and less fracture. CSI measurement results confirmed the inferences from SEM images. The presence of surface fractures and pits resulted in higher surface roughness values in CSI measurements. Figure 22 shows waviness and roughness height map from a CSI measurement using 20x objective of a rough ground direct sintered silicon carbide sample.

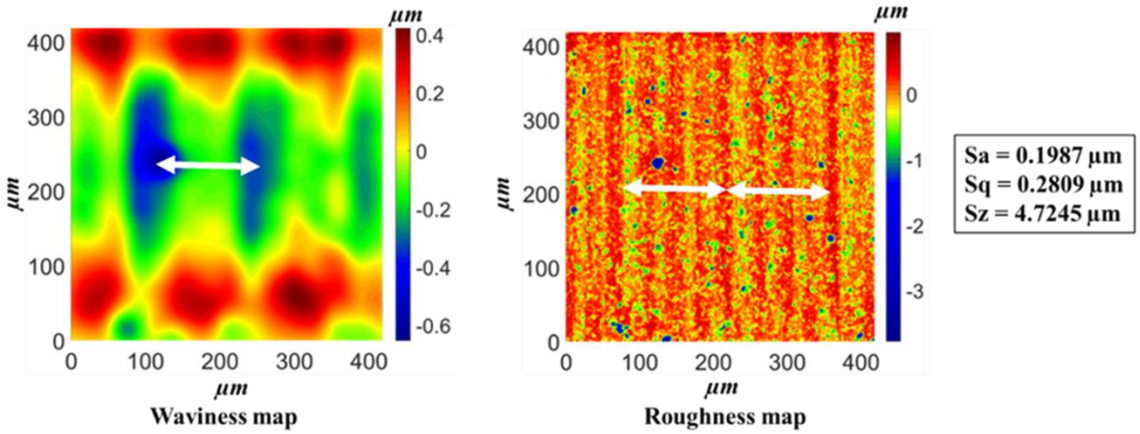

FIGURE 22: CSI height map of direct sintered SiC (rough ground)

The average estimates of roughness parameters for 30 measurements across the rough ground sample were 0.1869 ± 0.0309 µm Sa, 0.2905 ± 0.0630 µm Sq and 8.4348 ± 3.0934 µm Sz. These measurements were made using a 20x objective which has a field of view of 417 µm x 417 µm. Because the surface pits are less dominant in the surface when compared to the silicon infiltrated sample, the features of the geometric cutting conditions have become evident. The wheel feeds across the surface horizontally in Figure 22 and the stepover is vertical. The field of view is too small to adequately resolve the stepover in rough grinding of 500 µm. However, it does resolve the feed per revolution of 150 µm which is visible in the waviness map (white arrowed line). It is evident in the roughness map that the material removal was dominated by brittle fracture but is also more dominated by the fine structure of the wheel which is replicated every 150 µm as indicated by the white arrowed lines. The surface features can be made much more clear using CSI measurements with a larger field of view. A 2.75x objective with a field of view of 3 mm x 3 mm was used. The power spectral density data was analyzed using Zygo Mx software after removing form (plane removed). No filtering was done on this data.

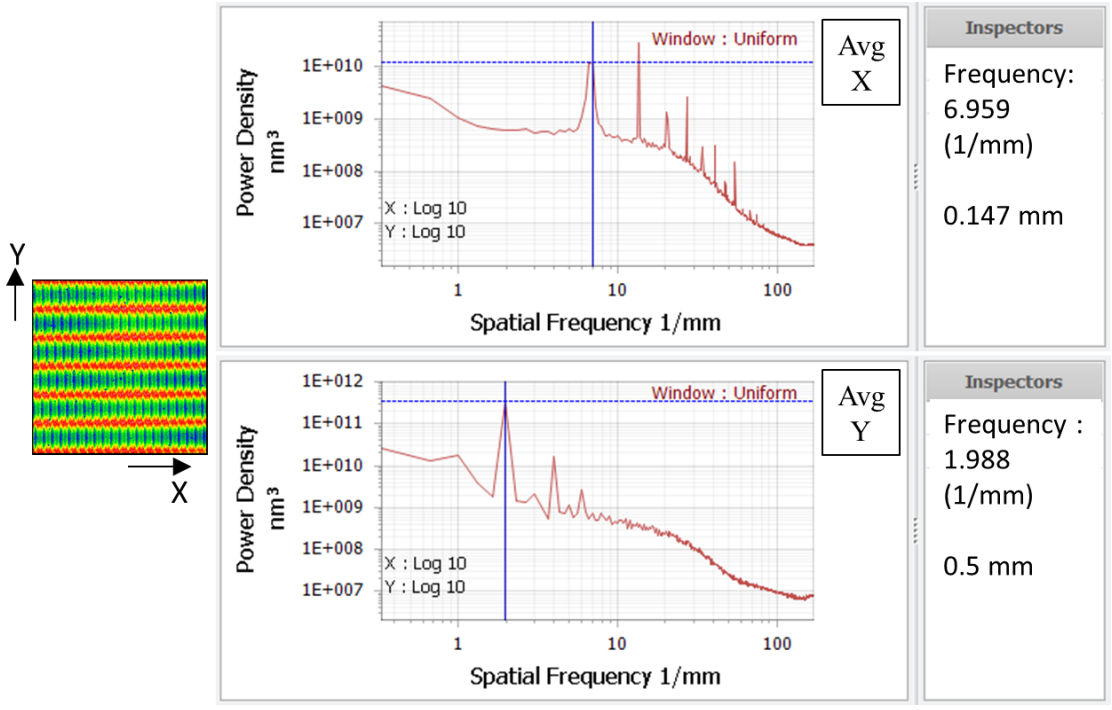

FIGURE 23: 1D – PSD of rough ground direct sintered SiC

Larger field of view measurements clarify these observations and the nature of the surface features. Figure 23 shows one-dimensional – PSD plots acquired using the 2.75x objective in the CSI measurement of the same surface. The grinding feed is along the X direction and the stepover was along the Y direction. The average PSD of X direction traces showed a fundamental peak at a frequency of 6.959 (1/mm) followed by several peaks at its harmonics. The fundamental frequency agrees with the feed per revolution used for the grinding process which was $\frac{1000(^{mm}/_{\min})}{6800(rpm)} \cong 0.147(^{mm}/_{rev})$. The average PSD of Y direction traces showed a fundamental frequency at 1.988 (1/mm) which corresponded with the step over (0.5 mm) used for the grinding process.

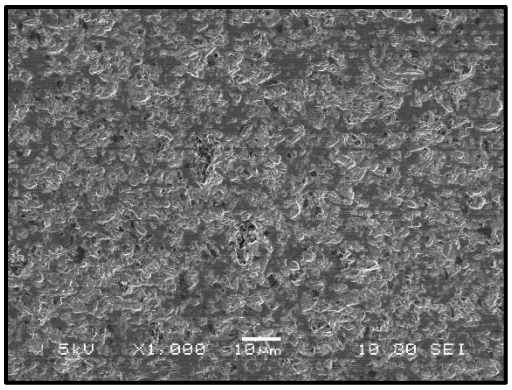

FIGURE 24: SEM image of medium ground sample

SEM images of medium ground surface showed similar features as observed in rough ground area. From Figure 24, it can be observed that the material removal mechanics was dominated by brittle fracture based on its similarity with brittle fractured surfaces shown in [20].

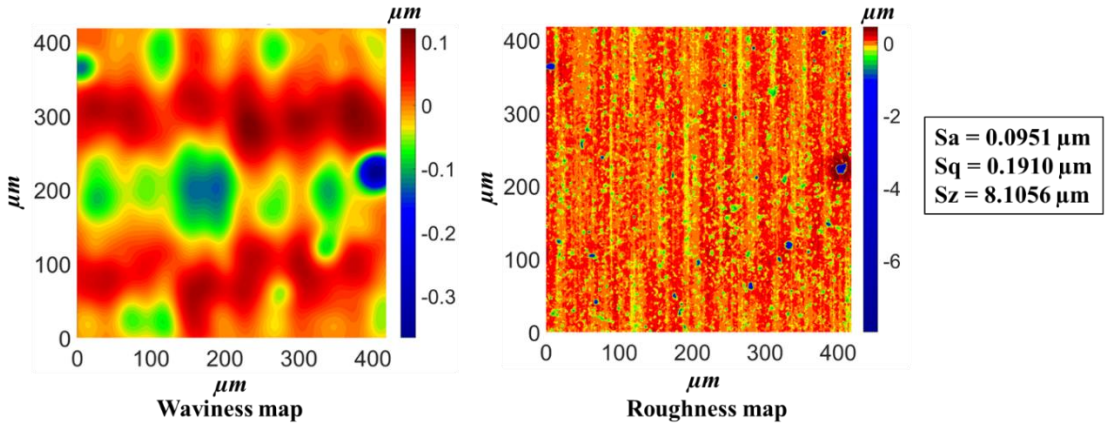

FIGURE 25: CSI height map of direct sintered SiC (Medium ground)

The CSI measurements correlated with the observations from SEM images. Compared to the rough ground surface, the medium ground had improved surface roughness. The average estimate of the roughness parameters for 30 measurements were

0.0904 ± 0.0139 µm Sa, 0.1641 ± 0.0457 µm Sq and 6.3063 ± 1.7437 µm Sz. The Sa roughness is approximately twice as good as the rough grinding conditions while the Sz is only slightly better indicating that large pits are still present on the surface but there are fewer of them (compare Figure 25 with Figure 22). The roughness map in Figure 25 also showed the presence of more prominent scratch marks generated by single grit interactions during grinding. The patterns in the waviness map correlate to the feed per revolution and the stepover in raster grinding. Further study was done using a larger field of view generated with the 2.75x objective. Again, the X-direction in the images corresponded to the feed direction and the Y-direction corresponded to the stepover direction. The average PSD of traces in the X-direction shows a first major peak at 6.959 (1/mm) which correlated with the feed/rev of the grinding wheel (147 µm/rev). A peak is also seen at 10.25 (1/mm) and we are unsure of its origin. It is possible that it relates to some repeating features of the grinding wheel itself. The remaining peaks appear to be harmonics of these peaks.

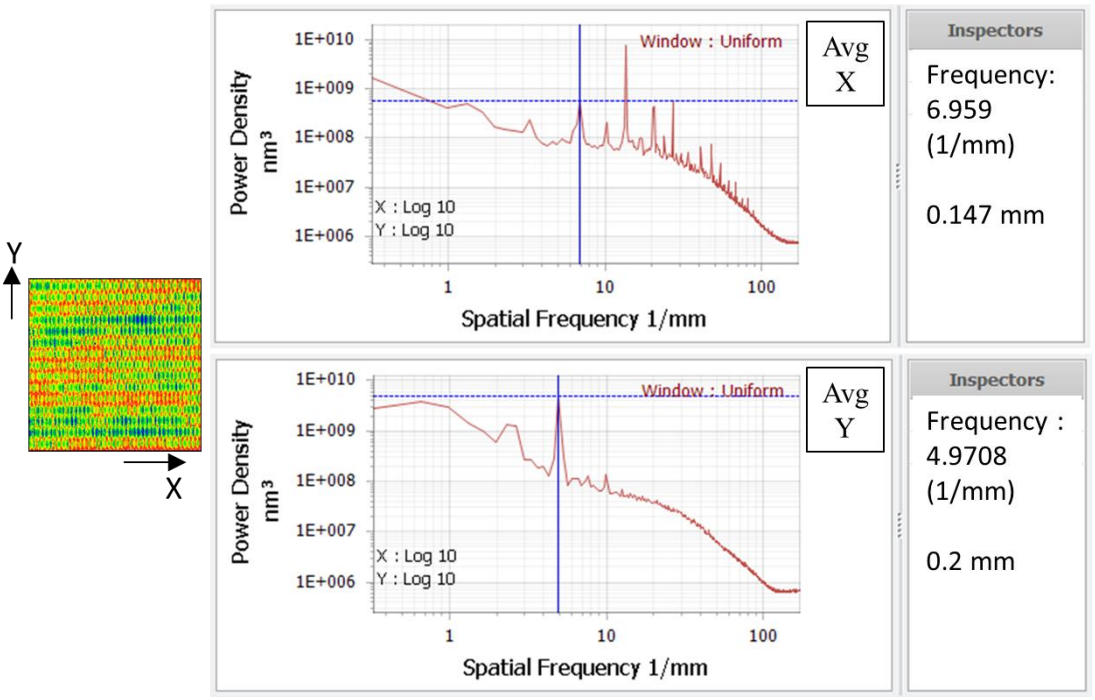

FIGURE 26: 1D – PSD of medium ground direct sintered sample

The average PSD of traces in the Y-direction showed a dominating peak at 4.9708 (1/mm) which correlated with the step over (0.2 mm).

Another broader peak appears at a frequency slightly below 2 (1/mm). This variation can be seen in the image as faint horizontal colored bands. The spatial wavelength is approximately 500 µm which corresponds to the stepover in the roughing operation that occurred before the medium grinding operation. Thus, this peak may be a signature of the rough grinding operation indicating that the medium grinding did not fully remove the surface cusps from the rough grinding. This may be due to elastic deflections of the tool and/or workpiece with variations in depth of cut or possibly a signature of surface damage induced by rough grinding. This suggests that in future work we should use multiple passes of medium grinding after rough grinding to completely remove its signature.

Figure 27 shows SEM images of the finish ground sample. The images of surface texture from the SEM suggested that the material removal mechanics was now dominated by ductile deformation as there were less evidence of fractures on the surface. However, the surface still has significant pits, which we believe is due to sample porosity.

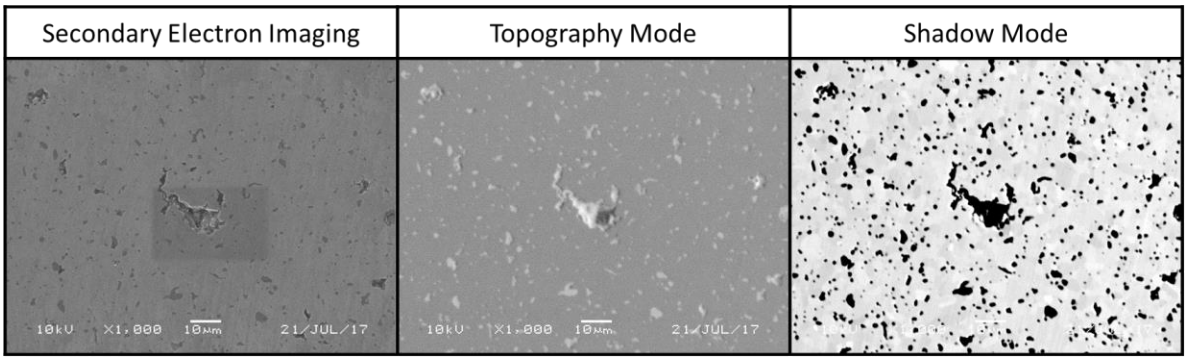

FIGURE 27: SEM images of finish ground direct sintered sample

As expected, the CSI measurements showed lower surface roughness values than those of rough and medium ground surfaces (See Figure 28). The average roughness parameter estimates of 30 measurements were as follows. The Sa was 0.0050 ± 0.0010 µm, nearly twenty times better than the medium ground sample. The Sq was 0.0289 ± 0.0154 µm, nearly six times better than the medium ground samples. The Sz was 2.6741 ± 1.2282 µm approximately two and a half times better than the medium ground sample.

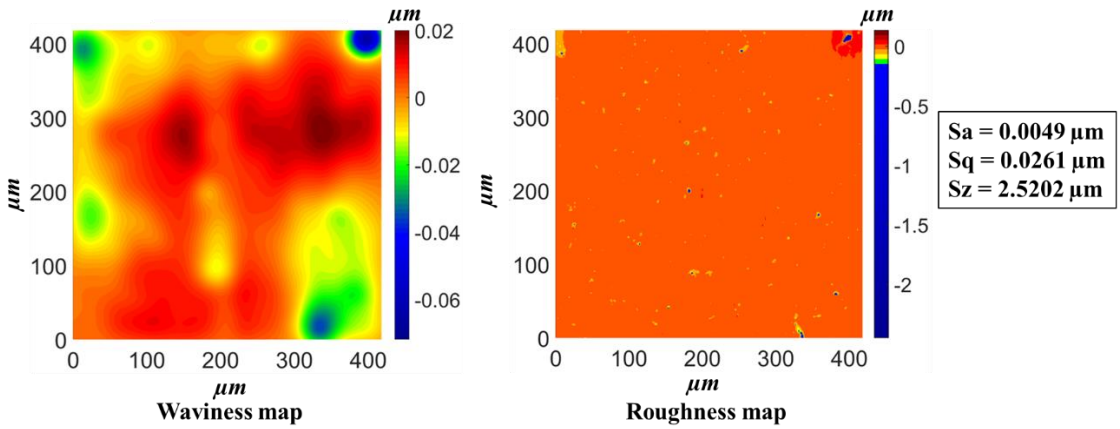

FIGURE 28: CSI height map of direct sintered SiC (Finish ground)

Figure 29 shows PSD graphs of finish ground surface using 2.75x objective. Again, in Figure 29 the feed is in the X direction and the stepover is in the Y direction. Notable, the PSDs for the finish ground surface show fewer dominant peaks than those of the rough and medium ground samples. The one major peak in the X direction was at 68.579 (1/mm) corresponding to a spatial wavelength of 14.6 µm. Recall that for the finishing operations, the feed rate was reduced to 100 mm/min while the wheel speed remained constant at 6800 rpm, so the feed per revolution decreased from 147 µm to 14.7 µm. So, the peak is indeed at the feed/revolution. In the Y direction, the PSD plot showed no significant peak at the stepover of 200 µm although it does appear slightly evident in the waviness plot in Figure 28. Surprisingly in the larger field of view image in Figure 29, there is a dominant longer wavelength pattern seen in the surface with a wavelength of approximately 1.5 mm (frequency peak at approximately 0.6627 (1/mm)). However, this is near the Nyquist limit for this field of view, so the frequency is very coarsely identified. We hypothesize that this peak may be due to machine error motions that were not seen in the rough and finish ground surfaces due to their relatively low magnitude

compared to the cusps produced at the larger stepover values. Such a periodic error motion could originate from the rotation of the ball screw in the axis drive, but more investigation is required to track down the source of this waviness.

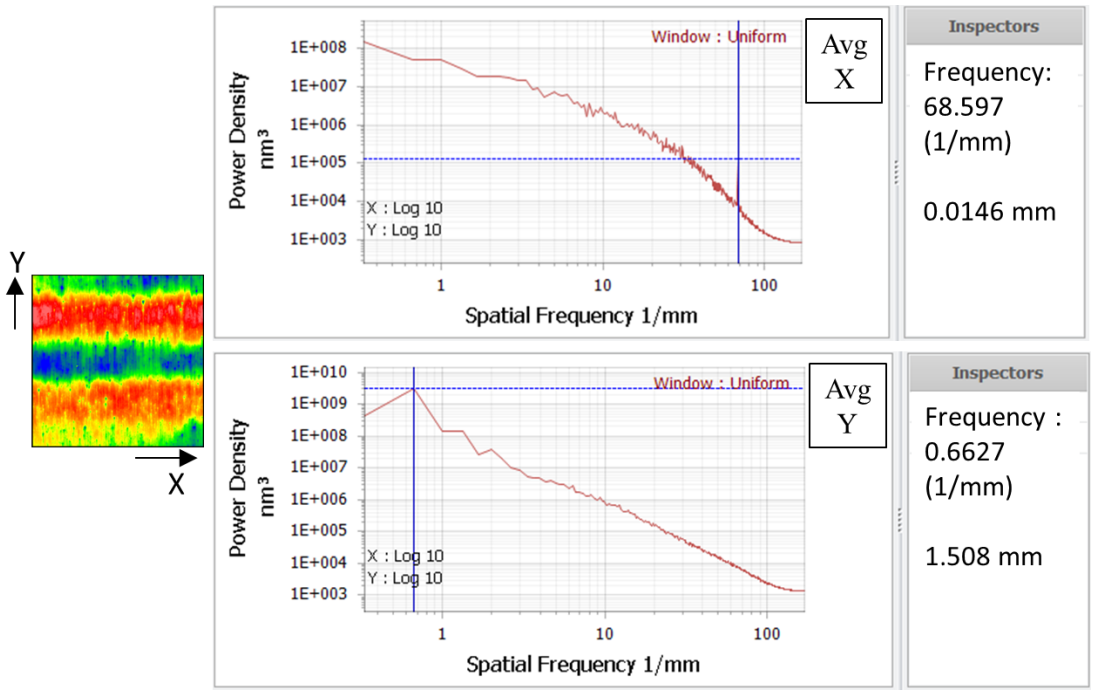

FIGURE 29: 1D – PSD plots of finish ground direct sintered SiC

4.3.2. CVD grade: (Finish only)

CVD grade samples were acquired from Poco Graphite and CoorsTek. Due to the limitations on the CVD coating thicknesses, the surface was only ground using finish parameters. Figure 30 shows SEM images from both CVD samples.

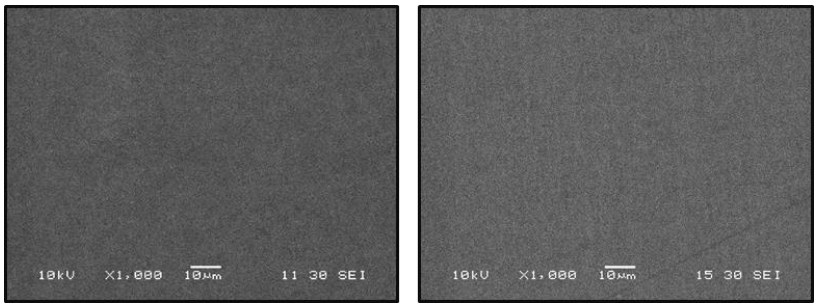

(a) (b)

FIGURE 30: SEM image of CVD samples (a) Sample A (b) Sample B

In both CVD samples A and B, the SEM images revealed that cutting mechanics was dominated by ductile deformation. Also, since CVD is a highly dense pure β-phase SiC grade that is relatively free from voids and microcracks the final surface had no significant pits, voids or surface fracture.

CSI measurements with the 20x objective correlated with the observations from the SEM. Figure 31 shows waviness and roughness height maps from a representative CSI measurement on the CVD sample. The dominating surface features observed were grinding tool marks in roughness map and the stepover of 200 µm in the waviness map. The average estimates of roughness parameters for 30 measurements of CVD B were 0.0023 ± 0.0005 µm Sa, 0.0031 ± 0.0006 µm Sq and 0.0498 ± 0.0199 µm Sz.

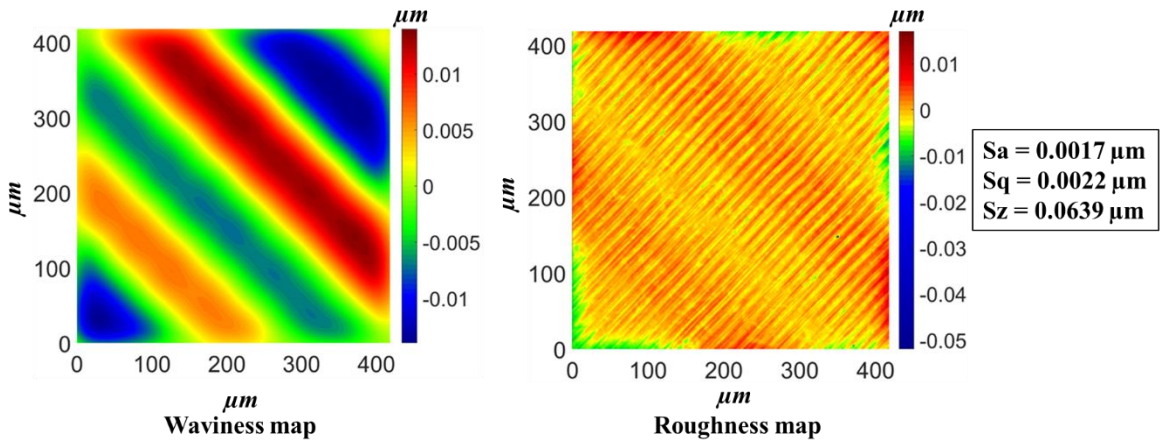

FIGURE 31: CSI height map of CVD sample B (finish ground)

The spatial frequencies were further investigated with larger field of view measurements using the 2.75x objective (Figure 32). Again, the feed is in the X-direction and the stepover is in the Y-direction. The PSD for the X-direction shows a peak at 68.597 (1/mm) that corresponds to the feed per revolution of the grinding wheel, i.e., 14.6 µm. In the Y-direction, the only peak is at a spatial wavelength of 215 µm, which is slightly more than the stepover. This difference is due to the tilt in the sample in the setup during grinding operation.

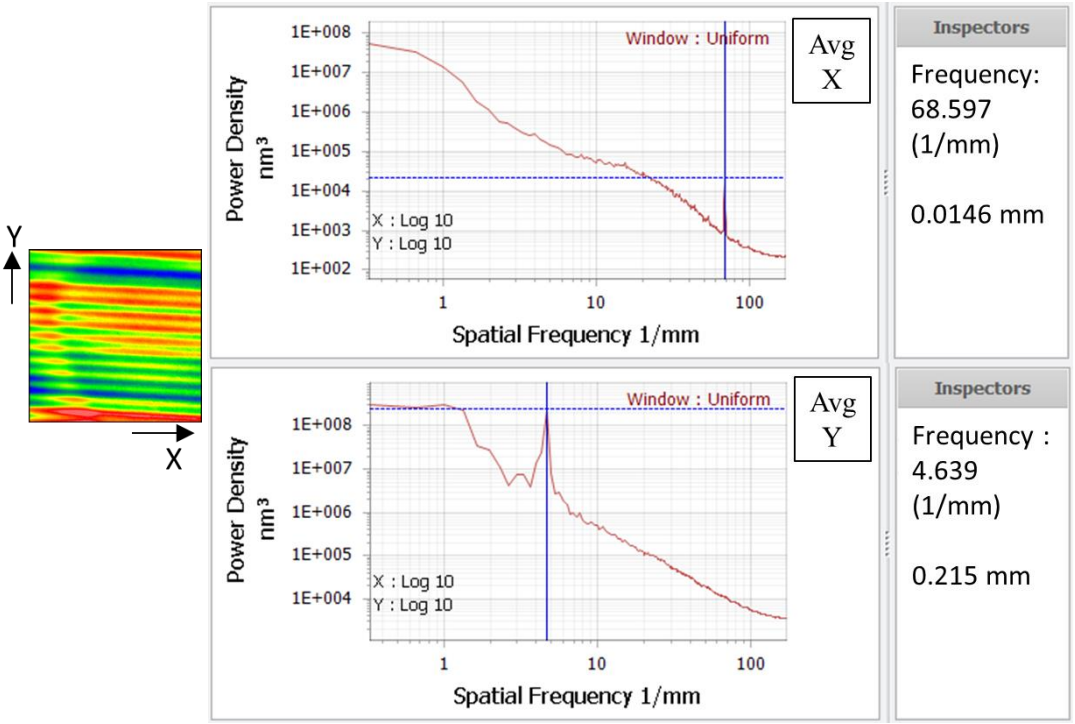

FIGURE 32: 1D – PSD plot of finish ground CVD sample

4.3.3. Chemical Vapor Composite (CVC) grade:

Like direct sintered, the whole surface of CVC grade sample was ground using rough parameters followed by grinding of two-thirds of the sample with medium parameters and then the final third with finish parameters. The SEM images of rough, medium and finish surfaces are as shown in Figure 33.

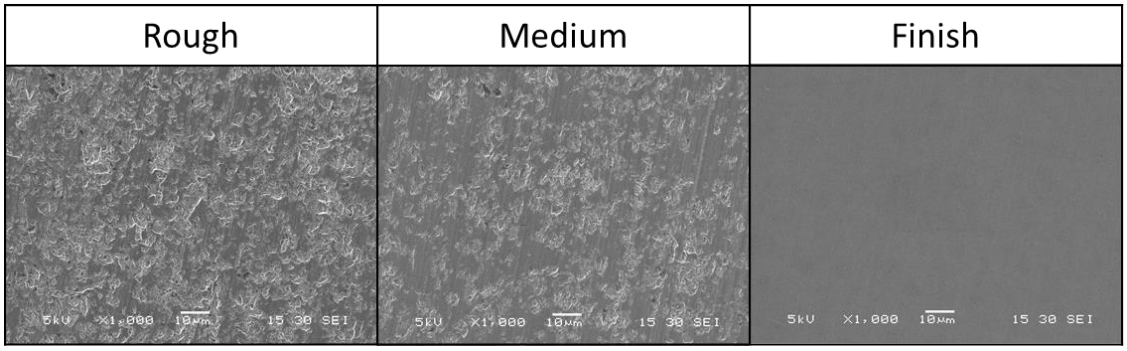

FIGURE 33: SEM images of ground CVC SiC

The SEM image of rough ground surface in Figure 33 showed significant surface fracture. The medium ground surface showed presence of fracture but some sections between the fractures appeared “smooth” indicating some ductile deformation. It is likely that the cutting had more of a ductile component in medium grinding when compared to rough grinding. For the finish ground surface, the SEM image showed that the surface mechanics was dominated by ductile deformation with very little surface fracture.

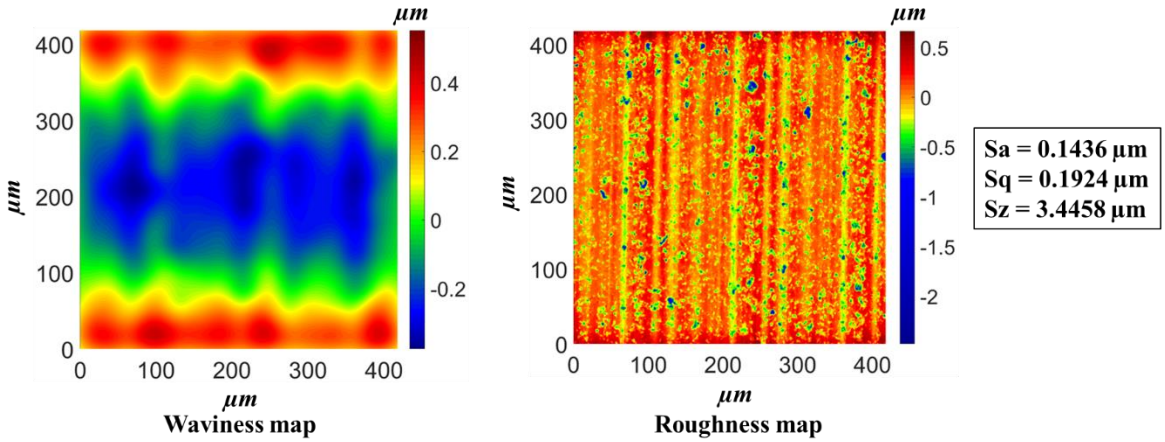

FIGURE 34: CSI height map of CVC grade (rough ground)

Figure 34 shows the waviness and roughness height map of rough ground CVC grade sample. The average estimates of roughness parameters of 30 measurements using the 20x objective were 0.1387 ± 0.0111 µm Sa, 0.1858 ± 0.0349 µm Sq and 2.7184 ± 0.7073 µm Sz. The roughness map shows the scratch marks due to individual grit interactions in grinding. However, in addition, many pits are also seen, likely due to material fracturing from the surface. The waviness map was dominated by the 500 µm step over.

Again, the spatial frequency content in the surface was further studied with the 2.75x objective. Figure 35 shows the surface map and corresponding PSD plots in the X and Y directions. The X direction is the feed direction, and the first peak is at the feed per rev 6.959 (1/mm) with a spatial wavelength of approximately 144 µm. Harmonics corresponding to this frequency are also evident. The Y-direction PSD plot has a first peak at 1.988 (1/mm) which corresponded with the step over used in the grinding process. Harmonics of this frequency are also evident.

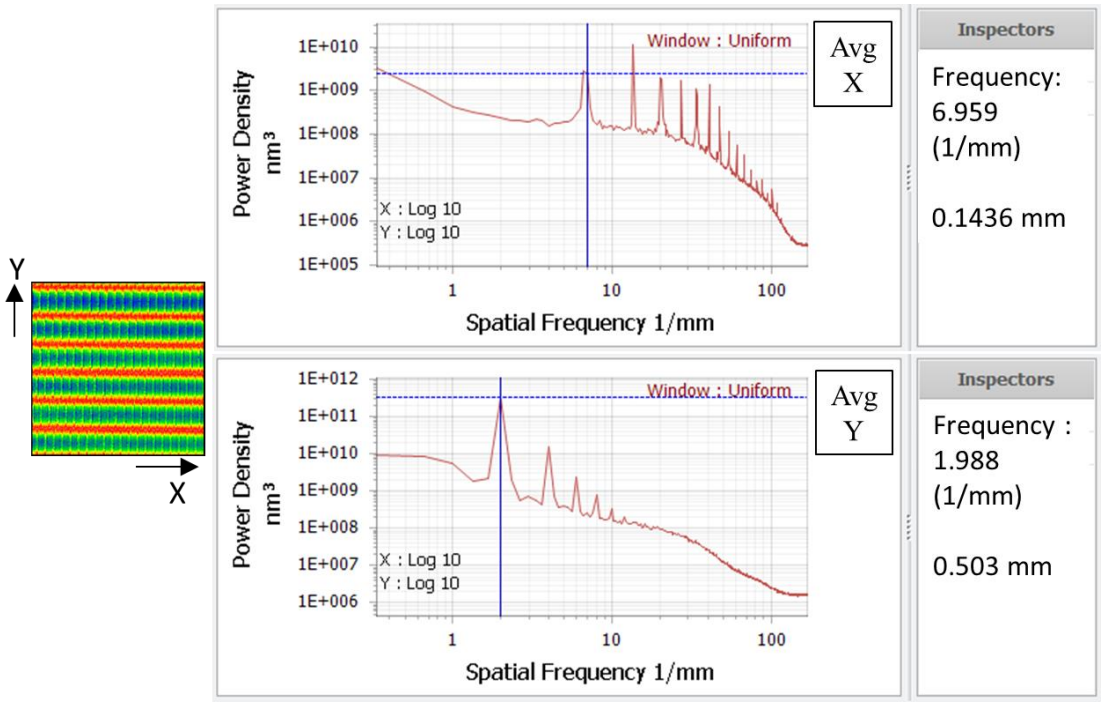

FIGURE 35: 1D – PSD plot of rough ground CVC sample

CSI measurements were also made on the medium ground CVC sample with the 20x objective. The waviness and roughness maps are shown in Figure 36. Since the surface experienced more ductile deformation than on the rough ground region, the surface finish was comparatively better than the rough ground sample. The average parameter estimates of roughness parameters were 0.0841 ± 0.0098 µm Sa, 0.1125 ± 0.0341 µm Sq and 1.7862 ± 0.5888 µm Sz.

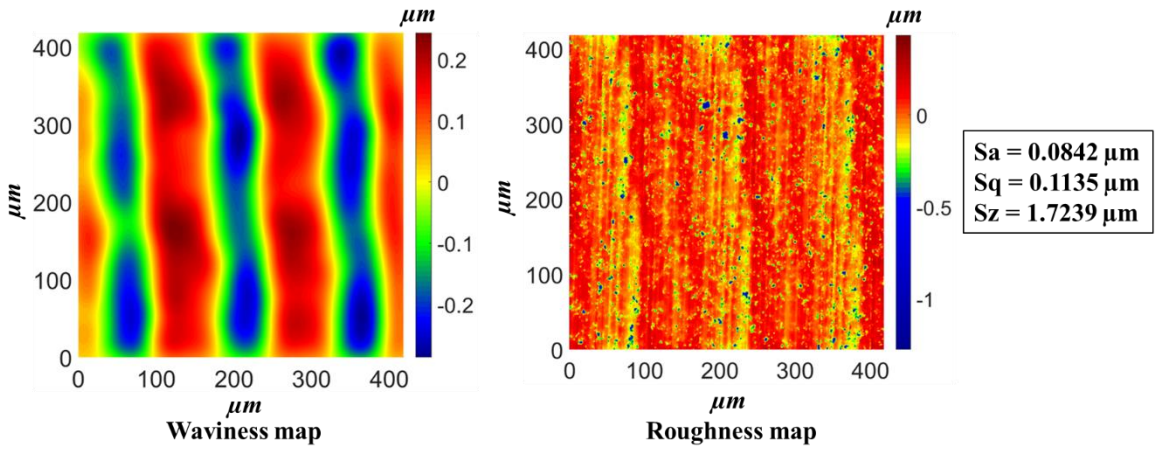

FIGURE 36: CSI height map of CVC grade (medium ground)

Similar to rough ground surface, the roughness map in Figure 36 shows the scratch marks from individual interaction with the grits on the grinding wheel and interspersed pits from brittle fracture. This surface however has some surprising features. The raster feed direction is horizontal and the stepover is vertical as in the previous plots, the waviness plot is dominated by horizontal features with an average frequency of 7.1759 (1/mm) corresponding to a spatial wavelength of approximately 139 µm. This corresponds to the feed/revolution of the wheel. The stepover of 200 µm can also be seen in the waviness and roughness maps but it is less prominent than the feed per revolution.

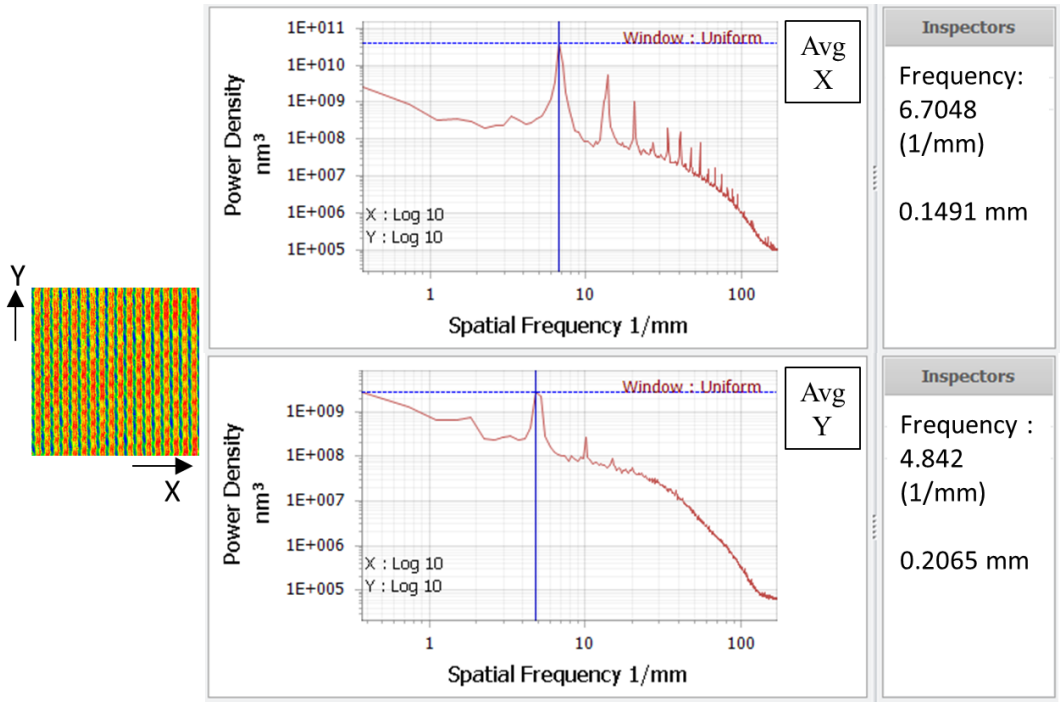

FIGURE 37: 1D – PSD plot of medium ground CVC sample

This is further quantified using larger field of view images taken with the 2.75x objective. Figure 37 shows the PSD plots in X and Y direction where X is the feed direction and Y is the direction of the stepover. The average PSD of traces in the X-direction show a peak at approximately the tool feed rate 149.1 µm per revolution of the tool and its harmonics. The average PSD of traces in the Y direction showed a dominant peak at a frequency of 4.842 (1/mm) corresponding to a wavelength of 207 µm which is approximately the stepover of 200 µm. As in the previous analyses, the deviation of the measured frequencies and the machining parameters is due to slight tilt of the sample. The final sample cut on the Makino A55, finish ground CVC, shows similar features to the rough and medium ground surfaces. Again, height maps were acquired using the 20x objective on the CSI. The waviness and roughness maps are shown in Figure 38. The roughness and waviness maps both show the 200 µm stepover quite clearly. The

roughness height map also shows the presence of scratches from the interaction of single grits with the surface. However, as with the CVC grade, there are very few pits that would indicate surface fracture and the average roughness parameters are similar to those obtained in CVD. Based on 30 measurements on the finish ground surface the roughness parameters were 0.0021 ± 0.0003 µm Sa, 0.0028 ± 0.0005 µm Sq and 0.0327 ± 0.0102 µm Sz.

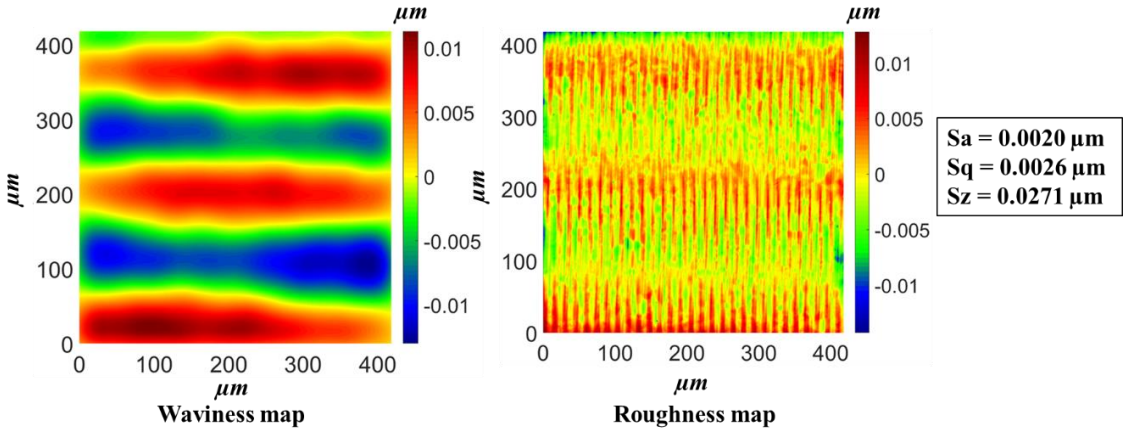

FIGURE 38: CSI height map of CVC grade (finish ground)

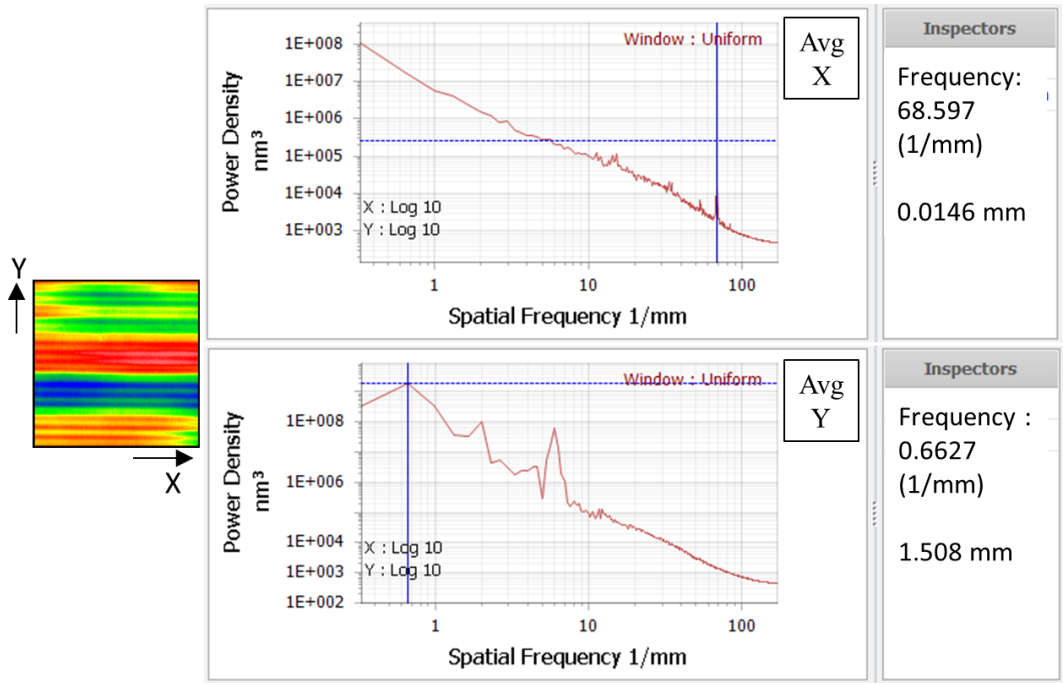

FIGURE 39: 1D – PSD plot of finish ground CVC sample

As in the previous cases, the spatial frequencies are further analyzed with larger field of view height maps obtained with the 2.75x objective on the CSI. The X-direction was aligned with the feed direction and the Y-direction was aligned with the stepover direction. However, as in the previous cases, there is a slight tilt in the sample. As expected, the average PSD plots of X direction traces show a peak approximately at the feed rate of the tool at 14.6 µm. The PSD plot in Y direction shows the stepover at approximately 200 µm. However, they also show the longer wavelength pattern also seen in Figure 29. The frequency is 0.6627 (1/mm) which corresponded to a spatial wavelength of 1.508 mm. This matches what was seen in Figure 29 and as previously stated, we hypothesize that this is related to machine error motions that are perhaps periodic due to the rotation of the driving ball screw on the axis.

4.4. Tests conducted on Optipro 1250X

The different grades of silicon carbide tested in Optisonic 1250X were CVD, reaction-bonded and silicon infiltrated. Grinding wheels used were from two different suppliers. One-inch wheels were acquired from Eminess Technologies. The rough and medium wheels were metal bonded, and the finish wheels were resin bonded. The two-inch wheels were acquired from Scomac. The rough and medium wheels were metals bonded, and the finish wheels were copper-resin bonded. CVD samples were ground using both the raster and spiral configurations. The reaction-bonded samples were ground using the raster configuration only. The parameters used for both configurations are given in chapter 2, Table 2 and Table 3.

4.4.1 CVD grade

Two CVD samples, acquired from POCO graphite, were used for this experiment. The first sample was raster ground using 1-inch wheels. One side was ground using medium parameters and the other side using finish parameters. The second sample was similarly ground with medium and finish parameters in spiral configuration using 2-inch wheels with parameters given in Chapter 2, Table 3. Figure 40 shows the SEM images of both samples at two different locations on the medium ground surfaces.

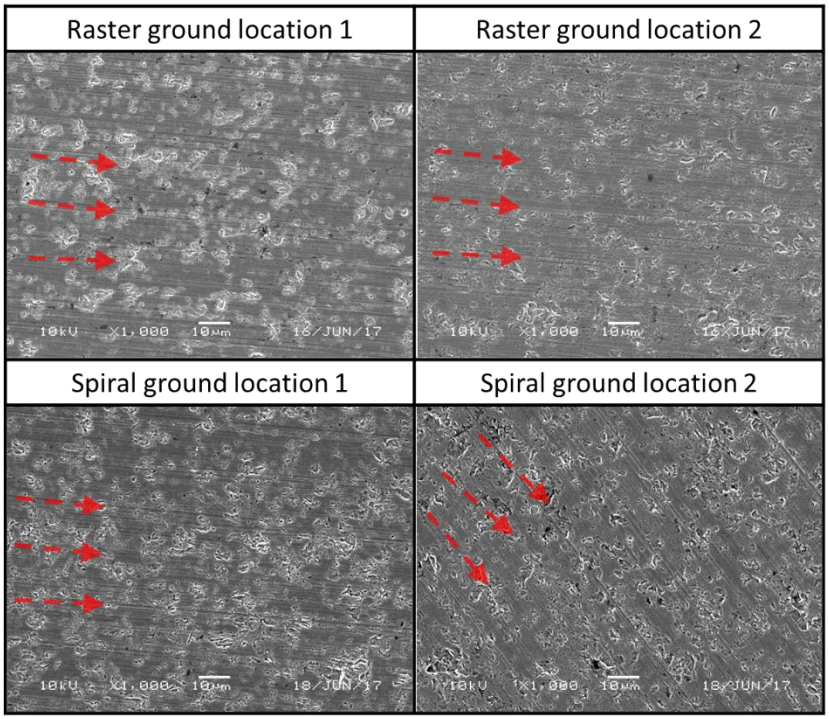

FIGURE 40: SEM images of ground CVD samples in the raster and spiral configurations (medium ground)

SEM images of raster ground surface (Figure 40) showed that the significant surface fracture and pits indicating a more brittle-dominated cutting mechanism. The direction of raster feed is shown by the red arrows on the SEM images. The SEM image of spiral ground surface (Figure 40) also showed that the surface was dominantly generated by brittle fracture. Because both the wheel and the workpiece are rotating in this configuration, the direction of grit motion and hence scratches changes on the sample. This change in direction was observed and indicated by the red arrows in Figure 40.

Height maps of both the raster and spiral ground surfaces in the CVD material were generated with the CSI using the 20x objective. The corresponding roughness maps are shown in Figure 41.

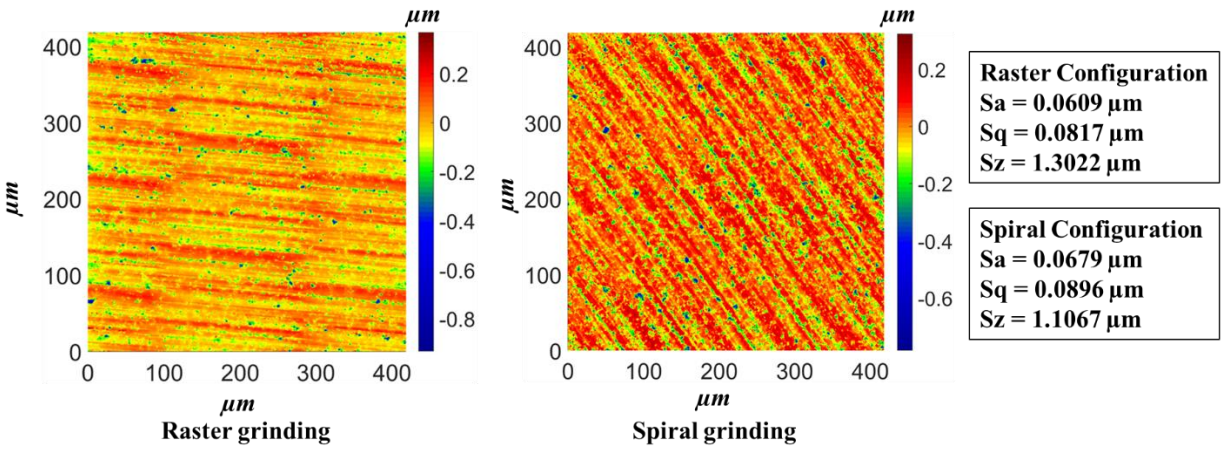

FIGURE 41: CSI roughness height map of CVD grade (medium ground)

Figure 41 showed the presence of grinding marks and the direction of material removal mechanics at the point of measurement. For the raster ground sample, the average roughness parameters were 0.0643 ± 0.0131 µm Sa, 0.0864 ± 0.0299 µm Sq and 1.4624 ± 0.7173 µm Sz. For the spiral ground sample, the average roughness parameters were similar, 0.0585 ± 0.0128 µm Sa, 0.0792 ± 0.0300 µm Sq and 1.1889 ± 0.5802 µm Sz.

The waviness map for both the raster and spiral ground CVD samples are shown in Figure 42.

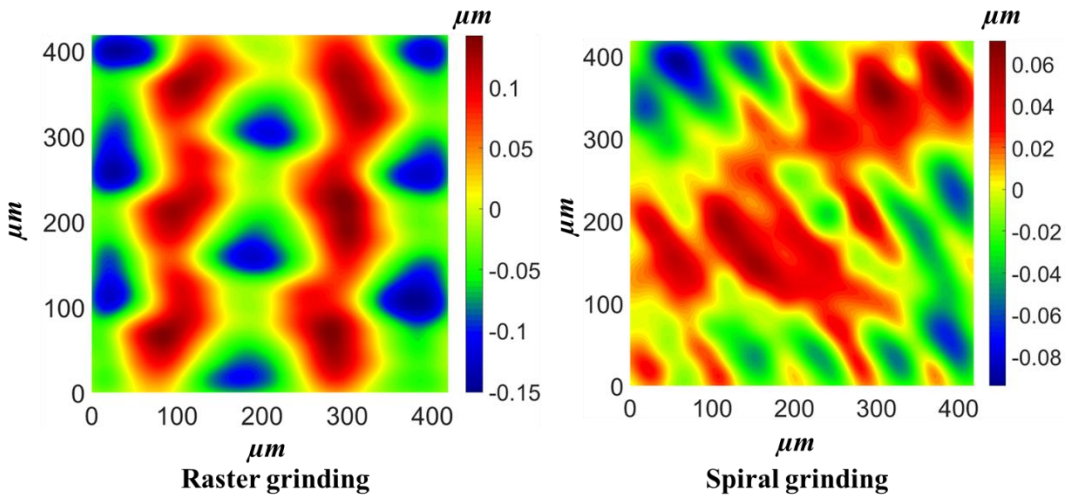

FIGURE 42: CSI waviness height map of CVD grade (Medium ground)

The waviness map of raster ground sample showed the presence of waviness due to stepover in the horizontal direction while there is another periodic waviness pattern due to feed per rev in the vertical direction. The waviness map of spiral grinding showed the presence of a complex surface interaction as a result of the combined workpiece and grinding wheel rotation.

Further analysis to understand the frequency content of the surfaces was done on larger field of view height maps using the 2.75x objective on the CSI. The PSD plots for the raster ground surface using medium parameters are shown in Figure 43 where, as before, the X direction is the feed direction and the Y-direction is the stepover direction.

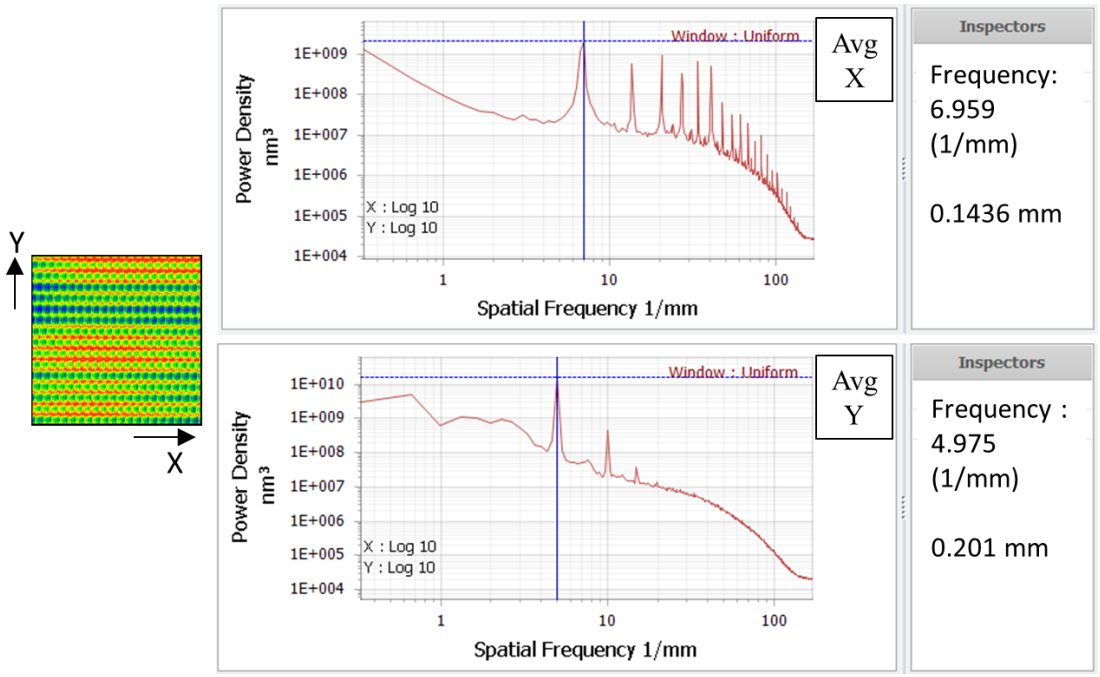

FIGURE 43: 1D – PSD plot of Medium ground CVD sample (raster configuration)

In the X-direction the PSD plot in Figure 43 showed a prominent first peak at 6.959 (1/mm) corresponding to a spatial wavelength of 143.6 µm which is approximately the feed per revolution. Harmonics of this frequency are also seen. In the Y-direction the dominant peak is at the stepover of 200 µm. For the spiral ground surface, the PSD plots shown in Figure 44 are much more complex than the raster configuration.

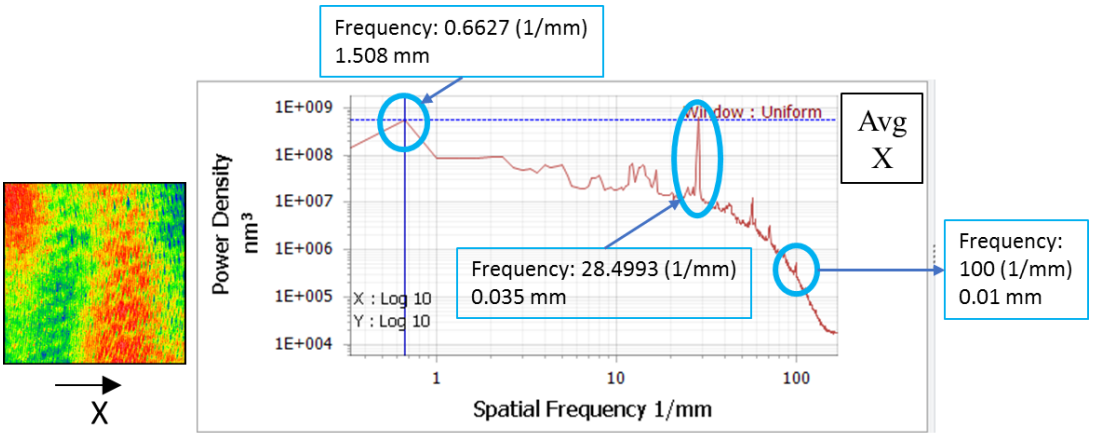

FIGURE 44: 1D – PSD plot of Medium ground CVD sample (spiral configuration)

The PSD is only analyzed in the X-direction. The first peak of the average PSD of traces in the X-direction is at 1.508 mm. The long wavelength pattern can be seen in the height map and its origin is not known. The fact that this wavelength matches that reported for the Makino is merely an artifact of low frequency resolution at long wavelength. For this case and for the case shown in Figure 29, the apparent periodic patterns are near the Nyquist limit and so both are very coarsely identified at a wavelength of 1.508 mm. A second peak is seen at 35 µm. This does not correlate to the parameters used for the grinding test. More analysis of the kinematics of the grinding motion with both the wheel and workpiece rotating would be required to identify its source. There is however also a small peak at 10 µm wavelength that correlates to the feed per revolution of the workpiece (1 mm/minute at 100 rpm).

Figure 45 shows the roughness plots for the finish ground surfaces using both raster and spiral configurations.

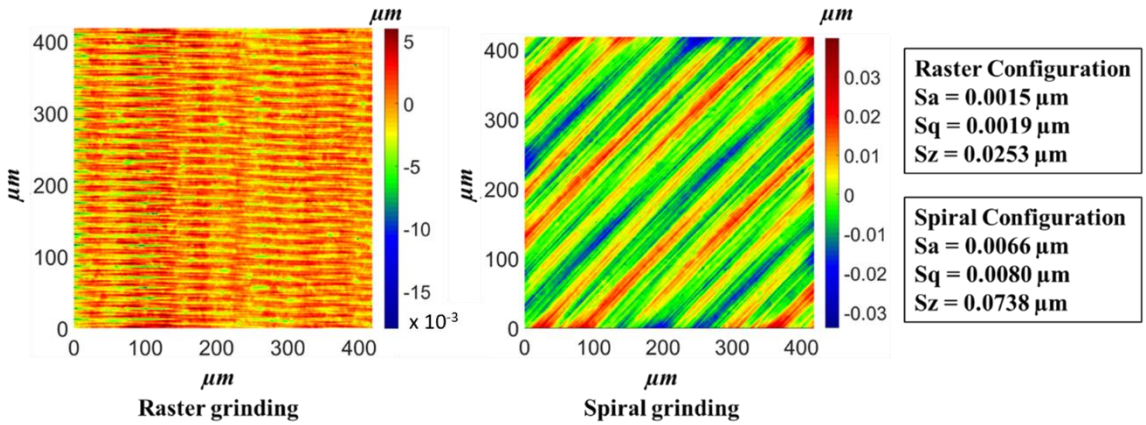

FIGURE 45: CSI roughness height map of CVD grade (finish ground)

The average estimate roughness parameter values were 0.0015 µm Sa, 0.0019 Sq µm and 0.0253 µm Sz for the raster ground surface while the roughness parameters for the spiral ground surface were 0.0066 µm Sa, 0.008 Sq and 0.0738 Sz. Figure 45 shows grinding marks in the raster ground surface with a periodicity equal to the feed per rev of the wheel (14.7 µm/rev). In the spiral ground surface, the dominant periodic pattern has a wavelength of approximately 50 µm, equal to the feed per workpiece rotation (5 mm/min feed at 100 rpm). The corresponding waviness maps are shown in Figure 46. It was also observed that the height amplitudes of waviness features were nearly an order of magnitude lower in the raster ground surface as compared to that of the spiral ground surface.

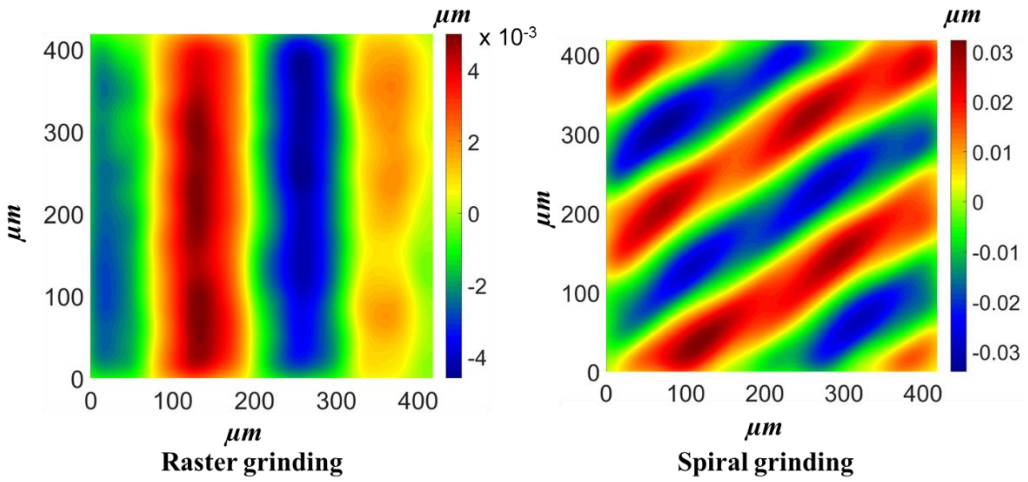

FIGURE 46: CSI waviness height map of CVD grade (finish ground)

The PSD plots for raster ground surface using finish parameters are as shown in Figure 47 with the X-direction aligned along the feed direction and the Y-direction being the stepover direction.

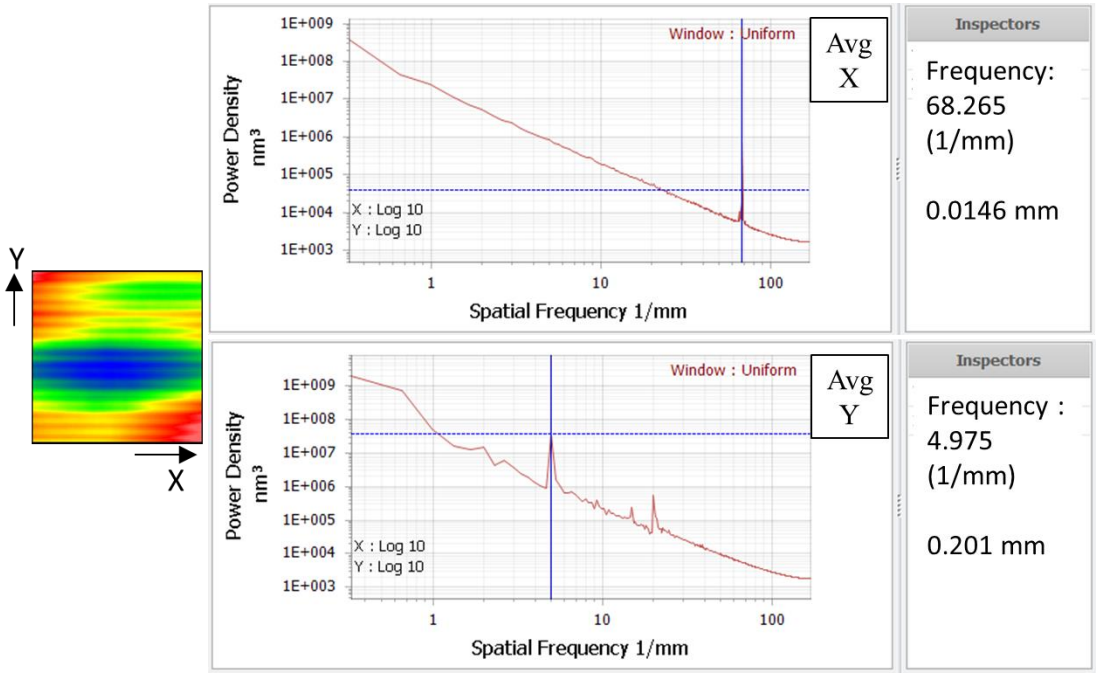

FIGURE 47: 1D – PSD plot of Finish ground CVD sample (raster configuration)

As in previous raster grinding, the PSD plot in X direction (Figure 47) showed a peak at the feed per revolution. The Y-direction PSD plot showed peaks at the step over and its harmonics.

The PSD plot for finish ground CVD surface using spiral configuration is shown in Figure 48. Due to workpiece rotation, the resultant direction of forces and material removal is continuously changing. Hence the PSD plot also changed with workpiece rotation. The PSD plots in Figure 48 were acquired along the radial direction which is aligned with X in the Figure. The PSD plot showed a peak corresponding to the tool feed per rotation of the sample at 50 µm. In addition, there were other peaks at 2.65 (1/mm) and its harmonics along radial directions from the center. These peaks did not correspond to any of the parameters used during the grinding test and hence was hypothesized that this was result of the more complex kinematics of the cutting operation. Further analysis with different parameters are required to more fully understand the PSD.

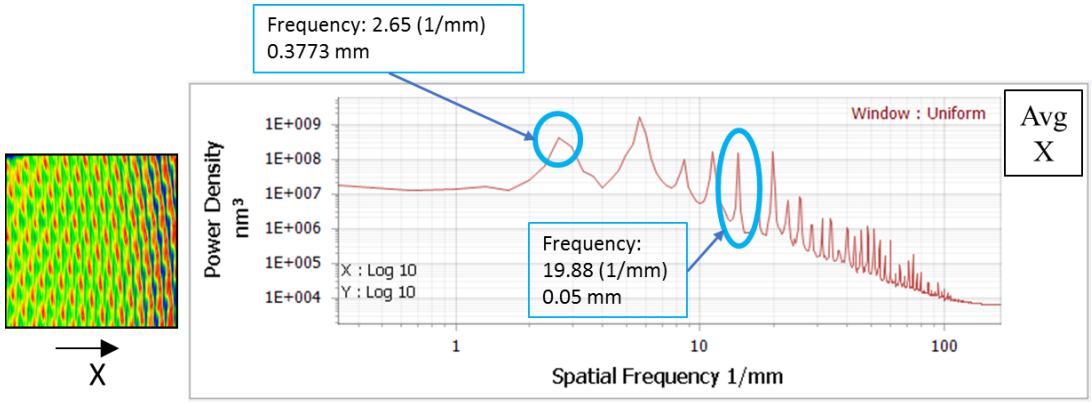

FIGURE 48: 1D – PSD plot of Finish ground CVD sample (Spiral configuration)

4.4.2 Reaction bonded grade:

The reaction bonded is a two-phase material with an internetwork of silicon and silicon carbide phases formed by a chemical reaction between graphite and silicon. The sample used for this test was acquired from L3. The sample was ground using the parameters from Chapter 2 using the raster configuration with one-inch diameter wheels. One side was ground using rough and medium parameters and second side was first ground with rough and medium parameters and then finished with the finish grinding parameters. SEM images acquired from a rough ground region are as shown in Figure 49.

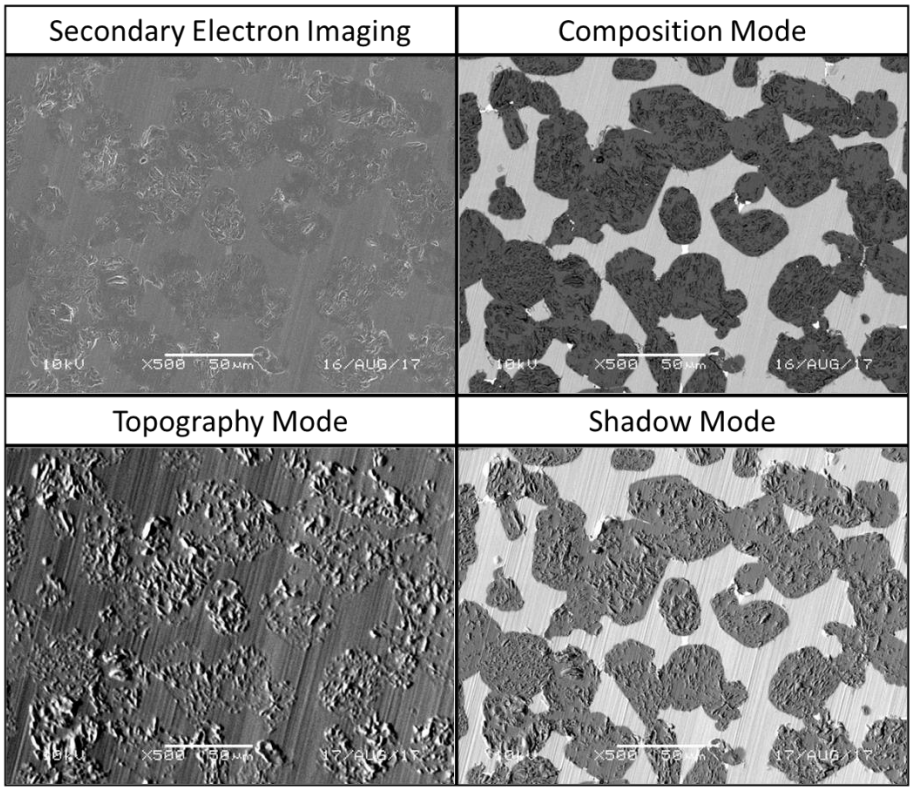

FIGURE 49: SEM images of rough ground RB samples

Both the secondary electron imaging and topography modes showed that certain regions of the sample appeared to arise from a more brittle fracture material removal process which others appeared to arise from a more ductile process. The composition

mode showed the presence of two phases, silicon and silicon carbide. Comparing all these images with shadow mode, it was concluded that material removal mechanics on the silicon phase was dominated by ductile deformation while the silicon carbide phase underwent material removal by brittle fracture. This produced the striking grain/phase relief shown in the images.

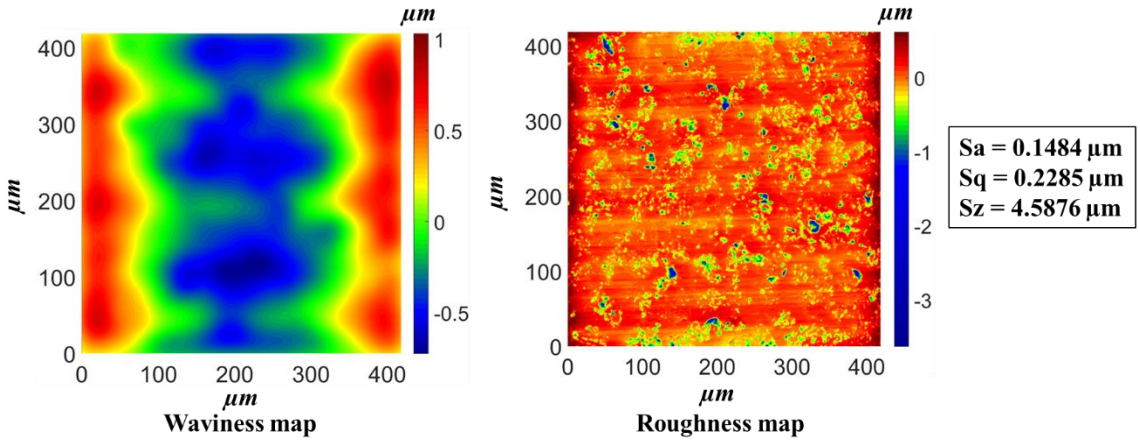

FIGURE 50: CSI height map of Reaction bonded grade (Rough ground)

The heightmaps acquired from a CSI measurement using a 20x objective are shown in Figure 50. The waviness map showed the waviness present due to the step over while the roughness map indicated presence of brittle fracture. The average estimates of roughness parameters were 0.1464 ± 0.0091 µm Sa, 0.2268 ± 0.0315 µm Sq and 4.8187 ± 1.2523 µm Sz.

The PSD plots shown in Figure 51 were acquired using 2.75x objective on the CSI with X aligned along the feed direction and Y in the stepover direction. As in previous cases, the average PSD plot of the traces in the X-direction showed a prominent peaks at the feed per revolution of the wheel and its harmonics. The average PSD plots of the traces in the Y direction showed peaks at the step over of 500 µm and its harmonics.

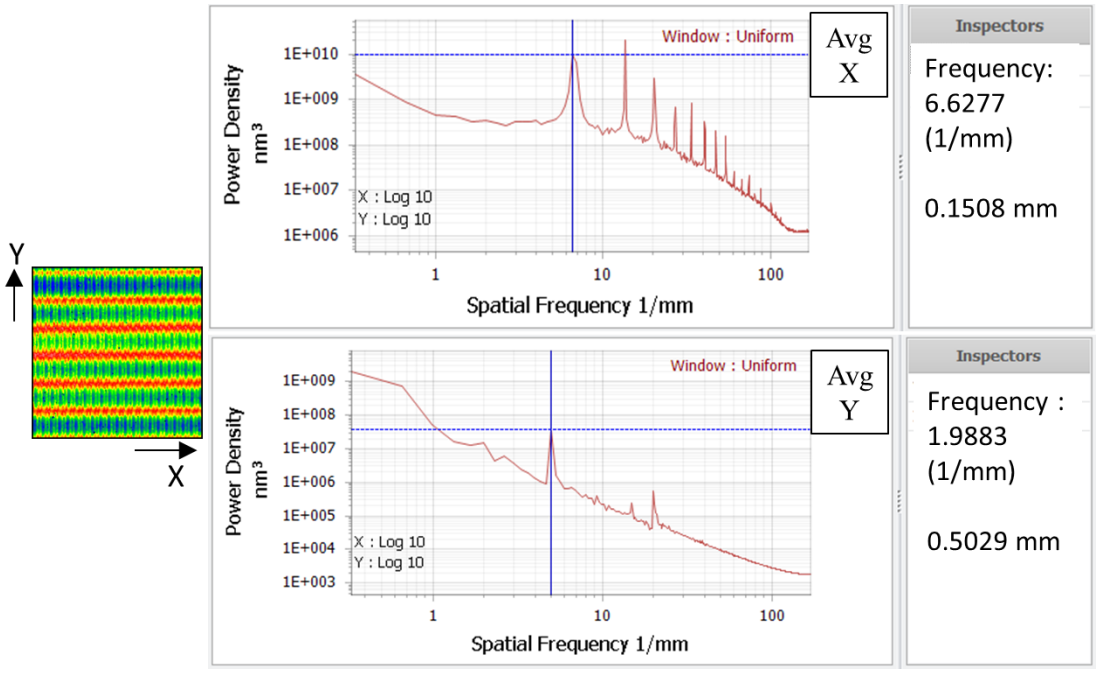

FIGURE 51: 1D – PSD plot of Rough ground reaction bonded sample (raster configuration)

The SEM images of medium ground surfaces (Figure 52) showed similar features to those observed in the rough ground surface. There was a continuous change in surface generation mechanics between brittle fracture in the SiC phase and ductile deformation in the silicon phase.

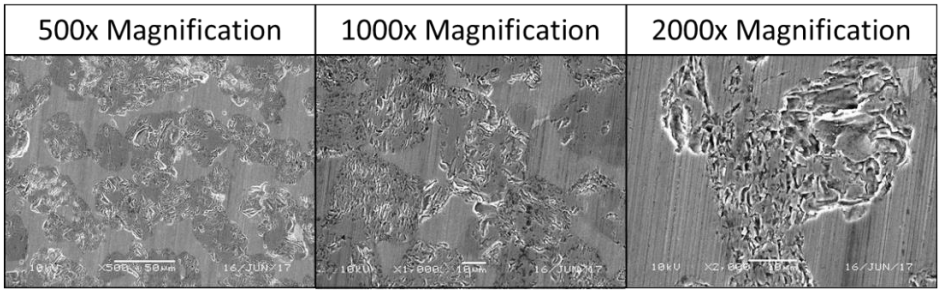

FIGURE 52: SEM images of medium ground RB samples

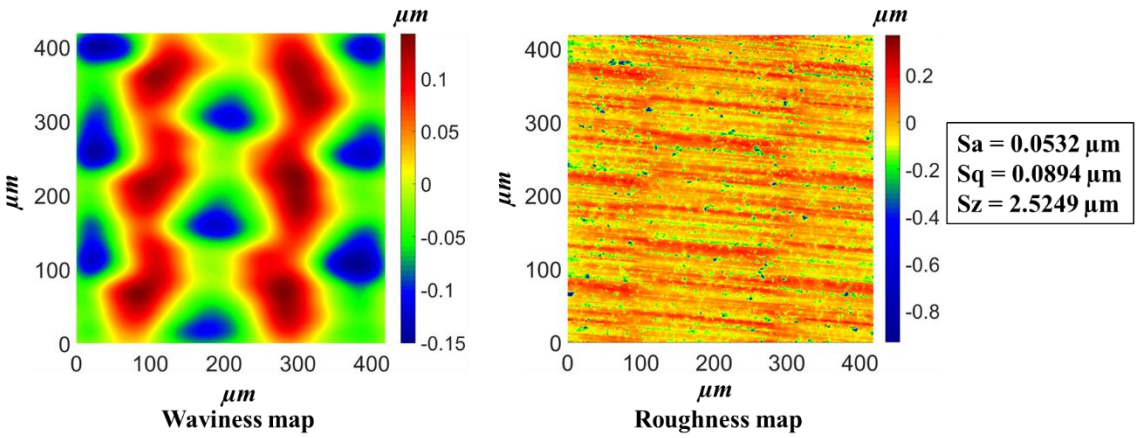

FIGURE 53: CSI height map of Reaction bonded grade (medium ground)

The CSI images using 20x objective are shown in Figure 53. The waviness map in Figure 53 showed the waviness features due to the step over and the feed per revolution. The roughness map showed grinding marks in the horizontal direction. The average estimates of roughness parameters were 0.0561 ± 0.0043 µm Sa, 0.0960 ± 0.0182 µm Sq and 3.0061 ± 0.8323 µm Sz.

SEM images of the finish ground surface are shown in Figure 54.

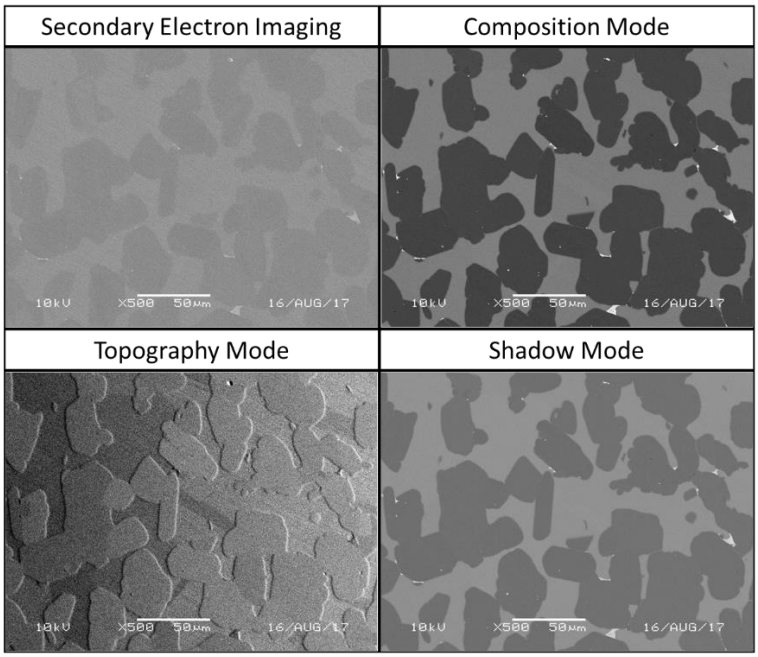

FIGURE 54: SEM images of finish ground RB samples

Comparing composition mode with shadow mode and secondary electron imaging mode, it was concluded that both silicon carbide and silicon phases were generated by material removal through ductile deformation. The absence of any surface fracture indicated that there was no, or very little brittle fracture involved. Comparing topography mode with composition mode, it was observed that, there were step like features between the silicon carbide and silicon phases. Since silicon carbide is significantly harder than silicon in terms of material properties, it was hypothesized that, during the ductile dominated material removal process, silicon experienced a higher material removal rate than silicon carbide phases. This behavior is similar to the surface interaction experienced by silicon infiltrated silicon carbide grade that was ground on the Makino and discussed in section 4.2.

The surfaces were further studied using a CSI measurement with a 2.75x objective. PSD plots of the surface are shown in Figure 55. Again, the X direction is aligned with the feed and the Y-direction is aligned with the stepover. In the X-direction the dominant peaks are at the feed per revolution and its harmonics. In the Y-direction the dominant peaks are at the stepover and its harmonics.

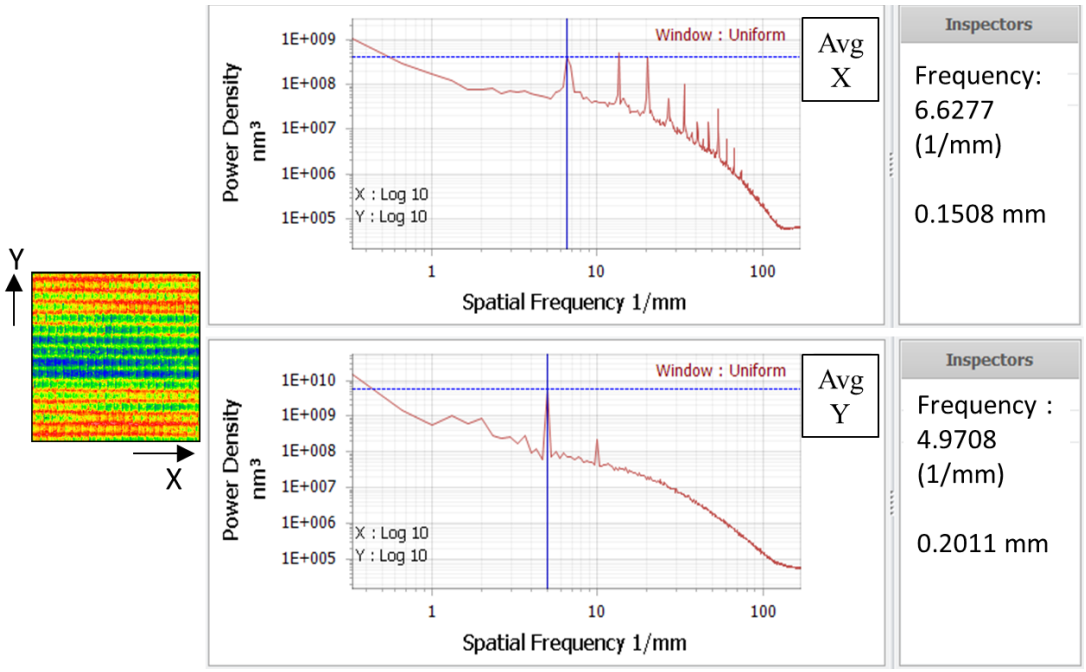

FIGURE 55: 1D – PSD plot of Medium ground RB sample (Raster configuration)

Figure 56 shows a CSI height map acquired using a 20x objective.

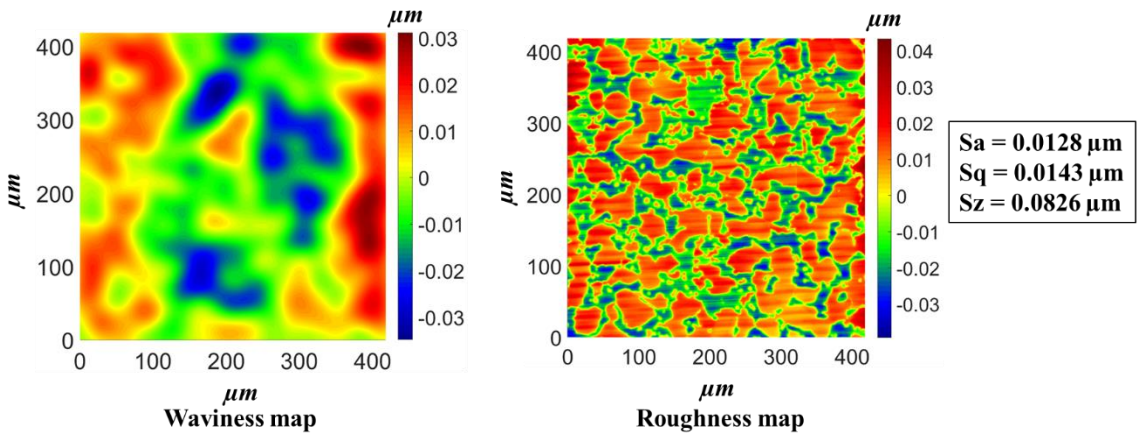

FIGURE 56: CSI height map of Reaction bonded grade (finish ground)

Due to the height difference between the silicon and silicon carbide phases as seen in SEM images (Figure 55), the roughness map showed the silicon carbide phase at a greater height than the silicon phase. These step changes in height dominated the surface roughness resulting in higher roughness values when compared to CVD or CVC grades. The average estimates of roughness parameters were 0.0145 ± 0.0010 µm Sa, 0.0164 ± 0.0013 Sq µm and 0.1353 ± 0.0862 µm Sz. The presence of step-like feature between the two phases is also reflected in the waviness map.

Finally, PSD plots generated with the 2.75x objective on the CSI and are shown in Figure 57.

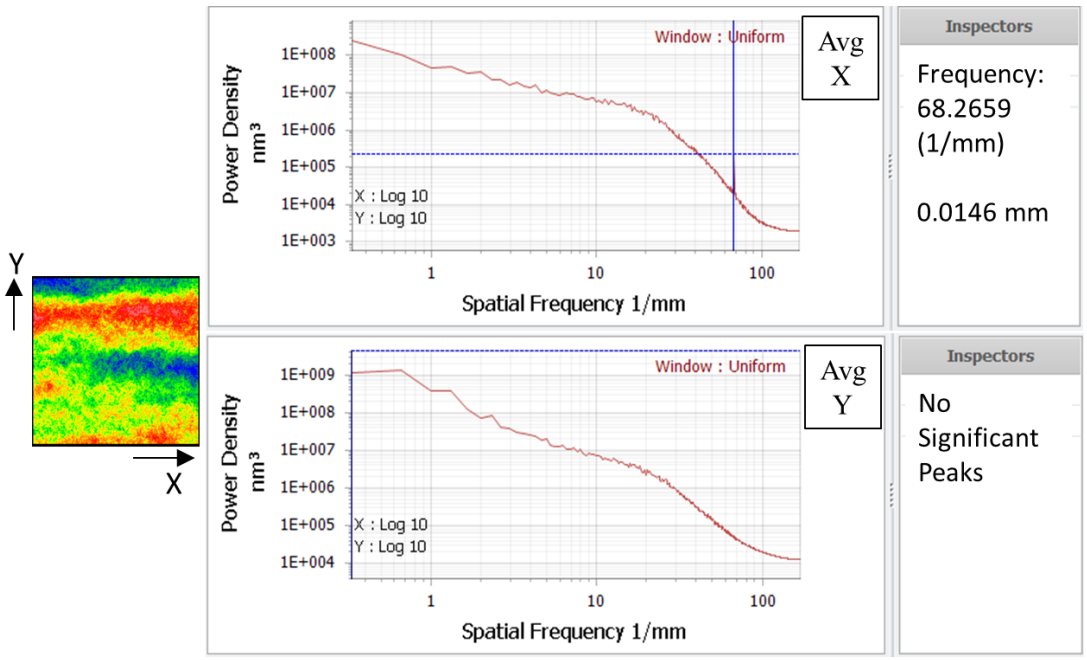

FIGURE 57: 1D – PSD plot of Finish ground RB sample (raster configuration)

The X-direction PSD plot showed a peak at 68.2659 (1/mm) which corresponded with the feed per revolution. There were no significant peaks in the Y-direction likely because of the irregular spacing of the silicon and silicon carbide phases.

This chapter discussed the surface results from grinding different grades of silicon carbide under identical grinding conditions using different configurations. The surfaces were studied using SEM and CSI to provide a baseline understanding of the nature of interaction during grinding in different grades of silicon carbide. The next chapter discusses the subsurface analysis conducted using MRF spotting technique in different grades of silicon carbide.

CHAPTER 5: RESULTS – SUBSURFACE DAMAGE ANALYSIS USING MRF SPOTTING TECHNIQUE

5.1 Introduction

The procedure to conduct MRF spotting technique and the theory behind the method of analyzing subsurface damage depth using this technique were discussed in Chapter 2. CSI measurements were acquired using the 20x objective at the base of the spots using the procedures discussed in Chapter 3 and the data were processed using MATLAB with codes available in Appendix A. Average roughness parameters Sa, Sq and Sz at the base of each spot were calculated as per ISO 25178-2-2012 [53] and averaged as per ISO 4288-1996 [54]. The evolution of roughness parameters was studied against spotting time to characterize the subsurface damage present the sample. After acquiring the roughness data using the 20x objective, the spots were measured using 2.75x objective CSI to measure the height of each spot. The analysis presented in this chapter estimates the subsurface damage using three major assumptions.

1.) The induced damage from MRF spotting process during the tests is negligible. Hence the MRF spotting process is assumed to produce surfaces that are ideally free from damage.
2.) The unidirectional fluid interaction between the MRF ribbon and the ground surface causes an imprint of the MRF spotting process. It is assumed that this imprint does not affect the subsurface damage results.
3.) The MRF spots with different spotting times are made at different angles on the sample. It is assumed that the presence and direction of the raster marks from the

grinding process do not affect the fluid interaction with the ground surface during the MRF spotting process.

4.) MRF spots with different spotting time are made at different locations on the sample and the surface roughness at the base of each spot is studied to estimate subsurface damage. Since the spots with different spotting time were not made at the same location to study the subsurface damage characteristics, it is assumed that the subsurface damage is homogenous across the entire ground area.

5.2 Subsurface damage analysis of samples ground on Makino A55

CVC, CVD and direct sintered samples that were ground in Makino A55 were tested using the MRF spotting technique to study the subsurface characteristics in the ground samples. Since this was a preliminary study to test the method in different grades, the spotting time was varied between 1 and 16 minutes. A maximum spotting of 16 minutes was selected based on previous study conducted on CVD grade silicon carbide in [32].

5.2.1 Chemical Vapor Composite (CVC) grade

Subsurface damage analysis was done for rough, medium and finish ground surface. 10 spots were made for each ground area with the spotting time varied as 1, 2, 3, 4, 6, 8, 10, 12, 14 and 16 minutes. Zero spotting time results were obtained from the roughness of the ground surface before spotting. Figure 58 shows the evolution of the roughness parameters versus spotting time plot for the spots made on the rough ground surface.

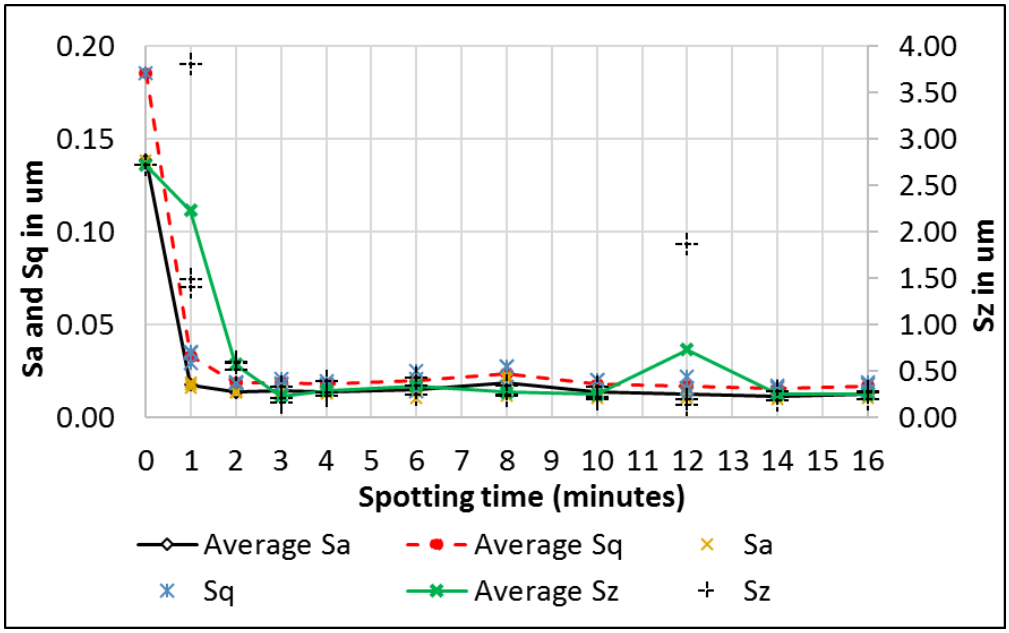

FIGURE 58: Spotting time vs Roughness parameters (Rough ground CVC)

When spotting rough ground CVC sample, the MRF spots remove grinding raster marks, surface fracture and subsurface damage. Hence, the roughness plots reach a stable value when all three sources of roughness are removed from the sample. Figure 58 shows a significant drop in Sa and Sq values after 1-minute which indicated that majority of surface damage was removed along with some of the underlying subsurface damage in 1 minute. The Sa and Sq values continued to decrease at a slower rate for longer spotting times, and all three parameters reached stable values between the 2-minute and 3-minute spotting time. Hence, we hypothesize that most of the subsurface damage was removed after a spotting time of 3 minutes. The height of the 3-minute spot was 3 µm. The roughness parameters continue to be stable after 3 minute-spot without any significant change. However, there is a small jump in the roughness parameters in the 12-minute spot. The CSI image revealed a pit in this spot. Thus, it could be concluded that majority

of the subsurface damage is present up to a depth of 3 µm but that additional damage and/or a material defect was detected at a depth of 10.5 µm (12-minute spot).

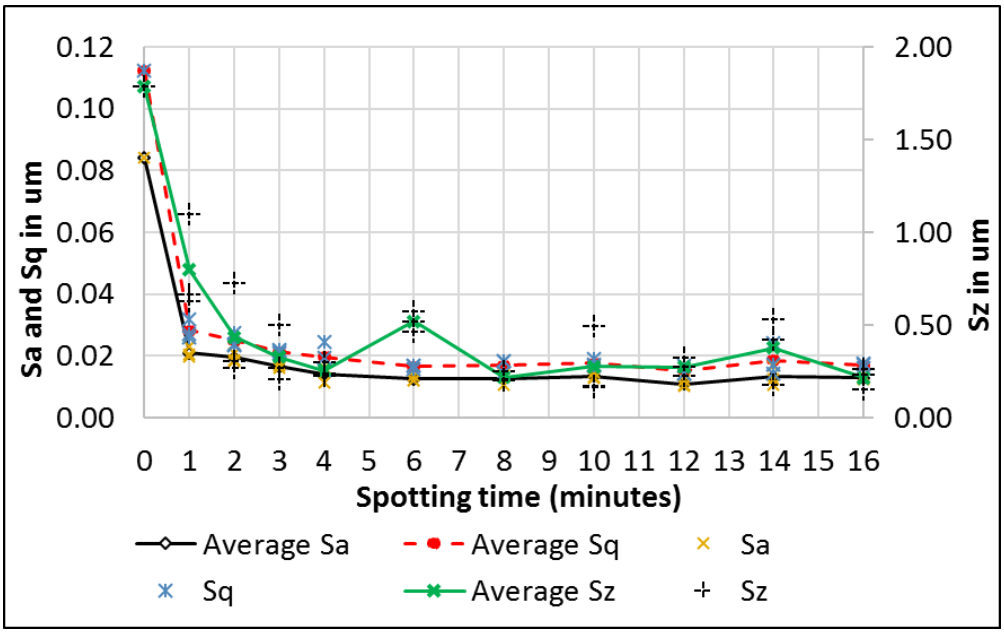

FIGURE 59: Spotting time vs Roughness parameters (Medium ground CVC)

Similarly, Figure 59 shows the roughness values at the base of spots of different spotting time on the medium ground CVC sample. Similar to the rough ground sample, the parameters Sa and Sq are significantly reduced after only a 1-minute spotting time. By contrast, Sz continues to drop rapidly up to a 2-minute spotting time. This indicated that majority of surface damage along with some subsurface damage were removed between 1-minute and 2-minute spot. From the 2-minute to 4-minute spotting time, all three roughness parameters continued to decline at a lower rate. Analysis of images from CSI measurements of surfaces at the base of 2-minute to 4-minute spots showed that the surfaces were still dominated by raster patterns from grinding. The slow decline in roughness values is attributed to the polishing of raster marks from the ground surface.

These results reveal that majority of the surface and subsurface damage was present to a depth of 1.7 µm (2-minute spot). However, there is a small spike at the 6-minute spot which correlated to the presence of a pit in the CSI images. Beyond this spotting time, the curve is stable. Hence, the observed subsurface damage depth was 1.7 µm with damage or material defects still being exposed to a depth of 6.5 µm (6-minute spot).

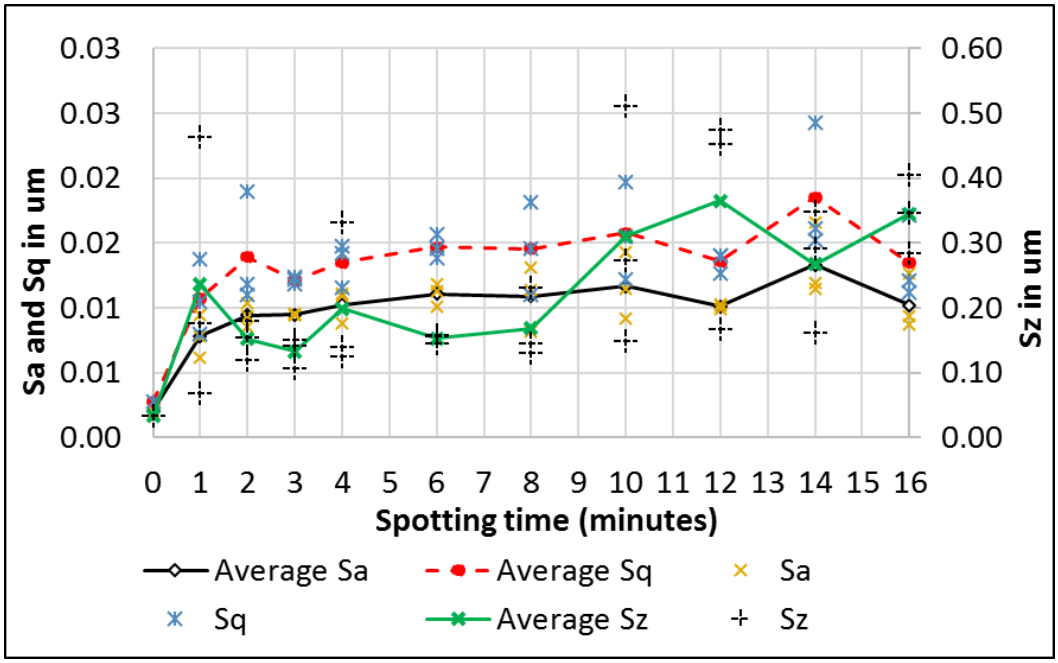

FIGURE 60: Spotting time vs Roughness parameters (Finish ground CVC)

Figure 60 shows the results of MRF spotting on the finish ground CVC sample. The pattern is not the same as for the rough and medium ground surfaces. Instead, it was observed that the roughness parameters increased and fluctuated with no discernable pattern. It was hypothesized that the initial spotting time of 1 minute was too long, and that most of the surface and subsurface damage was removed in less than 1 min. Experiments with shorter spotting time would be required to estimate the subsurface

damage in finish ground CVC sample. The overall increase in surface roughness values with greater spotting times was attributed to the unidirectional interaction between the MRF fluid and silicon carbide grains and this unidirectional interaction actually caused a roughening of the surface over the finish ground surface. Since the height of the 1-minute spot was approximately 0.7 µm, it was hypothesized that the subsurface damage in this sample was less than 0.7 µm.

5.2.2 Chemical Vapor Deposition (CVD) grade

Since the CVD grade was only finish ground, this technique was applied on the finish ground surface alone to study subsurface damage. Similar to the CVC grade sample, 10 spots were made for spotting intervals 1,2,3,4,6,8,10,12,14 and 16 minutes on a finish ground CVD grade sample.

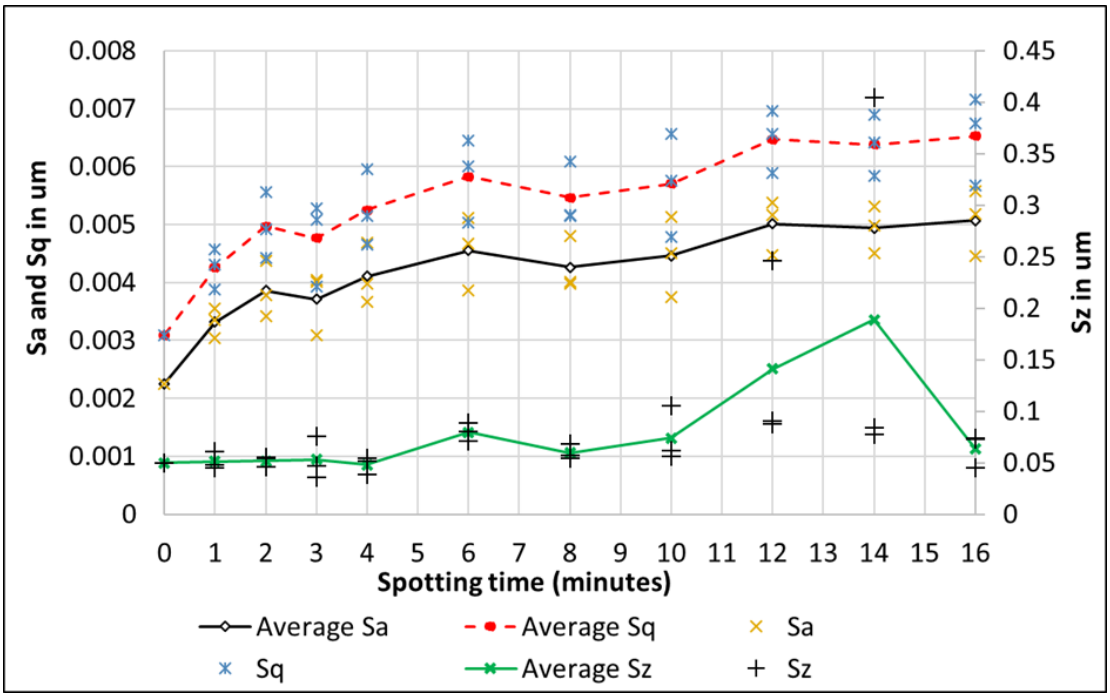

FIGURE 61: Spotting time vs Roughness parameters (Finish ground CVD)

Figure 61 showed that again there is no convergence of the roughness parameters. Hence, it was hypothesized that again all surface and subsurface damage was removed with much less than 1 minute of spotting time. Shorter spotting times were required to ascertain the subsurface damage present in the sample. A further spotting test was conducted using spotting intervals of 20 seconds between the 0-minute spot and 2-minute spot. Since the characteristic of the fluid had changed between the previous and the current experiment, the plot was standardized between the two experiments by plotting roughness values against spot heights up to 5 µm depth as shown in Figure 62.

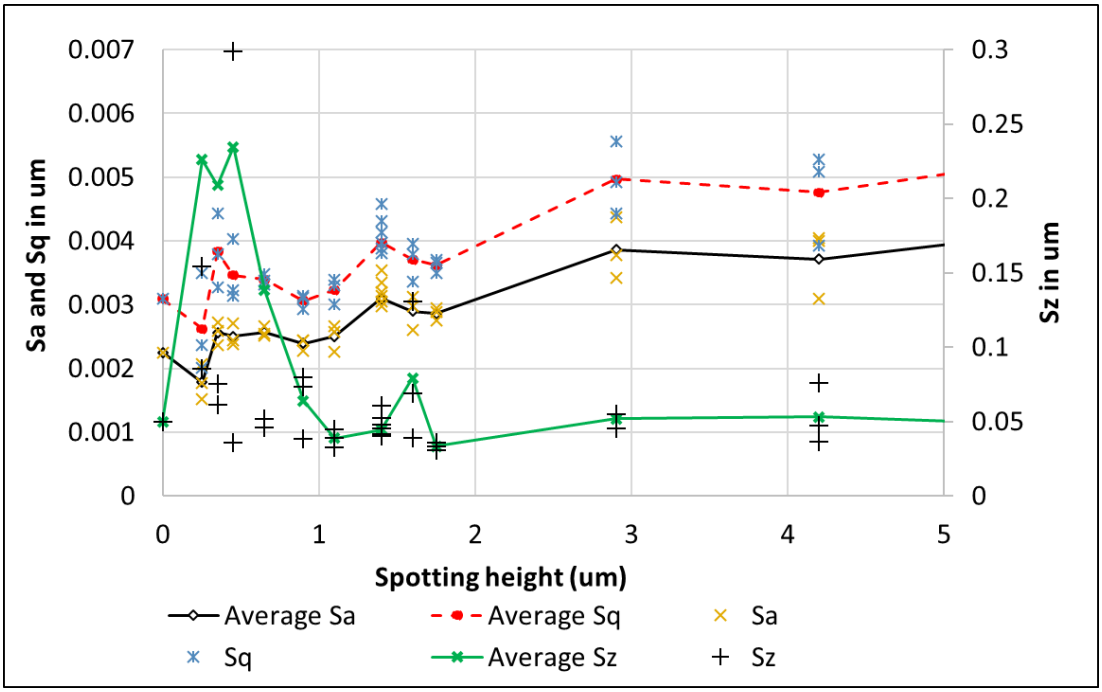

FIGURE 62: Spotting height vs Roughness parameters (updated) (Finish ground CVD)

In the updated plot (Figure 62), the roughness parameter Sz shows a significant increase in the roughness values after the 20-second spot while the parameters Sa and Sq gradually increase further even at the 40-second spot. We hypothesize that the top layers

of the surface generated by the grinding concealed damage below the surface. The spotting then exposed the damage causing the roughness parameters to rise and then converge to lower values. Parameters Sa, Sq and Sz reached stable values at approximately a spot depth of approximately 1.6 µm. Beyond this depth, minor fluctuations were observed in the roughness parameter values due to the nature of interaction between MRF fluid and the SiC. Hence, the approximate value of subsurface damage in this sample is 1.6 µm.

5.2.3 Direct Sintered Grade (DS)

Due to limitation in area available for spotting in the direct sintered sample, only 7 spots were made on the finish ground region of the sample with spotting intervals 1, 2, 3, 6, 9, 12 and 16 minutes. Figure 63 shows the spotting interval versus roughness data measured at the base of the spots.

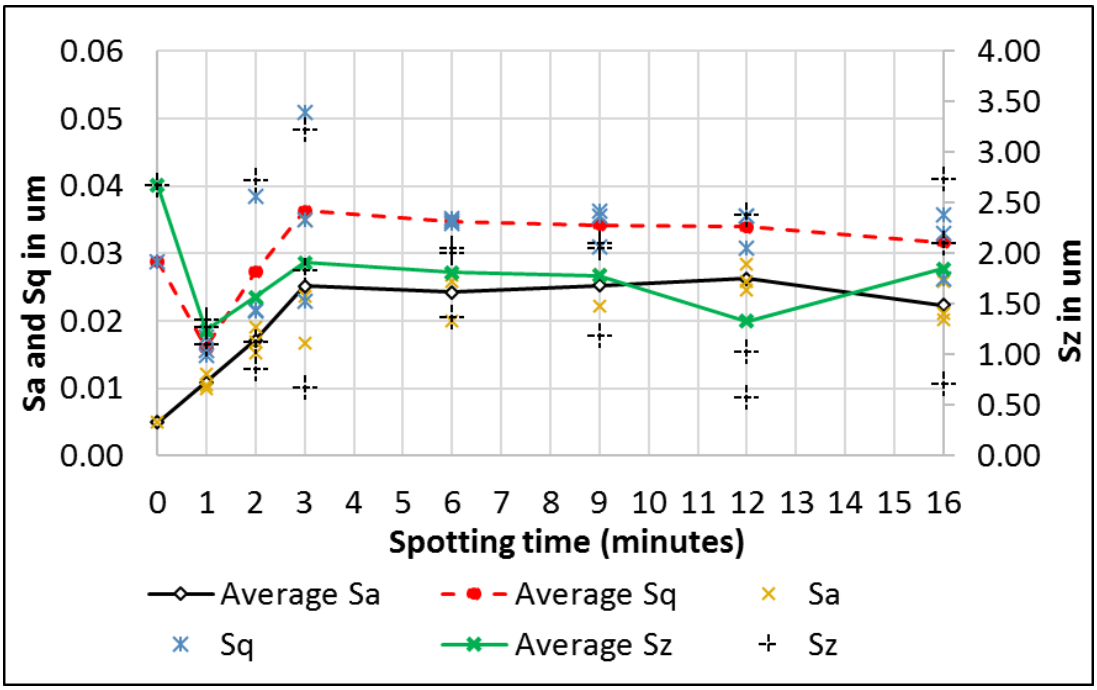

FIGURE 63: Spotting time vs Roughness parameters (finish ground DS)

No converging pattern was observed in Figure 63 and hence no information could be extracted from this test. Further analysis was required to understand the cause of this pattern. SEM images were made on 1, 2, 3 and 16-minute spots to study the nature of surface texture at the base of the spot. The SEM images are shown in Figure 64.

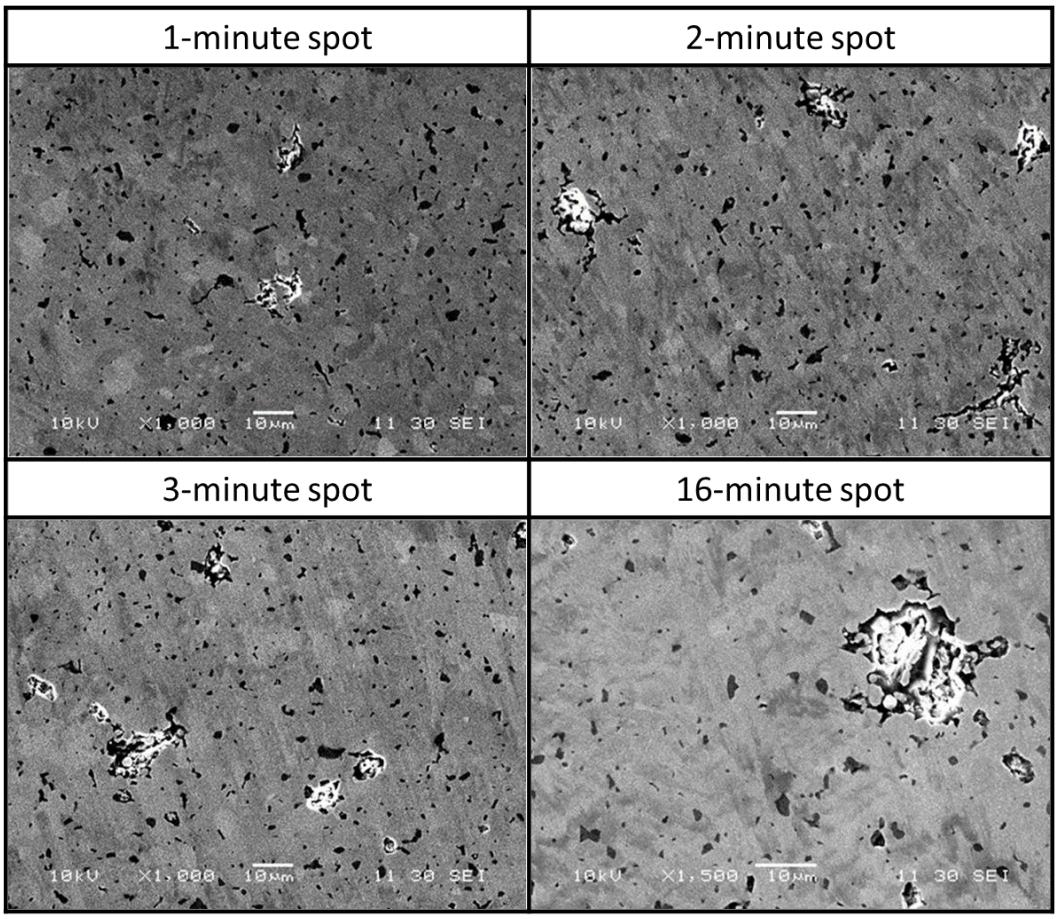

FIGURE 64: Analysis of base of spots in DS sample using SEM

Though the spotting does appear to expose some subsurface features in the SEM images, damages/defects could still be observed at the base of 16-minute spot. The height of the 16-minute spot was 10 µm. This led to two possible hypotheses, (1) the spotting interval chosen for the study was not sufficient to estimate the subsurface damage caused by the grinding, or (2) the presence of porosity and its interaction with the MRF spotting

process was skewing the results. Further study is required to study the feasibility of the process in direct sintered sample to estimate the subsurface damage.

5.3 Subsurface Damage Analysis of Samples Ground on Optisonic 1250X

CVD, silicon infiltrated and reaction bonded samples that were ground in the Optisonic 1250x were studied with the MRF spotting technique to estimate subsurface damage. Previous tests on samples ground on Makino A55 suggested that the choice of spotting time intervals was important for revealing damage. For this study, the spotting intervals were reduced based on results from the previous tests.

5.3.1 Chemical Vapor Deposited (CVD) Grade

The CVD samples were ground on the Optisonic 1250X using medium and finish parameters in the raster and spiral configurations.

For the medium ground sample, the spot times were varied from 0 to 9 minutes with the 0-minute spot corresponding to the as-ground surface before spotting. The first three spots were made at 20-seconds, 40-seconds and 1-minute. The spots from 1-minute to 9-minutes were made in 30 second intervals.

For the finish ground sample, the spotting times were varied between 0 and 6 minutes in intervals of 20 seconds.

Figure 65 shows the spotting interval versus roughness parameters for the medium raster-ground sample.

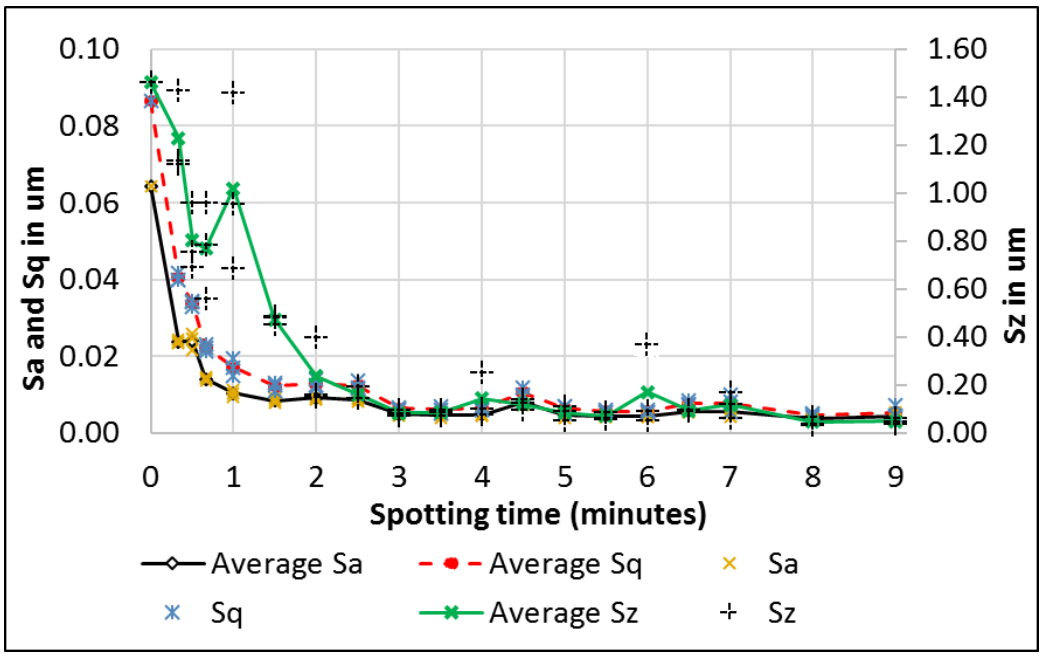

FIGURE 65: Spotting time vs Roughness parameters (CVD medium raster ground)

Sa, Sq and Sz initially show a steep decrease in the roughness for spotting times ranging from 0-minutes to 40-seconds. While the Sa and Sq parameters continue to decrease beyond 40 seconds, Sz increases again with a peak at the 1-minute spot. The spot depth associated with this spot time is 0.67 µm. This again suggested that removal of the top ground layer actually exposed some of the underlying damage in the sample. After 1 minute, the Sz parameter decreased again. All three parameters decreased and reached a stable value after 3 minutes of spotting. The depth of this spot was 2 µm. Beyond this spotting interval, the roughness parameters did not show any significant change. Thus, the damage depth in this sample was estimated to be approximately 2 µm. Figure 66 shows the MRF spotting plot for the medium ground sample using the spiral configuration.

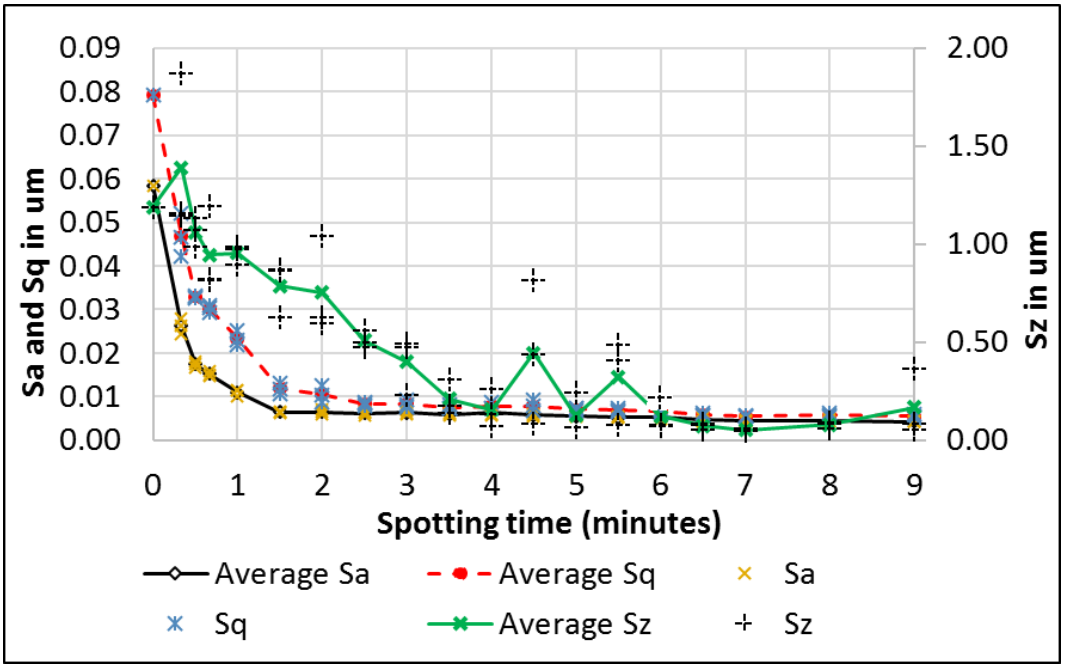

FIGURE 66: Spotting time vs Roughness parameters (CVD medium spiral ground)

Similar to the medium raster ground sample, the medium spiral ground sample also showed a drop in Sa and Sq values which reached stable values after 2 minutes of spotting time. This showed that majority of the surface features were removed by this stage. However, Sz showed a pattern different from those previously seen. Possibly due to initial exposure of subsurface damage, Sz peaked after 20-seconds. Beyond this spotting time, the value of Sz declined at a slower rate than previously observed, reaching a stable value at 4 minutes of spotting time. The corresponding spot depth was 2 µm. This characteristic of the curve also indicated that the concentrations of the subsurface damage features were high up to a depth of approximately 2 µm. The Sz parameter reached a stable value after 6 minutes of spotting. The spot depth at this time was 3 µm. Beyond this spotting time, there were minor fluctuations in the roughness values that are

attributed to the interaction of MRF process with grade of silicon carbide. Thus, the estimated value of subsurface damage for this sample was 3 µm.

Figure 67 shows the subsurface damage estimation plot for the finish ground surface using the raster configuration.

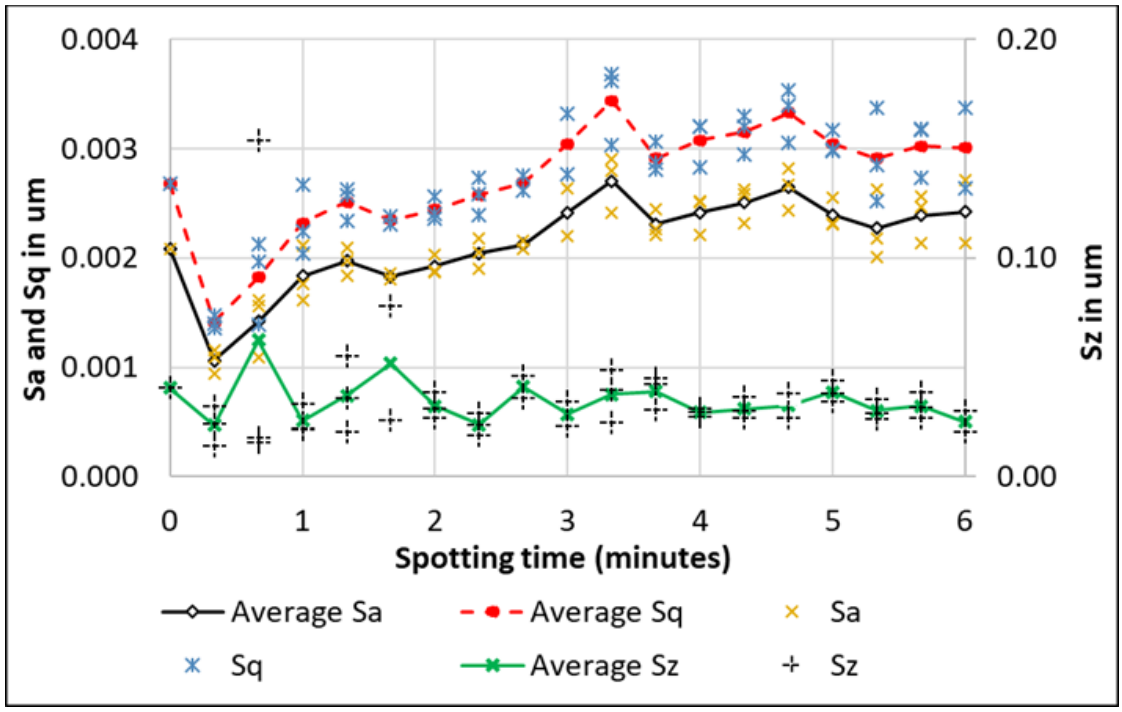

FIGURE 67: Spotting time vs Roughness parameters (CVD finish raster ground)

Figure 67 shows that there is a decline in the roughness parameter values from the 0-minute spot to 20-second spot. Beyond this point, there was no discernable pattern observed in the plot with minor fluctuations and a gradual increase due to interaction between the unidirectional flow of the MRF fluid and the sample surface. It was hypothesized that the subsurface damage depth was too small to be resolved in the 20 second spotting time. The spot height associated with the 20 second spot was

approximately estimated to be 0.17 µm. Hence the estimated value of subsurface damage is less than 0.17 µm.

Figure 68 shows the subsurface damage estimation plot for a finish ground sample ground using the spiral configuration.

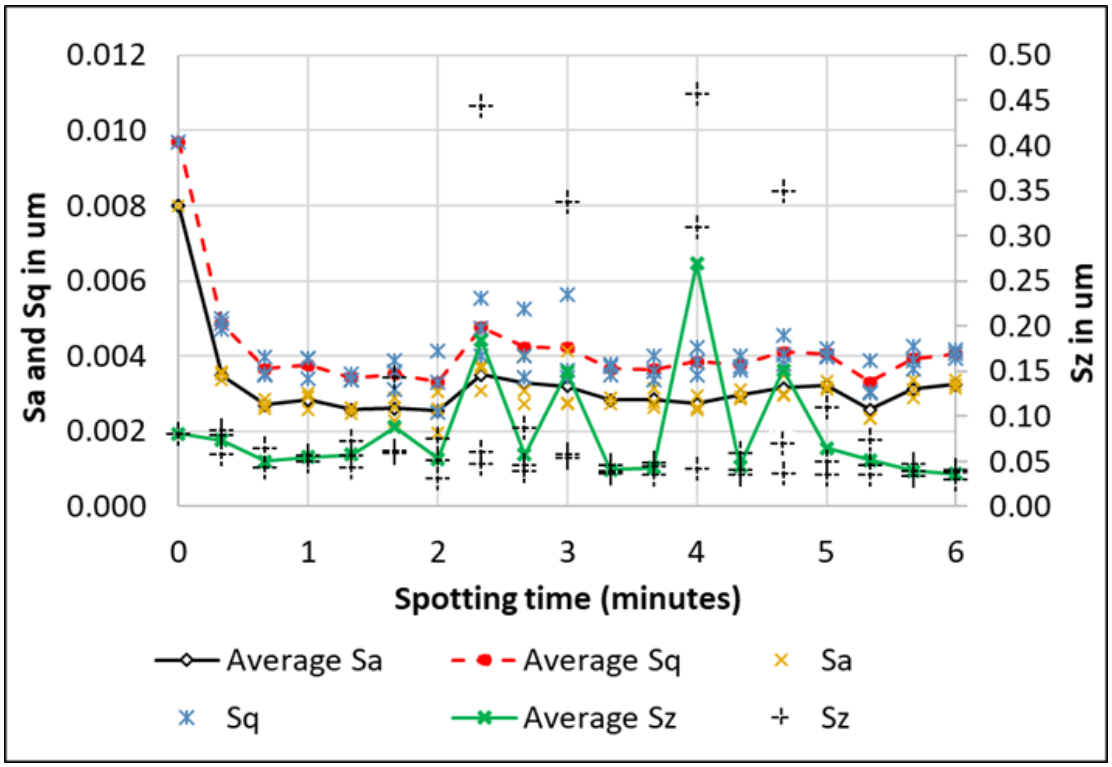

FIGURE 68: Spotting time vs Roughness parameters (CVD finish spiral ground)

Up to 2 minutes of spotting, there was no major variation in the value of Sz. However, the values of Sa and Sq showed a decline until 40 seconds of spotting time and then remained stable with increased spotting time. The spot height at 40 seconds was approximately 0.3 µm. In chapter 4, it was discussed that the roughness parameters of the finish spiral ground CVD surface were higher than that of finish raster ground surface. Since the Sa and Sq values dropped while the Sz showed no significant changes between the 0-minute spot and 40-second spot, it was hypothesized that the decline in Sa and Sq

was due to the removal of roughness features on the top layers of the surface. There was no discernable pattern in the Sz parameter for the entire range of spotting time. This led to two possible hypotheses, (i) the process of removing the roughness features from the surface also removed the subsurface damage present in the sample or (ii) the subsurface damage from the grinding process was insignificant and could not be measured by this technique. In both cases, it can be concluded that the subsurface damage present in the sample was less than 0.3 μm which corresponded to a spotting time of 40 seconds.

5.3.2 Reaction Bonded Grade

The reaction bonded grade is a two-phase material. Hence this is the first MRF spotting test in a silicon carbide grade with an intertwining network of two phases, silicon and silicon carbide. To explore how this grade would interact with MRF, the spotting times were varied from 20 seconds to 25 minutes with the 0-minute spot corresponding to the as ground surface before MRF spotting. The spotting intervals were varied by 20 seconds for spots less than or equal to a minute. The spotting intervals were separated by 30 seconds between spots for spotting times between 1 and 5 minutes. The interval was changed to 1 minute between 5 and 10 minutes. Beyond the 10-minute spot, the spotting times were varied as follows: 12, 15, 20 and 25 minutes.

Figure 69 shows the spotting time versus roughness parameter plots for MRF spots made on a finish ground reaction bonded sample for spotting times between 0 and 10 minutes. Figure 70 extends the plot with spotting time between 0 and 25 minutes.

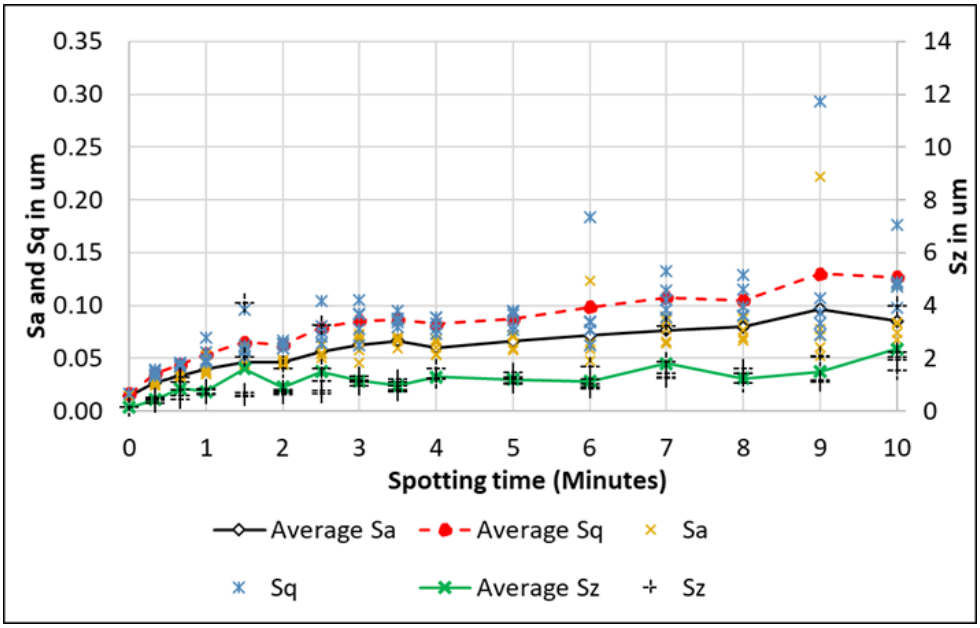

FIGURE 69: Spotting time (0 to 10 minutes) vs Roughness parameters (RB Finish Raster ground)

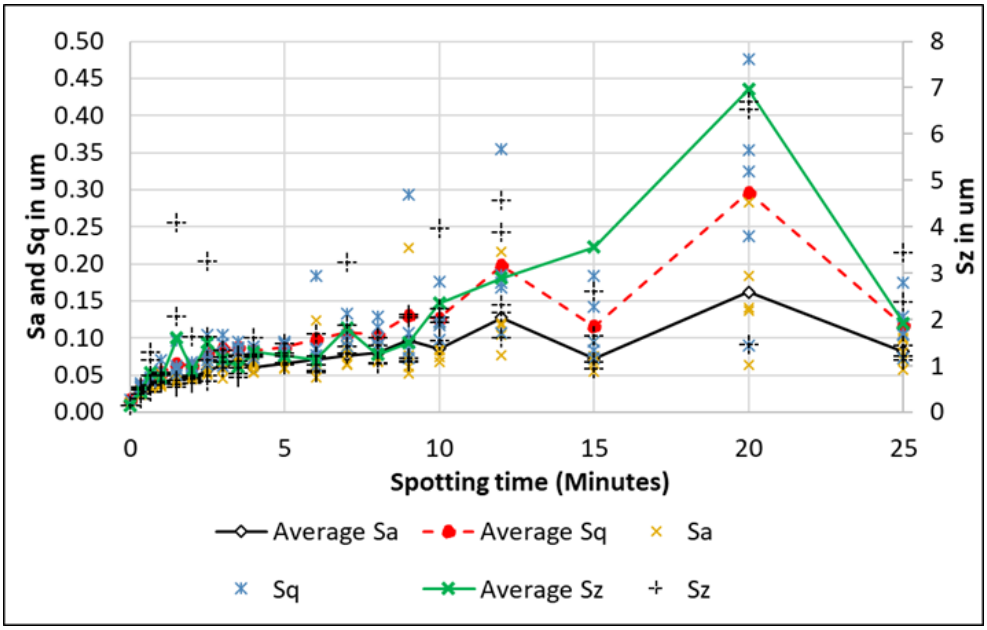

FIGURE 70: Spotting time (0 to 25 minutes) vs Roughness parameters (RB Finish Raster ground)

In Figure 69, it can be seen that all three roughness parameters, Sa, Sq and Sz, increase slowly with minor fluctuations between 0 to 10 minutes of spotting. Figure 70

shows the behavior beyond 10 minutes of spotting time. After 10 minutes, the fluctuations in the parameter values increased. There was no discernable pattern in the parameter variation except the gradual average increase. As discussed in chapter 4, the finish ground sample showed that there were step like features at the grain boundaries separating the silicon and silicon carbide phases either due to differential elastic recovery or due to different removal rates between the two materials.

It was hypothesized that the same phenomenon occurred during the MRF spotting process which increased the surface roughness values with increased spotting times. This hypothesis was based on the relative compliance of the two processes. The grinding wheels are quite stiff, and the wheel stiffness should suppress the phase height differentiation: a perfectly rigid wheel should make the step height difference zero. A more compliant tool would deform around the phases and lead to greater differentiation. The MRF process relies on a magneto-rheological fluid with viscosity and some stiffness, but likely much more compliant than a grinding wheel. Thus, it is hypothesized that the phase differentiation in MRF would be far greater than that seen in grinding.

The hypothesis is backed up by SEM images. Figure 71 shows SEM images from the base of 20-second, 5-minute and 25-minute spot. The corresponding spot heights are 0.3 µm, 5 µm and 26 µm.

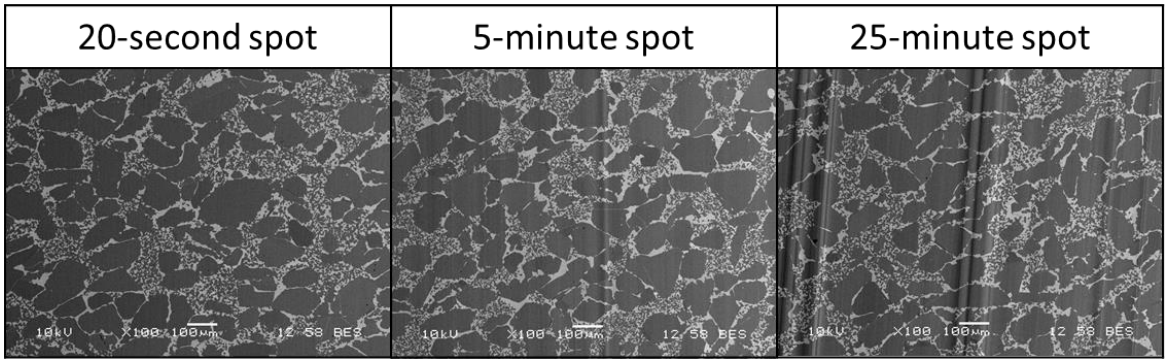

FIGURE 71: SEM analysis of spot base surfaces at different depths

The SEM images were taken at 100x magnification in shadow mode. In Figure 71, the SEM image of 20-second spot does not show any significant difference from the as-ground surface. The 5-minute spot surface showed linear features in the direction of the fluid flow. These features become much more prominent in the 25-minute spot. It was hypothesized that this was due to the combination of interaction between fluid and the surface due to the unidirectional fluid flow and the different removal rates between the two phases of the material. Further analysis of the 20-second spot was made using the SEM and the images are as shown in Figure 72.

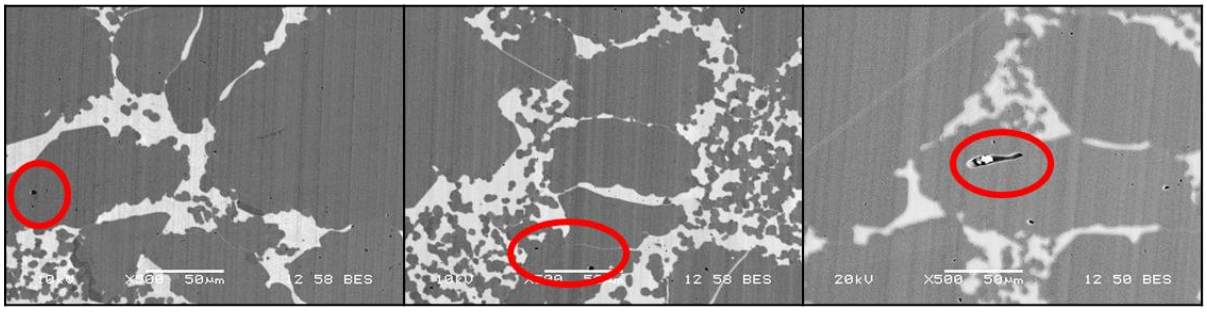

FIGURE 72: SEM images of 20-second spot surface (500x magnification)

Figure 72 showed SEM images of surface at the base of 20-second spot at 500x magnification. The images showed that the MRF spotting process removed top layers of the silicon carbide phase exposing subsurface damage. However, due to the presence/formation of step like features between the silicon and silicon carbide phases, the MRF spotting technique of characterizing subsurface damage using roughness parameters is not applicable for this grade. In addition, the results could also be significantly skewed by the presence of polishing marks caused by the unidirectional flow interaction between the fluid and sample surface.

This study was further explored to understand the nature of MRF process interaction with the reaction bonded grade. A reaction bonded sample finish ground using a raster configuration was full aperture polished with MRF. The machine was programmed to remove 1 µm uniformly across the surface. Figure 73 shows images from CSI measurement using a 20x objective before and after MRF polishing.

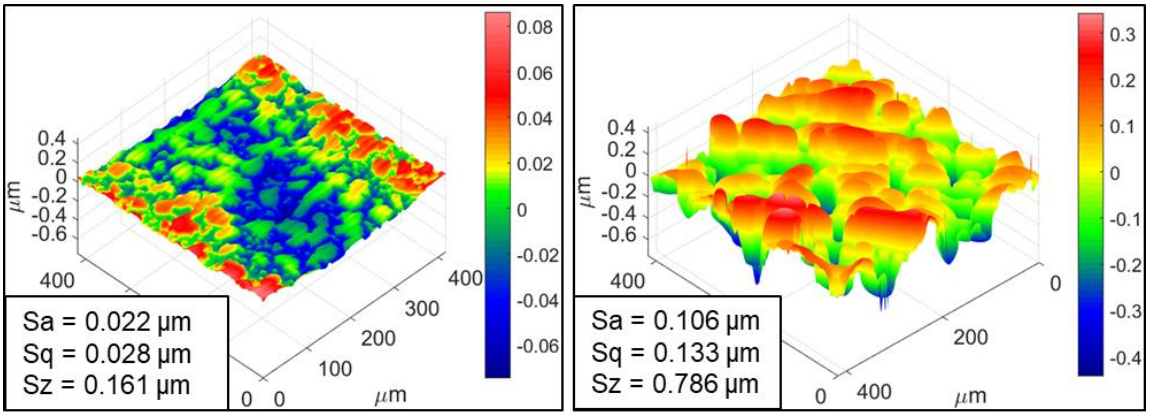

(a) (b)

FIGURE 73: CSI image of surface (a) before polishing (b) after 1 µm uniform polishing

The images and values presented in Figure 73 was after removing form (plane removed), and no filtering was done on the surface. Figure 73 (a) showed the step like feature between the silicon and silicon carbide phases after grinding. Comparing Figures 73 (a) and (b) showed that the MRF polishing process also removes silicon and silicon carbide at significantly different rates so that the step heights have significantly increased as denoted by the parameter Sz. This difference in removal rates between silicon and silicon carbide had significantly increased the surface roughness values. The roughness values increased when compared to the surface before polishing. This was also observed in the SEM images of the sample as shown in Figure 74 where the surface appears to have trailing marks left by MRF fluid in the direction of polishing.

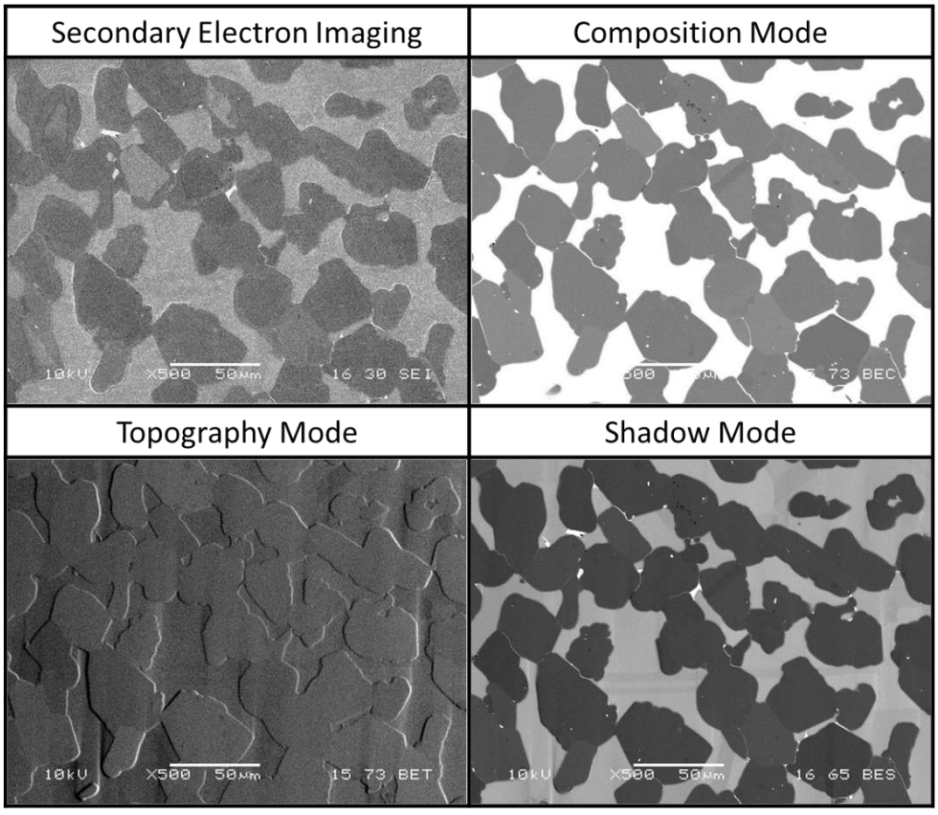

FIGURE 74: SEM images of MRF polished reaction bonded sample

Figure 74 shows the SEM image of MRF polished reaction bonded sample in all 4 SEM modes. The composition mode and shadow mode showed the boundaries between the silicon and silicon carbide phases. The topography mode showed the presence of step like features along with trailing marks in the direction of the fluid flow. This further validates the conclusion that the silicon and silicon carbide phases have different material removal rates.

The sample was then measured using 2.75x objective in the CSI and PSD plots were compared before and after polishing.

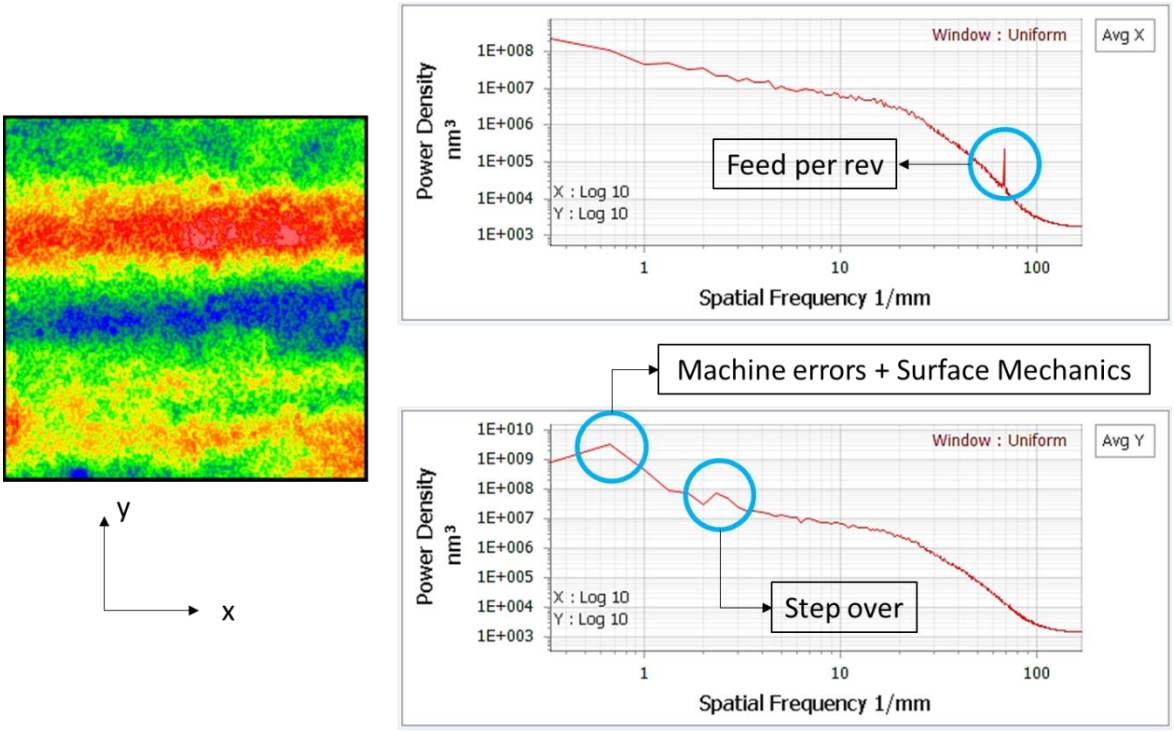

FIGURE 75: CSI 2.75x measurement with PSD plot (sample before polishing)

Figure 75 shows the CSI image under a 2.75x objective along with the PSD plots from the surface before polishing. The X-direction PSD showed a peak at the feed per revolution. The Y-direction PSD plots showed one peak caused due to step over per raster pass and the other peak at 1.5 mm as discussed previously.

In comparison, the CSI image of polished surface using a 2.75x objective was also acquired as shown in Figure 76.

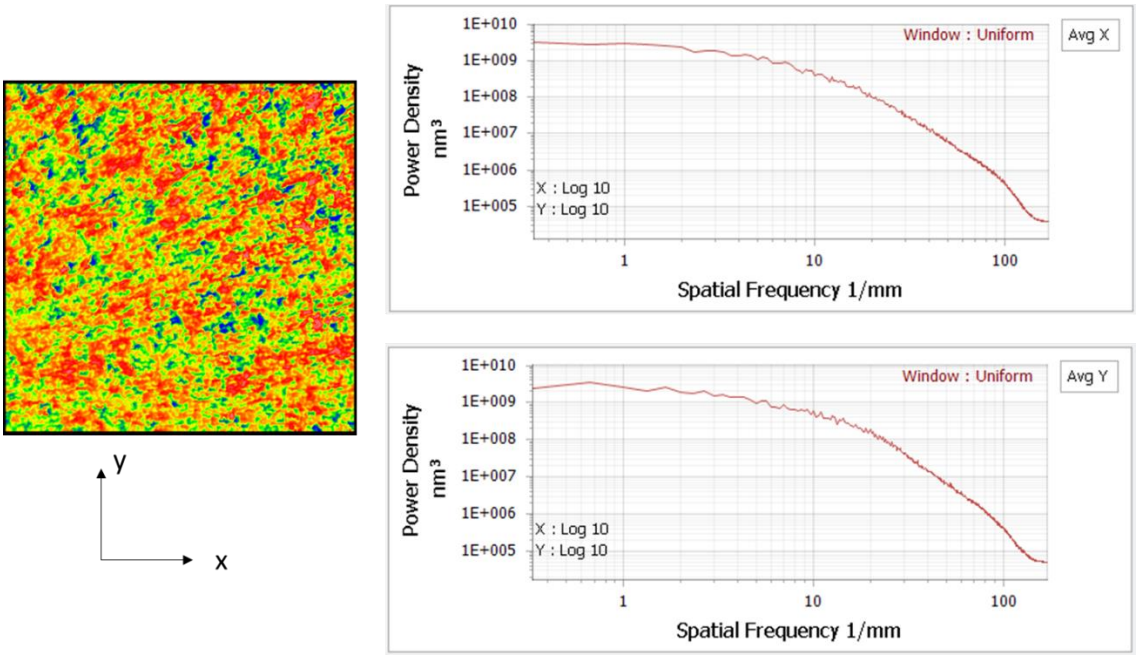

FIGURE 76: CSI 2.75x measurement with PSD plot (sample after polishing)

The PSD plots in Figure 76 did not show any significant peaks. Comparing the PSD plots from Figure 75 and Figure 76, it can be concluded that the MRF polishing process causes phase relief that leads to an increase in the roughness parameter values. It can be inferred from these results that the use of MRF in the conventional sense may not be the solution to either estimate the subsurface damage or polish the reaction bonded grade.

5.3.3 Silicon Infiltrated Grade

To further explore the feasibility of using MRF spotting technique to estimate subsurface damage, the method was also tested on the raster rough ground region in silicon infiltrated sample. Figure 77 shows the spotting time versus roughness parameters plot. Since this was a study to understand the interaction between MRF spot and sample

surface, the spotting intervals were widely spaced and varied from 0 to 20 minutes using 6 spots.

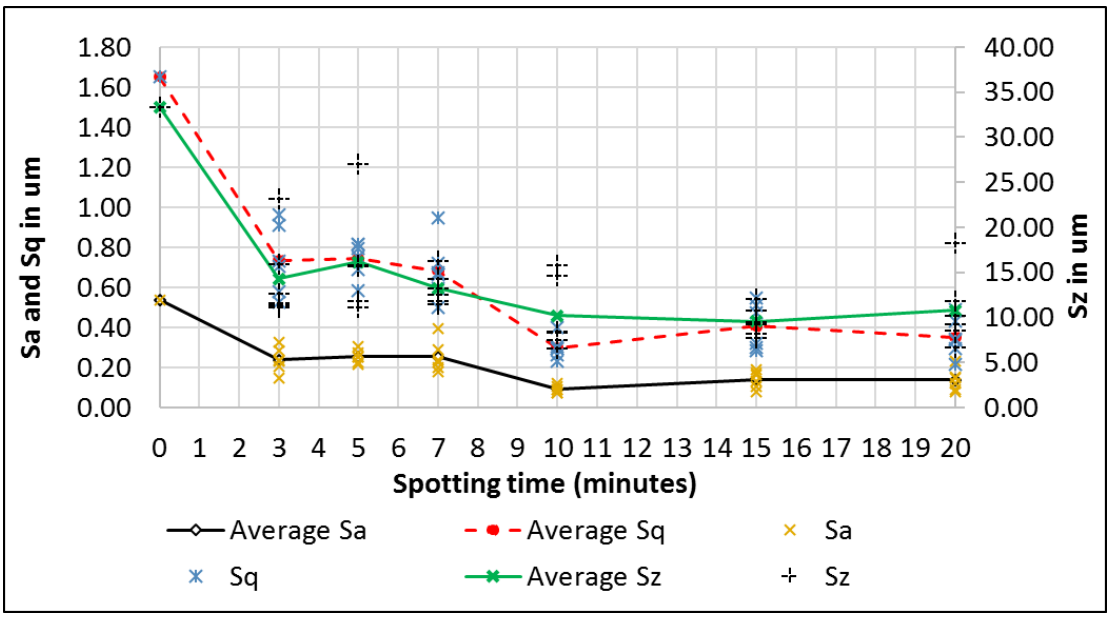

FIGURE 77: Spotting time vs Roughness parameters (silicon infiltrated rough ground)

From Figure 77, it was observed that there was a trend of declining values from 0-minute spot to 3-minute spot. All three parameters showed a significant change in roughness values during this decline. Beyond the 3-minute spot, the rate of change of roughness parameter values reduced and the parameter values were fairly constant after spotting for 10 minutes. However, even after 20 minutes of spotting, the magnitudes of these roughness parameters were significantly higher when compared to the roughness values at the base of spots in other grades of silicon carbide. After 20 minutes of spotting, the roughness parameter values were calculated to be 0.137 µm Sa, 0.352 µm Sq and 10.762 µm Sz. To study the surface interaction further, SEM images were taken at the base of 3-minute and 20-minute spot.

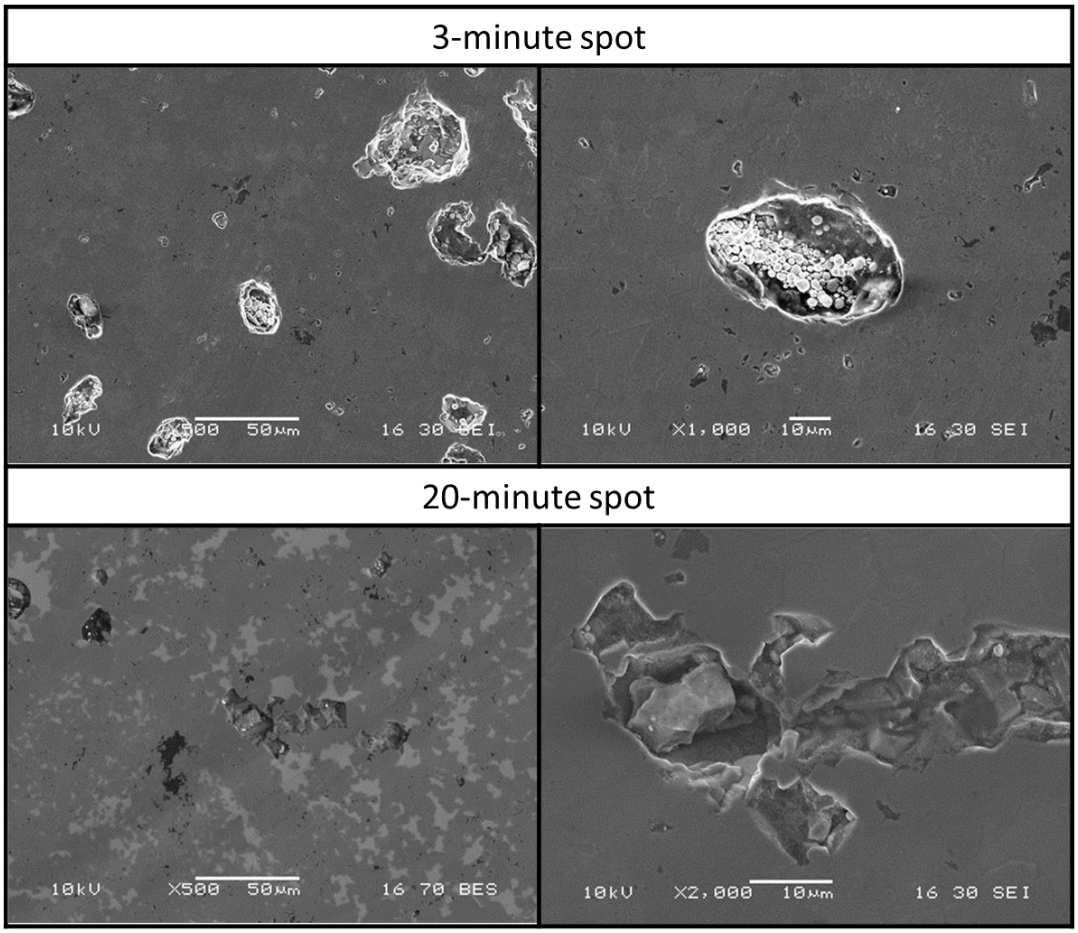

FIGURE 78: SEM images of 3-minute and 20-minute spot

Figure 78 shows that after spotting for 3 minutes, the roughness features were removed. There were small pits, which could be due to exposure of subsurface damage when the top layers of the surface were removed, and there were larger pits due to porosity and silicon grain pullouts during grinding. The height of the 3-minute spot was approximately 2.5 µm. The SEM images after 20 minutes of spotting also showed the presence of big surface fractures which were due to grain pull outs. However, the smaller pits, which was earlier hypothesized that it could be from subsurface damage, we no longer present. But due to the presence of large pits from grain pull outs, the subsurface

damage cannot be studied using roughness parameter values. Further studies with shorter spotting times are required to identify other significant features in the roughness parameters vs spotting time plots. Similar to the test conducted in reaction bonded sample, a full aperture polish of 1µm uniform removal was made on the silicon infiltrated silicon carbide to understand the feasibility of using this grade for final polishing using MRF process. Figure 79 shows the CSI measurements from a 20x objective.

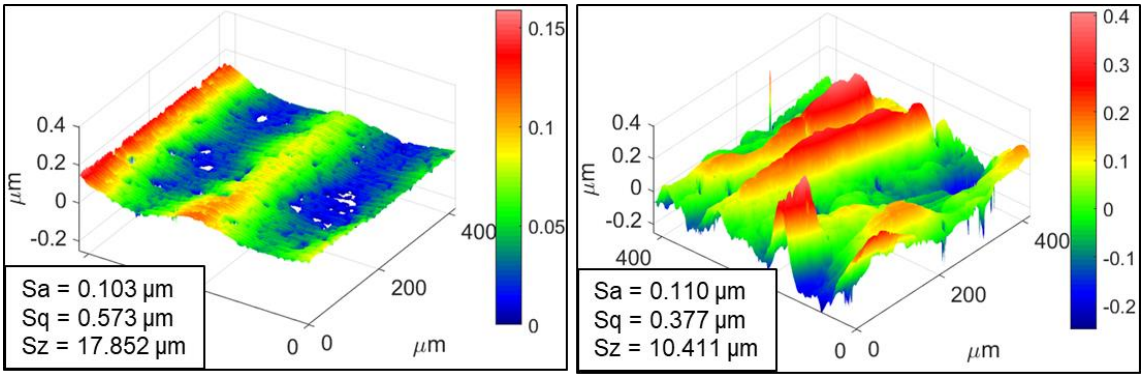

(a) (b)

FIGURE 79: CSI measurements of Si inf grade using 20x objective
(a) Before polishing (b) After polishing

It can be observed from Figure 79 that the mid-spatials caused by the grinding process were removed by the MRF polishing process but additional mid-spatials were introduced on the surface. This was also further analyzed using 2.75x objective to observe the behavior on a larger field of view. CSI measurements using 2.75x objective are as shown in Figure 80.

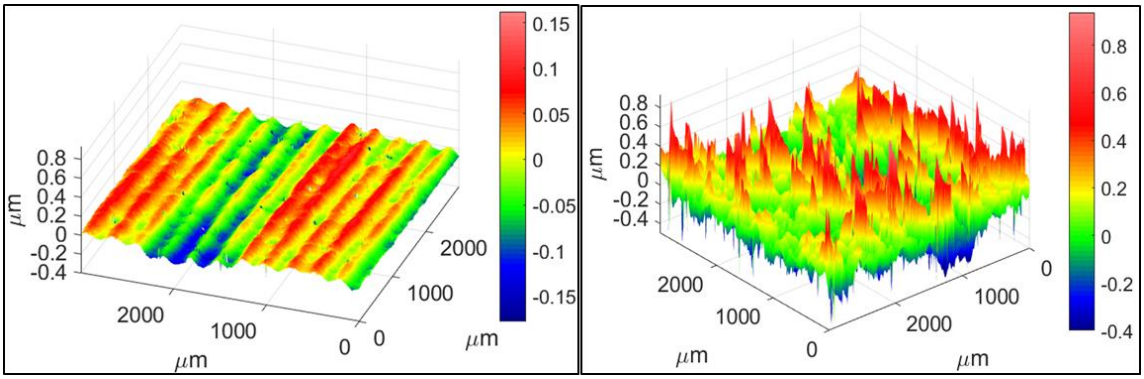

(a) (b)

FIGURE 80: CSI measurements of Si inf grade using 2.75x objective
(a) Before polishing (b) After polishing

The same conclusion can be derived from Figure 80. The mid-spatial introduced from the step over of the grinding process (as shown in Figure 80 (a)) were removed by the MRF polishing process (as shown in Figure 80 (b)). However, it could also be observed that the surface roughness has increased after polishing. It was hypothesized that the increase in surface roughness is due to the different material removal rates between the two phases and also due to interruptions in fluid flow on the surface caused by pits and step features between the two phases. The surface was also observed under the SEM and the images are shown in Figure 81.

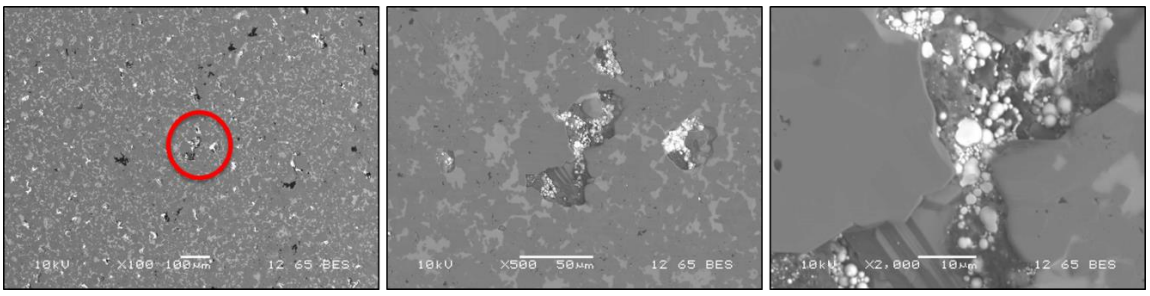

FIGURE 81: SEM images of Si inf grade after polishing

SEM images from Figure 81 revealed that the presence of pits from grain pull outs and porosity enables the carbonyl iron particles to deposit on the surface and thus contaminate the surface. From the above observations based on surface roughness and surface interactions, the current version of MRF polishing and MRF spotting technique may not be suitable for this grade of silicon carbide.

This chapter discussed the results obtained from MRF spotting technique in CVC, CVD, DS, silicon infiltrated and reaction bonded samples that were ground in Makino A55 and Optisonic 1250x. The method was also studied in CVD samples that were ground in two different configurations. The subsurface damage values were reported for CVC and CVD grade samples. The feasibility of this method and the use of MRF polishing in general was also studied for reaction bonded and silicon infiltrated sample.

CHAPTER 6: CONCLUSIONS AND FUTURE WORK

6.1 Summary of surface analysis

This thesis provides a baseline knowledge on diamond grinding different grades of silicon carbide under identical conditions. Wheels of different bond material and diamond grit sizes were used for these tests. The different grades of silicon carbide were subjected to identical conditions in raster configuration and were machined in a Makino A55 and an Optisonic 1250X. Further, a comparative study was also made in CVD grade to study the surface response in two different grinding configurations, raster and spiral. The surface features were studied using SEM and CSI. It was concluded that the nature of surface mechanics was different between different grades even when the grades were ground under identical conditions using same parameters. Single phase material such as direct sintered, CVD and CVC grades showed more uniform material removal characteristics and yielded very low surface roughness values. CVD grade is a pure β-phase face centered cubic (FCC) structure. Owing to its crystal structure and homogeneity, surface level grinding results showed that CVD grade could be ground to achieve a surface roughness between 1 and 2 nm Sq. Through waviness map and PSD plots, the effect of different grinding parameters on the spatial features were studied. CVD sample ground using spiral configuration exhibited a much more complex relation between the spatial features and grinding parameters which requires further study. In all grades that were ground using raster configuration, the surface features exhibited spatial frequencies corresponding to the feed per rev of the tool and step-over. In case of two-phase materials, the nature of surface interaction varied marginally. In silicon infiltrated grade, the surface was dominated by pits from silicon grain pull outs which significantly

affected the surface roughness parameters. In reaction bonded grade, there were visible signatures that the two phases, silicon and silicon carbide, experienced different surface mechanics simultaneously with different material removal rates. In rough and medium ground surfaces, the silicon carbide phase experienced material removal by brittle fracture while silicon phase exhibited ductile deformation. When using finish parameters with resin bonded wheels, both phases exhibited material removal by ductile deformation. However, there was a significant difference between the material removal rates of silicon and silicon carbide phases. Since the hardness of silicon carbide is relatively higher than silicon, the material removal rate at the silicon phase was relatively higher when compared to that of silicon carbide. This resulted in a step-like feature between the silicon and silicon carbide phases throughout the surface. This feature was also observed in silicon infiltrated grade. A summary of the average surface roughness values from grinding using finish parameters as shown in Figure 82 along with associated uncertainties. The tests showed that under identical conditions, CVD and CVC grade produced better surface finish.

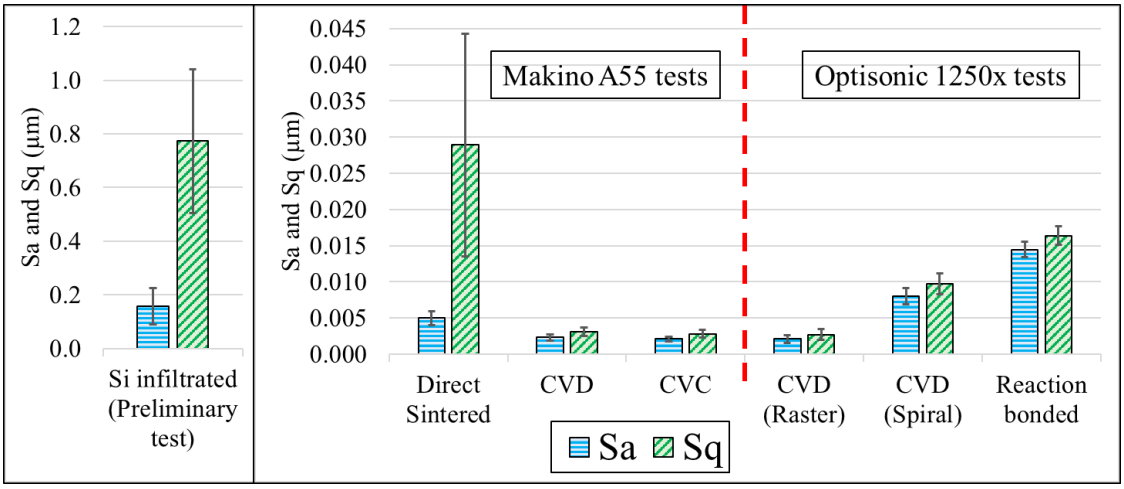

FIGURE 82: Summary of surface roughness on finish ground surface

6.2 Summary of subsurface analysis

The subsurface damage was studied using a recently developed technique which involved producing MRF polish spots with different spotting times to remove the top layer of ground surface and expose the underlying features. The subsurface damage was then characterized based on the evolution of roughness parameters with spotting time at the base of the spots. The theory behind the concept of MRF spotting technique to estimate subsurface damage was verified in CVC grade sample by correlating SEM images with roughness measurements from CSI at the base of spots. Further, the technique was applied to all the ground samples to study the subsurface features and the suitability of this technique to characterize them. It was concluded that the method could estimate subsurface damage height values in homogenous materials such as CVD and CVC. The CVD and CVC samples finish ground on the Makino A55 exhibited a subsurface damage less than 1 µm deep. The CVD grade ground on Optisonic 1250X using raster configuration exhibited a subsurface damage depth of 0.17 µm and CVD

grade finish ground using spiral configuration exhibited subsurface damage of 0.3 µm. The CVD sample ground on the Makino A55 had more subsurface damage than the CVD sample ground on Optisonic 1250X. The CVD sample ground on Makino A55 had a CVD layer of 75 µm. However, due to initial tilt on the sample before grinding, several micrometers of the top CVD layer were ground before using finish parameters. Hence it was hypothesized that the increase in subsurface damage was due to being in the vicinity of the interface between the coating and the substrate.

The presence of porosity and grain pull outs were the major impediments to using this method in grades like direct sintered silicon carbide. This method was also proven to be not successful in two-phase materials such as reaction bonded grade. Due to different phases, the surface experiences different material removal rates at each phase and skews the roughness values in correlation with subsurface damage. Silicon infiltrated, being a two-phase material with a lot of surface pits due to grain pull outs, was also not suitable for this method. The nature of surface interaction during MRF polish in two-phase grades of silicon carbide was further investigated by polishing a whole surface of reaction bonded sample. It was concluded that the differential material removal rates between the silicon and silicon carbide phases increased the surface roughness height parameters while the waviness present on the surface were removed.

Alternatives to studying the spots to characterize subsurface damage were explored to determine subsurface damage depth using qualitative techniques such as SEM since grades like reaction bonded sample could not be characterized using roughness parameters. Preliminary studies were made on the rough ground CVC grade

sample to verify the hypothesis. Figure 83 shows an image of a spot on a rough ground CVC grade silicon carbide along its slope.

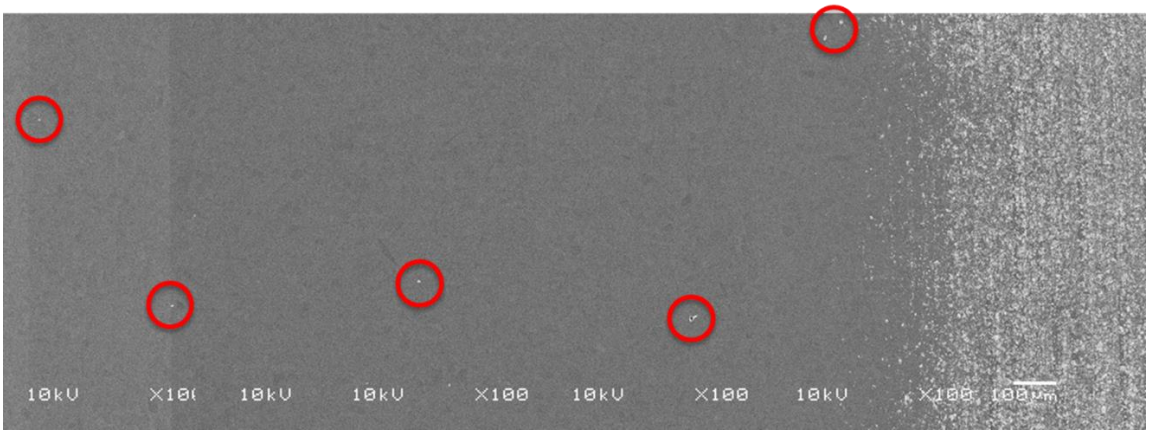

FIGURE 83: SEM image along slope of 6-minute spot (Rough ground CVC sample)

The presence of subsurface damage could be observed along the slope of the spot in Figure 83. Since the spot has a varying slope angle from the top surface to the bottom of the spot, the height of the identified subsurface damages (marked by red circles) could not be determined. Further tests using SEM on flat MRF polished samples are required to characterize the subsurface damage depth. The hypothesis is that observing the evolution of surface features using SEM by iteratively removing the top layers of the surface after each observation would enable characterization of subsurface damage depth. Further MRF polishing are required to first validate the technique in a single-phase grade and then implement it in two-phase materials to estimate the subsurface damage.

In case of using MRF spotting technique to estimate subsurface damage in rough and medium ground samples, the spotting process was removing both the surface roughness as well as subsurface damage from the sample. Due to this reason, samples such as rough ground silicon infiltrated silicon carbide showed a trend of decreasing roughness values,

though it was proved that this technique is not applicable in two-phase materials. The division between removal of surface roughness features and subsurface damage features by polishing is not clear when spotting rough and medium ground surface. A potential study for future work would be to simulate the process of removing surface topographical features and study the evolution of roughness parameters at each stage. This could provide a solution towards understanding the MRF spotting technique better when studying subsurface damage using the technique on rough and medium ground samples.

6.3 First step towards freeform optical surfaces

This thesis focused on surface level interactions and surface/subsurface response from grinding different grades of silicon carbide flat samples. As a first step towards understanding surface response from grinding different geometries, test spheres were ground in three different grades of silicon carbide in SXL500 at Optipro using cup grinding wheels. Figure 84 shows a representation of the setup used for the grinding the test spheres on SXL500.

FIGURE 84: Grinding setup in SXL500 (the part is not silicon carbide in this Figure)

The specifications and the parameters used are tabulated in table 4.

TABLE 4. Grinding Experiment Parameters cup grinding

Grade	Mode of grinding	Grit Size in Mesh	Grit Size in µm	Feed (mm/min)
Si-infiltrated	Rough	35/40	500	0.25
	Finish	600	10-20	0.03
Direct Sintered	Rough	35/40	500	0.15
	Finish	600	10/20	0.03
Reaction bonded	Rough	35/40	500	0.05
	Finish	600	10-20	0.03

The tool spindle speed was at 5000 rpm and the workpiece was rotated at a constant speed of 92 rpm. The objective of this test was to fabricate a concave mirror with a base radius of 247 mm. To fabricate the part with best possible way, the depths were varied per pass for the rough grinding operation. Once the form was achieved, the finish grinding operations were done with a depth of cut of 30 µm and total stock of 70 µm to 100 µm were removed during the finish operation.

The samples were first measured using a Talysurf profilometer to assess the deviation in the radius of base sphere. The measured values of the base radius have been reported in table 5 and Figure 85 shows an image of the ground test sphere samples.

TABLE 5. Grinding Experiment Parameters cup grinding

Grade	Target Base radius (mm)	Measured Base radius (mm)
Si-infiltrated	247	246.98
Direct Sintered	247	247.16
Reaction bonded	247	247.01

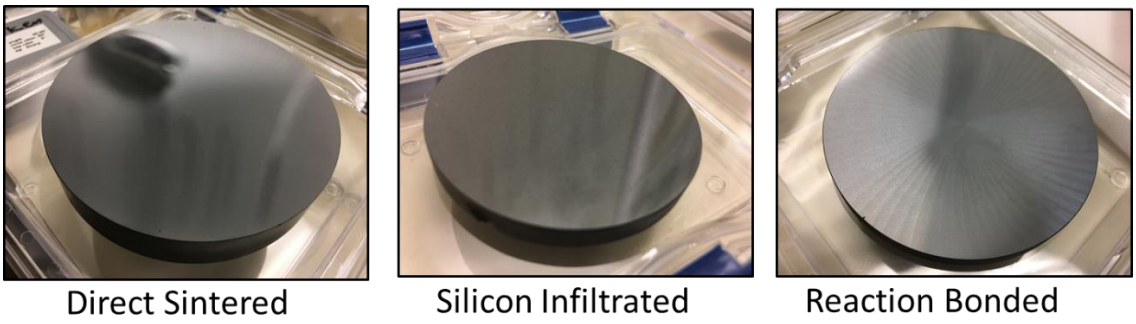

FIGURE 85: Ground Test Spheres

Further, the ground test spheres were studied using CSI and Fizeau interferometer. Since this was a preliminary test, only one surface measurement was taken per grade after finish grinding in the CSI using a 20x Mirau objective. Figure 86 showed CSI images acquired from finish ground surfaces of each grade.

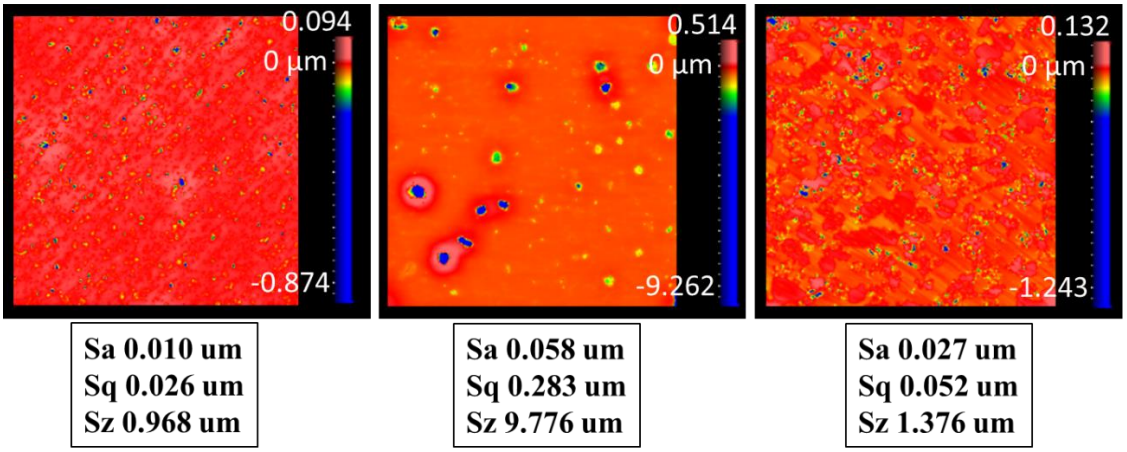

(a) (b) (c)

FIGURE 86: CSI measurement data from test spheres on (a) Direct sintered, (b) Silicon infiltrated and (c) reaction bonded grades of silicon carbide

The CSI images in Figure 86 showed that direct sintered grade had the best surface finish among the three grades. The presence of large pits in silicon infiltrate grade due to silicon grain pull outs was the dominating feature which cause the surface

roughness to go high. In reaction bonded grade, the differential removal rates between silicon and silicon carbide phases, and presence of pits due to microfractures affected the surface finish. However, these experiments were not conducted under similar parametric conditions. Further studies with similar parametric conditions are required to understand the surface response and surface level mechanics in different grades of silicon carbide. Further, measurements were made on a Zygo Verifire Fizeau interferometer as shown in Figure 87

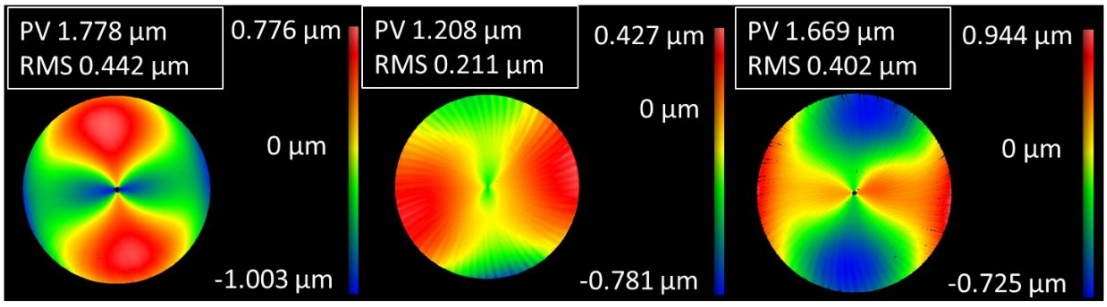

(a) (b) (c)

FIGURE 87: Fizeau measurements from finish ground test spheres
(a) Direct sintered (b) silicon infiltrate (c) Reaction bonded grades

These Fizeau measurement data are presented here after removing the Zernike terms corresponding to piston, X-tilt, Y-tilt and power. These results indicate that the major aberration found on the surface was astigmatism. Further, the Zernike terms generated by the software also showed that the surface was dominated by fourth order spherical aberration. Further grinding tests with different parameters and analysis is required to characterize the form, waviness and surface roughness with respect to the grinding parameters used. This opens potential for future work to study the effect of process parameters on surface form, waviness and surface roughness to characterize surface responses in different geometries. Also, form-based subsurface damage response

is another subject which hasn't been explored yet using MRF spotting technique. An assumption was made when characterizing subsurface damage in flat surfaces in the current study that the damage was uniform across the whole ground surface. This enabled for assessment of subsurface damage by studying the evolution of roughness parameters at the base of spots made at different locations of the ground surface. For surface ground with different geometries, this assumption is no longer valid since the damage changes with form. Hence alternative techniques should be explored to characterize the spots and assess subsurface damage. One possible solution would be full aperture polish the surface and study the evolution of surface topography using SEM.

REFERENCES

[1] K. P. Thompson, E. Schiesser, and J. P. Rolland, “Why are freeform telescopes less alignment sensitive than a traditional unobscured TMA?,” vol. 9633, no. October 2015, pp. 963317-1–5, 2015.

[2] J. Reimers, A. Bauer, K. P. Thompson, and J. P. Rolland, “Freeform spectrometer enabling increased compactness,” *Light Sci. Appl.*, vol. 6, no. 7, p. e17026, 2017.

[3] S. Agarwal and P. V. Rao, “Experimental investigation of surface/subsurface damage formation and material removal mechanisms in SiC grinding,” *Int. J. Mach. Tools Manuf.*, vol. 48, no. 6, pp. 698–710, 2008.

[4] E. Paul, C. J. Evans, A. Mangamelli, M. L. McGlauflin, and R. S. Polvani, “Chemical aspects of tool wear in single point diamond turning,” *Precis. Eng.*, vol. 18, no. 1, pp. 4–19, 1996.

[5] S. Goel, “The current understanding on the diamond machining of silicon carbide,” *J. Phys. D. Appl. Phys.*, vol. 47, no. 24, 2014.

[6] S. Goel, X. Luo, P. Comley, R. L. Reuben, and A. Cox, “Brittle–ductile transition during diamond turning of single crystal silicon carbide,” *Int. J. Mach. Tools Manuf.*, vol. 65, pp. 15–21, Feb. 2013.

[7] S. Takesue, K. Katahira, and J. Komotori, “A study on PCD tool surface reconditioning technique for SiC micromachining,” *Procedia CIRP*, vol. 14, pp. 355–359, 2014.

[8] D. Ravindra, S. Virkar, and J. Patte, “Ductile Mode Micro Laser Assisted Machining of Silicon Carbide,” *Prop. Appl. Silicon Carbide*, 2011.

[9] D. Ravindra and J. Patten, “Micro-Laser-Assisted Machining: The Future of Manufacturing Ceramics and Semiconductors,” *Sensors Mater.*, vol. 26, no. 6, pp. 417–427, 2014.

[10] K. Ding, Y. Fu, H. Su, X. Gong, and K. Wu, “Wear of diamond grinding wheel in ultrasonic vibration-assisted grinding of silicon carbide,” *Int. J. Adv. Manuf. Technol.*, vol. 71, no. 9–12, pp. 1929–1938, 2014.

[11] T. W. Hwang, C. J. Evans, E. P. Whitenton, and S. Malkin, “High Speed Grinding of Silicon Nitride With Electroplated Diamond Wheels, Part 1: Wear and Wheel Life,” *J. Manuf. Sci. Eng.*, vol. 122, no. 1, p. 32, 2000.

[12] W. M. Zeng, Z. C. Li, Z. J. Pei, and C. Treadwell, “Experimental observation of tool wear in rotary ultrasonic machining of advanced ceramics,” *Int. J. Mach.*

Tools Manuf., vol. 45, no. 12–13, pp. 1468–1473, 2005.

[13] I. D. Marinescu, E. Uhlmann, and T. Doi, *Handbook of Ceramics Grinding and Polishing*, 2nd Editio. 2014.

[14] L. Yin, E. Y. J. Vancoille, L. C. Lee, H. Huang, K. Ramesh, and X. D. Liu, "High-quality grinding of polycrystalline silicon carbide spherical surfaces," *Wear*, vol. 256, no. 1–2, pp. 197–207, 2004.

[15] I. D. Marinescu, M. Hitchiner, E. Uhlmann, W. B. Rowe, and I. Inasaki, *Handbook of Machining with Grinding Wheels*. 2007.

[16] W. Yao, Y. Zhang, and J. Han, "Machining characteristics and removal mechanisms of reaction bonded silicon carbide," 2006, vol. 6149, p. 61490W.

[17] W. J. Callister and D. Rethwisch, *Materials science and Engineeing: An Introduction*, 9E ed. 2014.

[18] S. Malkin and T. W. Hwang, "Grinding Mechanisms for Ceramics," *CIRP Ann. - Manuf. Technol.*, vol. 45, no. 2, pp. 569–580, Jan. 1996.

[19] D. A. Lucca, E. Brinksmeier, and G. Goch, "Progress in assessing surface and subsurface integrity," *CIRP Ann. - Manuf. Technol.*, vol. 47, no. 2, pp. 669–693, 1998.

[20] T. G. Bifano, T. A. Dow, and R. O. Scattergood, "Ductile-Regime Grinding: A New Technology for Machining Brittle Materials," *J. Eng. Ind.*, vol. 113, no. 2, p. 184, 1991.

[21] H. P. KIRCHNER, "Comparison of Single-Point and Multipoint Grinding Damage in Glass," *J. Am. Ceram. Soc.*, vol. 67, no. 5, pp. 347–353, May 1984.

[22] B. Zhang and T. D. Howes, "Material-Removal Mechanisms in Grinding Ceramics," *CIRP Ann. - Manuf. Technol.*, vol. 43, no. 1, pp. 305–308, 1994.

[23] S. Agarwal and P. Venkateswara Rao, "Grinding characteristics, material removal and damage formation mechanisms in high removal rate grinding of silicon carbide," *Int. J. Mach. Tools Manuf.*, vol. 50, no. 12, pp. 1077–1087, 2010.

[24] S. Agarwal, "Optimizing machining parameters to combine high productivity with high surface integrity in grinding silicon carbide ceramics," *Ceram. Int.*, vol. 42, no. 5, pp. 6244–6262, 2015.

[25] S. Agarwal and P. Venkateswara Rao, "Modeling and prediction of surface roughness in ceramic grinding," *Int. J. Mach. Tools Manuf.*, vol. 50, no. 12, pp. 1065–1076, 2010.

[26] S. Agarwal, S. K. Khare, V. P. Pandey, and M. Patel, “An Analytical Chip Thickness Model for Performance Assessment in Silicon Carbide Grinding,” *Procedia Manuf.*, vol. 10, pp. 298–306, 2017.

[27] Y. Zhou, P. D. Funkenbusch, D. J. Quesnel, D. Golini, and A. Lindquist, “Effect of Etching and Imaging Mode on the Measurement of Subsurface Damage in Microground Optical Glasses,” *J. Am. Ceram. Soc.*, vol. 77, no. 12, pp. 3277–3280, Dec. 1994.

[28] H. H. K. Xu and S. Jahanmir, “Simple Technique for Observing Subsurface Damage in Machining of Ceramics,” *J. Am. Ceram. Soc.*, vol. 77, no. 5, pp. 1388–1390, May 1994.

[29] B. Zhang and T. D. Howes, “Subsurface Evaluation of Ground Ceramics,” *CIRP Ann. - Manuf. Technol.*, vol. 44, no. 1, pp. 263–266, 1995.

[30] J. C. Lambropoulos, Y. Li, P. Funkenbusch, and J. Ruckman, “Non-contact estimate of grinding-induced subsurface damage,” *Proc. SPIE*, vol. 3782, no. July, pp. 41–50, 1999.

[31] S. N. Shafrir, J. C. Lambropoulos, and S. D. Jacobs, “MRF spotting technique for studying subsurface damage in deterministic microground polycrystalline alumina,” in *Applied Optics*, 2007, vol. 46, no. 22, p. 66710J.

[32] S. N. Shafrir, J. C. Lambropoulos, and S. D. Jacobs, “Subsurface damage and microstructure development in precision microground hard ceramics using magnetorheological finishing spots,” *Appl. Opt.*, vol. 46, no. 22, p. 5500, Aug. 2007.

[33] F. Träger, *Springer Handbook of Lasers and Optics*. New York, NY: Springer New York, 2007.

[34] J. Casstevens, D. J. Bray, A. Rashed, and R. Plummer, “Rapid fabrication of large mirror substrates by conversion joining of silicon carbide,” in *SPIE*, 2005, vol. 5868, no. August 2005, p. 586801.

[35] A. Ellison, J. Zhang, A. Henry, and E. Janzén, “Epitaxial growth of SiC in a chimney CVD reactor,” *J. Cryst. Growth*, vol. 236, no. 1–3, pp. 225–238, 2002.

[36] G. Chollon, F. Langlais, M. Placide, and P. Weisbecker, “Transient stages during the chemical vapour deposition of silicon carbide from CH3SiCl3/H2: impact on the physicochemical and interfacial properties of the coatings,” *Thin Solid Films*, vol. 520, no. 19, pp. 6075–6087, Jul. 2012.

[37] J. S. Goela and M. A. Pickering, “Optics applications of chemical vapor deposited beta-SiC,” vol. 1028908, no. July 1997, p. 1028908, 1997.

[38] J. S. Johnson, K. D. Grobsky, and D. Bray, “Rapid fabrication of lightweight silicon carbide mirrors,” *Optomech. Des. Eng.*, vol. 4771, pp. 243–253, 2002.

[39] C. T. Tanaka and K. Webb, “Chemical vapor composite silicon carbide for space telescopes,” *Proc.of SPIE*, vol. 6265, no. June 2006, p. 62652Q1-9, 2006.

[40] D. Aikens, J. E. DeGroote, and R. N. Youngworth, “Specification and Control of Mid-Spatial Frequency Wavefront Errors in Optical Systems,” p. OTuA1, 2013.

[41] M. Field, J. F. Kahles, and J. T. Cammett, “A Review of Measuring Methods for Surface Integrity,” in *CIRP Annals - Keynote Paper S*, 1972, pp. 219–238.

[42] S. Malkin and C. Guo, *Grinding Technology: Theory and Application of Machining with Abrasives*. Industrial Press, 2008.

[43] E. Brinksmeier, C. Heinzel, and M. Wittmann, “Friction, cooling and lubrication in grinding,” *CIRP Ann. - Manuf. Technol.*, vol. 48, no. 2, pp. 581–598, 1999.

[44] R. A. Irani, R. J. Bauer, and A. Warkentin, “A review of cutting fluid application in the grinding process,” *Int. J. Mach. Tools Manuf.*, vol. 45, no. 15, pp. 1696–1705, 2005.

[45] P. Dumas, “Magnetorheological finishing (optics).” McGraw-Hill Education OP - AccessScience, 2005.

[46] S. N. Shafrir *et al.*, “Zirconia-coated carbonyl-iron-particle-based magnetorheological fluid for polishing optical glasses and ceramics,” *Appl. Opt.*, vol. 48, no. 35, p. 6797, 2009.

[47] H. Shahinian (Editor), “ReadMetroProFile.” 2018.

[48] J. D. Errico, “inpaint_nans,” *Matlab Cent. Exch. File*, no. Last Updated August 2012, 2004.

[49] International Standard, “ISO 16610-21-2012 - Geometrical Product Specifications - Filtration - Part 21: Linear profile filters: Gaussian Filters.”

[50] International Standard, “ISO 25178-3-2012 - Geometrical Product Specifications - Surface texture: Areal - Part 3: Specification operators.”

[51] B. Muralikrishnan and J. Raja, *Computational Surface and Roundness Metrology*. London: Springer London, 2009.

[52] International Standard, “ISO 25178-604-2013 - Geometrical Product Specifications - Surface texture: Areal - Part 604: Nominal characteristics of non-contact (coherence scanning interferometry) instruments.”

[53] International Standard, “ISO 25178-2-2012 - Geomtrical Prodcut Specifications - Surface Texture: Areal - Part 2: Terms, definitions and surface texture parameters.”

[54] International Standard, “ISO 4288-1996 - Geometrical Product Specifications - Surface Texture: Profile Method - Rules and procedures for the assessment of surface finish.”

APPENDIX A: MATLAB CODE

MATLAB® was used to process CSI data acquired using 20x objective and apply filters to analyze roughness and waviness heightmaps. The program also calculates the roughness parameters and exports the data to a spreadsheet for further analysis. The list of Main program and subprograms used are listed in table A.1.

TABLE A.1. List of MATLAB® programs and subprograms

Program Name	Purpose
SWLI_Data_Main.m	Main Program to process CSI data
swli_to_mat.m	Imports CSI measurements (.dat file) to MATLAB (Subprogram)
fixplot.m	Removes NaNs and replaces them with interpolated values (Subprogram)
test.m	Subprogram to process raw data
createFit.m	Subprogram to remove form
gauss_remove.m	Subprogram to define and use a Gaussian filter
savegraph3.m	Subprogram to create plots and save as pdf files
export_parameters_2_excel.m	Subprogram to export roughness parameters to a spreadsheet

A.1 SWLI_Data_Main.m

```
% Main program to process CSI data
clear all
clc
close all

% Loading height map data from .dat files
addpath(genpath('Inpaint_nans'));
dataswli = swli_to_mat;

% Removing nans by interpolation
prog1 = waitbar(0,'Identifying Nans...');
set(get(findobj(prog1,'type','axes'),'title'), 'string',
'Processing Nans');
steps = length(dataswli);
```

```
for i = 1:length(dataswli)
    waitbar(i/steps);
    dataswli(i).phasedata = fixplot(dataswli(i).phasedata);
end

delete(prog1);
clearvars prog1;

% Saving workspace to a .mat file
save('Swli_data.mat');

% Data Processing
 test(dataswli);

 clear all;
 close all;

% Exporting roughness parameters to a spreadsheet
 export_parameters_2_excel();
 arrange_results_folder_1();

 message1 = msgbox('Program Execution
Completed','Success');

% End of Main Program
```

A.2 swli_to_mat.m

```
% Function to import .dat file
function dataswli= swli_to_mat

files = dir('*.dat');

for i = 1:1:length(files)
    [~,dataswli(i).name,~] = fileparts(files(i).name);
    [~,~,~,temp] = ReadMetroProFile(files(i).name);
    dataswli(i).phasedata = temp;

end
end
```

A.3 fixplot.m

```
%Function to remove NaNs and replace with interpolated
values
```

```
function dataswli = fixplot(dataswli)
dataswli = inpaint_nans(dataswli);
end
```

A.4 test.m

```
% Function to process CSI data

function test(dataswli)

clc
clearvars -except dataswli;

prog1 = waitbar(0,'Processing data...');
pause(1);

%Loading CSI data incase of previously saved data
%load('Swli_data.mat');
mkdir('Results');


for file = 1 : length(dataswli)

%% Progress bar
step = file;
steps = length(dataswli);

%% Input objective magnification and zoom options
obj = 20;
zoomx = 1;
%Slice Row number for X direction slice
row = 512;
%Slice Column number for Y direction slice
column = 512;

%Defining Field of View
[y_limit , x_limit] = size(dataswli(file).phasedata);
range = 0;
if obj == 5
    range = 1670;
else if obj == 2.75
        range = 2995.230;
    else if obj ==20
        range = 418.065;
```

```
        else if obj == 50
            range = 167.758;
            else
           disp('Objective information not available');
           return;
            end
        end
    end
end
range = range*zoomx;
x = (linspace(0,range,y_limit))';
y = (linspace(0,range,x_limit))';

%Converting data to micrometer scale
z = (dataswli(file).phasedata)*10^6;

%Function to remove form
[X , Y] = meshgrid(x,y);
[fitresult, gof] = createFit(X, Y, z);
zp = fitresult(X,Y);

z = z - zp;

%Gaussian filter (Low Pass filter to get waviness data)
dataswli(file).w = zeros(length(x),length(y));
dataswli(file).w = gauss_remove(x,y,z,range);

%Roughness data
dataswli(file).z = z - dataswli(file).w;

%Calculating surface parameters:
parameters(file).name = dataswli(file).name;
parameters(file).Sa = mean(mean(abs(dataswli(file).z))) ;
parameters(file).Sq = sqrt(mean(dataswli(file).z(:).^2));
parameters(file).Sz = max(max(dataswli(file).z)) -
min(min(dataswli(file).z));
parameters(file).Wa = mean(mean(abs(dataswli(file).w))) ;
parameters(file).Wq = sqrt(mean(dataswli(file).w(:).^2));
parameters(file).Wz = max(max(dataswli(file).w)) -
min(min(dataswli(file).w));

%X direction slice
 x_slice = dataswli(file).z(row,:);

%Y direction slice
 y_slice = dataswli(file).z(:,column);
```

```
%Calculate Slice parameters
parameters(file).Rax = mean(abs(x_slice));
parameters(file).Rqx = sqrt(mean(x_slice.^2));
parameters(file).Rzx = max(x_slice) - min(x_slice);
parameters(file).Ray = mean(abs(y_slice));
parameters(file).Rqy = sqrt(mean(y_slice.^2));
parameters(file).Rzy = max(y_slice) - min(y_slice);

%Generating plots and saving as pdf
savegraph3(dataswli,parameters,file,x,y,x_slice,y_slice);
message1 = sprintf('Files processed... %d/%d',step,steps);
set(get(findobj(prog1,'type','axes'),'title'), 'string',
message1);
waitbar(step/steps);
end
delete(prog1);

%Saving Parameters
save('parameters.mat');
end
%End of function
```

A.5 createFit.m

```
%Function to remove form

function [fitresult, gof] = createFit(x, y, z)

[xData, yData, zData] = prepareSurfaceData( x, y, z );

%Type of form defined by polynomial order
ft = 'poly11'; %Used for ground samples only
%ft = 'poly44'; %Used for spot surfaces only

%Fitting a model to the surface using defined polynomial
[fitresult, gof] = fit([xData,yData],zData,ft,'Normalize',
'on');
end
```

A.6 gauss_remove.m

```
%Defining gaussian function for surface filter

function [w] = gauss_remove(xr,yr,z,range)
```

```
nx = length(xr); %Length of x
ny = length(yr); %Length of y

dx = range/(nx); %Pixel size in x
dy = range/(ny); %Pixel size in y


a=sqrt(log(2)/pi); %Constant for Gaussian
lambda_cutoff = 80 ; %Cutoff wavelength for the filter

x = (-lambda_cutoff:dx:lambda_cutoff )';
y = (-lambda_cutoff:dy:lambda_cutoff )';
mx = size(x,1);
my = size(y,1);

%Gaussian function
for i = 1: mx
    for j = 1:my
S(j,i) = (1/(a^2*lambda_cutoff*lambda_cutoff))*exp(-
pi*(x(i)/a/lambda_cutoff)^2 -pi*(y(j)/a/lambda_cutoff)^2);
    end
end

%Normalization
S = S/sum(sum(S));

%Convolution
C = conv2(z,S);

%Cutting off surface to generate waviness profile
w = C(my/2+1:ny+my/2,mx/2+1:nx+mx/2);
end
%End of sub function
```

A.7 savegraph3.m

```
%This function creates waviness, roughness map and 2d
%profile plots of roughness map and saves it as a pdf

function
savegraph3(dataswli,parameters,file,x,y,x_slice,y_slice)


%Figure window
fig_file = figure('visible','off');
clf;
```

```
%Waviness height map
subplot(321)
surf(x,y,dataswli(file).w,'linestyle','none')
view(0,90)
axis tight
axis equal
h = colorbar;
title(h,'\mum');
colormap jet;
title('Waviness height map');
xlabel('\mum');
ylabel('\mum');
grid on;

%Roughness height map
subplot(322)
surf(x,y,dataswli(file).z,'linestyle','none')
view(0,90)
axis tight
axis equal
h1 = colorbar;
title(h1,'\mum');
colormap jet;
title('Roughness height map');
xlabel('\mum');
ylabel('\mum');
grid on;
h = legend(sprintf('Sa = %.4f um\nSq = %.4f um\nSz = %.4f
um',parameters(file).Sa,parameters(file).Sq,parameters(file
).Sz));
hold on

%X direction 2D profile plot
subplot(3,2,[3 4])
plot(x,x_slice);
title('X Roughness profile');
xlabel('X position in \mum');
ylabel('Height in \mum');
axis tight;
h1 = legend(sprintf('Ra = %.4f um\nRq = %.4f um\nRz = %.4f
um',parameters(file).Rax,parameters(file).Rqx,parameters(fi
le).Rzx),'location','northeastoutside');
grid on;

hpos = get(h,'position');
h1pos = get(h1,'position');
```

```
set(h1,'location','southeastoutside');
set(h,'position',[0.03+h1pos(1) 0.05+h1pos(2) hpos(3)
hpos(4)]);

%Y direction 2D profile plot
subplot(3,2,[5 6])
plot(y,y_slice);
title('Y Roughness profile');
xlabel('X position in \mum');
ylabel('Height in \mum');
axis tight;
legend(sprintf('Ra = %.4f um\nRq = %.4f um\nRz = %.4f
um',parameters(file).Ray,parameters(file).Rqy,parameters(fi
le).Rzy),'location','northeastoutside');
grid on;

%Saving pdf files in a folder called Results
cd Results
print(fig_file,sprintf('%s',parameters(file).name),'-
dpdf','-fillpage');
cd ..
end
%End of sub program
```

A.8 export_parameters_2_excel.m

```
%Exporting the parameters to a spreadsheet

function export_parameters_2_excel

load('parameters','parameters');

prog1 = waitbar(0,'Exporting Parameters to Excel');
steps = (length(parameters));


names = fieldnames(parameters);

para_excel = names';


for i = 1:length(parameters)
        step = i;
        temp = parameters(1,i);
        temp1 = struct2cell(temp);
        para_excel(i+1,:) = temp1;
        waitbar(step/steps);
```

```
end

xlswrite('Processed_Roughness_parameters',para_excel,'Proce
ssed_raw_data');

delete(prog1);
clearvars prog1;

end

%End of functions
```

APPENDIX B: MATLAB CODE READMETROPRO

This part of MATLAB® code converts the data from .dat files acquired from CSI measurements to variables of different types that can be accessed in MATLAB. This code was edited by and borrowed from Dr. Hossein Shahinian.

B.1 ReadMetroProFile.m

```
function [lError,
InfoHeader,IntensityMap,PhaseMap]=ReadMetroProFile(filename
)
warning off all
lError=-1;
InfoHeader=0;
IntensityMap=0;
PhaseMap=0;
    fid = fopen(filename,'r', 'b');
    try
        message = ferror(fid);
    catch
        emessage=strcat('File doesn''''t exist or there is
an access violation to file : ',filename);
        errordlg(emessage,'File Type Error','modal')
        lError=-1;
        return;
    end
    InfoHeader.MagicNumber=fread(fid,1,'*int32');
    if InfoHeader.MagicNumber~=-2011495569 &&
InfoHeader.MagicNumber~=-2011495568 &&
InfoHeader.MagicNumber~=-2011495567
        lError=fclose(fid);
        lError=-1;
        return;
    end

    InfoHeader.HeaderFormat=fread(fid,1,'*int16');
    if InfoHeader.HeaderFormat~=1 &&
InfoHeader.HeaderFormat~=2 && InfoHeader.HeaderFormat~=3
        lError=fclose(fid);
        lError=-1;
        return;
    end
    InfoHeader.HeaderSize=fread(fid,1,'*int32');
```

```
    if InfoHeader.HeaderSize~=834 &&
InfoHeader.HeaderSize~=4096
        lError=fclose(fid);
        lError=-1;
        return;
    end
    InfoHeader.SoftwareType=fread(fid,1,'*int16');
    InfoHeader.SoftwareDate=fread(fid,30,'uchar=>char')';
    InfoHeader.MajorVersion=fread(fid,1,'*int16');
    InfoHeader.MinorVersion=fread(fid,1,'*int16');
    InfoHeader.BugVersion=fread(fid,1,'*int16');
    InfoHeader.IntensOriginX=fread(fid,1,'*int16');
    InfoHeader.IntensOriginY=fread(fid,1,'*int16');
    InfoHeader.IntensWidth=fread(fid,1,'*int16');
    InfoHeader.IntensHeight=fread(fid,1,'*int16');
    InfoHeader.NBuckets=fread(fid,1,'*int16');
    InfoHeader.IntensRange=fread(fid,1,'*uint16');
    InfoHeader.NrOfBytesIntens=fread(fid,1,'*int32');
%Phase
    InfoHeader.PhaseOriginX=fread(fid,1,'*int16');
    InfoHeader.PhaseOriginY=fread(fid,1,'*int16');
    InfoHeader.PhaseWidth=fread(fid,1,'*int16');
    InfoHeader.PhaseHeight=fread(fid,1,'*int16');
    InfoHeader.NrOfBytesPhase=fread(fid,1,'*int32');
%timestamp
    InfoHeader.TimeStamp=fread(fid,1,'*int32');
    InfoHeader.Comment=fread(fid,82,'uchar=>char')';
    InfoHeader.Source=fread(fid,1,'*int16');
    InfoHeader.IntfScaleFactor=fread(fid,1,'*float32');
    InfoHeader.WaveLengthIn=fread(fid,1,'*float32');
    InfoHeader.NumericAperture=fread(fid,1,'*float32');
    InfoHeader.ObliquityFactor=fread(fid,1,'*float32');
    InfoHeader.Magnification=fread(fid,1,'*float32');
    InfoHeader.CameraRes=fread(fid,1,'*float32');
    InfoHeader.AcquireMode=fread(fid,1,'*int16');
    InfoHeader.IntensAvgs=fread(fid,1,'*int16');
    InfoHeader.PZTCal=fread(fid,1,'*int16');
    InfoHeader.PZTGainTolerance=fread(fid,1,'*int16');
    InfoHeader.PZTGain=fread(fid,1,'*int16');
    InfoHeader.PartThickness=fread(fid,1,'*float32');
    InfoHeader.AGC=fread(fid,1,'*int16');
    InfoHeader.TargetRange=fread(fid,1,'*float32');
    InfoHeader.Spare1=fread(fid,1,'*int16');
    InfoHeader.MinMod=fread(fid,1,'*int32');
    InfoHeader.MinModPts=fread(fid,1,'*int32');
    InfoHeader.PhaseRes=fread(fid,1,'*int16');
    InfoHeader.MinimumAreaSize=fread(fid,1,'*int32');
```

```
    InfoHeader.DisconAction=fread(fid,1,'*int16');
    InfoHeader.DisconFilter=fread(fid,1,'*float32');
    InfoHeader.ConnectionOrder=fread(fid,1,'*int16');
    InfoHeader.DataSign=fread(fid,1,'*int16');
    InfoHeader.CameraWidth=fread(fid,1,'*int16');
    InfoHeader.CameraHeight=fread(fid,1,'*int16');
    InfoHeader.SystemType=fread(fid,1,'*int16');
    InfoHeader.SystemBoard=fread(fid,1,'*int16');
    % I guess Serial Number of Instrument not to be
    % negative so *uint16 instead of *int16
    InfoHeader.SystemSerial=fread(fid,1,'*uint16');
    InfoHeader.InstrumentId=fread(fid,1,'*int16');
    InfoHeader.ObjectiveName=fread(fid,12,'uchar=>char')';
    InfoHeader.PartNum=fread(fid,40,'uchar=>char')';
    InfoHeader.CodeVType=fread(fid,1,'*int16');
    InfoHeader.PhaseAvgs=fread(fid,1,'*int16');
    InfoHeader.SubtractSysErr=fread(fid,1,'*int16');
    InfoHeader.Spare2=fread(fid,16,'uchar=>char')';
    InfoHeader.PartSerNum=fread(fid,40,'uchar=>char')';
    InfoHeader.RefractiveIndex=fread(fid,1,'*float32');
    InfoHeader.RemoveTiltBias=fread(fid,1,'*int16');
    InfoHeader.RemoveFringes=fread(fid,1,'*int16');
    InfoHeader.MaxAreaSize=fread(fid,1,'*int32');
    InfoHeader.SetupType=fread(fid,1,'*int16');
    InfoHeader.Spare3=fread(fid,2,'uchar=>char')';
    InfoHeader.PreConnectFilter=fread(fid,1,'*float32');
    InfoHeader.Wavelength2=fread(fid,1,'*float32');
    InfoHeader.WavelengthFold=fread(fid,1,'*int16');
    InfoHeader.Wavelength1=fread(fid,1,'*float32');
    InfoHeader.Wavelength3=fread(fid,1,'*float32');
    InfoHeader.Wavelength4=fread(fid,1,'*float32');
InfoHeader.WavelengthSelect=fread(fid,8,'uchar=>char')';
    InfoHeader.FdaRes=fread(fid,1,'*int16');
InfoHeader.ScanDescription=fread(fid,20,'uchar=>char')';
    InfoHeader.NFiducials=fread(fid,1,'*int16');
    InfoHeader.Fiducial1X=fread(fid,1,'*float32');
    InfoHeader.Fiducial1Y=fread(fid,1,'*float32');
    InfoHeader.Fiducial2X=fread(fid,1,'*float32');
    InfoHeader.Fiducial2Y=fread(fid,1,'*float32');
    InfoHeader.Fiducial3X=fread(fid,1,'*float32');
    InfoHeader.Fiducial3Y=fread(fid,1,'*float32');
    InfoHeader.Fiducial4X=fread(fid,1,'*float32');
    InfoHeader.Fiducial4Y=fread(fid,1,'*float32');
    InfoHeader.Fiducial5X=fread(fid,1,'*float32');
    InfoHeader.Fiducial5Y=fread(fid,1,'*float32');
    InfoHeader.Fiducial6X=fread(fid,1,'*float32');
    InfoHeader.Fiducial6Y=fread(fid,1,'*float32');
```

```
    InfoHeader.Fiducial7X=fread(fid,1,'*float32');
    InfoHeader.Fiducial7Y=fread(fid,1,'*float32');
    InfoHeader.PixelWidth=fread(fid,1,'*float32');
    InfoHeader.PixelHeight=fread(fid,1,'*float32');
    InfoHeader.ExitPupilDiam=fread(fid,1,'*float32');
    InfoHeader.LightLevelPct=fread(fid,1,'*float32');
    InfoHeader.CoordsState=fread(fid,1,'*int32');
    InfoHeader.XPos=fread(fid,1,'*float32');
    InfoHeader.YPos=fread(fid,1,'*float32');
    InfoHeader.ZPos=fread(fid,1,'*float32');
    InfoHeader.XRot=fread(fid,1,'*float32');
    InfoHeader.YRot=fread(fid,1,'*float32');
    InfoHeader.ZRot=fread(fid,1,'*float32');
    InfoHeader.CoherenceMode=fread(fid,1,'*int16');
    InfoHeader.SurfaceFilter=fread(fid,1,'*int16');
    InfoHeader.SysErrFile=fread(fid,28,'uchar=>char')';
    InfoHeader.ZoomDescr=fread(fid,8,'uchar=>char')';
    InfoHeader.Spare4=fread(fid,264,'uchar=>char')';
% jumping to Intensity Map
    fseek(fid,double(InfoHeader.HeaderSize),'bof');
    if (InfoHeader.NBuckets>1)
IntensityMap=zeros(double(InfoHeader.NBuckets),double(InfoH
eader.IntensHeight),double(InfoHeader.IntensWidth),'uint16'
);
        for n=1:InfoHeader.NBuckets
       IntensTemp=fread(fid,[double(InfoHeader.IntensWidth)
double(InfoHeader.IntensHeight)],'*uint16');
            IntensTemp=IntensTemp';
            IntensTemp(IntensTemp >= 65535)=NaN;
            IntensityMap(n,:,:)=IntensTemp;
        end
    else
     IntensityMap=fread(fid,[double(InfoHeader.IntensWidth)
double(InfoHeader.IntensHeight)],'*uint16');
        IntensityMap=IntensityMap';
        IntensityMap(IntensityMap >= 65535)=NaN;
    end
    if isempty(IntensityMap)
        IntensityMap=0;
    end
% jumping to Phase Map
fseek(fid,double(InfoHeader.HeaderSize)+double(InfoHeader.I
ntensWidth)*double(InfoHeader.IntensHeight)*double(InfoHead
er.NBuckets)*2,'bof');

PhaseMap=zeros(double(InfoHeader.IntensHeight),double(InfoH
eader.IntensWidth));
```

```
    PhaseMap(:)=NaN;
PhaseMapTemp=double(fread(fid,[double(InfoHeader.PhaseWidth
) double(InfoHeader.PhaseHeight)],'*int32'));
    PhaseMapTemp=PhaseMapTemp';
    PhaseMapTemp(PhaseMapTemp >= 2147483640)=NaN;
    if (InfoHeader.IntensHeight==0 &&
InfoHeader.IntensWidth==0)
        PhaseMap=PhaseMapTemp;
    else
PhaseMap(double(InfoHeader.PhaseOriginY)+1:double(InfoHeade
r.PhaseOriginY)+double(InfoHeader.PhaseHeight),double(InfoH
eader.PhaseOriginX)+1:double(InfoHeader.PhaseOriginX)+doubl
e(InfoHeader.PhaseWidth))=PhaseMapTemp;
    end
    switch InfoHeader.PhaseRes
        case 0
            R=4096;
        case 1
            R=32768;
        case 2
            R=131072;
        otherwise
            R=32768;
    end
PhaseMap=PhaseMap.*double(InfoHeader.IntfScaleFactor).*doub
le(InfoHeader.ObliquityFactor).*double(InfoHeader.WaveLengt
hIn)./R;
    if isempty(PhaseMap)
        PhaseMap=0;
    end

    lError = fclose(fid);
return;

% End of function
```

APPENDIX C: SURFACE TOPOGRAPHY REPEATABILITY TEST

The following MATLAB® code imports data of type .datx from CSI Nexview's software Zygo Mx and evaluates the surface topography repeatability.

C.1 STR_Main_code

```
%% Main code
%% Code for Opening MX .DATx file and removing form
clear all
clc
close all

%% Loading data from .dat files
addpath(genpath('DATx_Files'));

% Extracting data
files = dir('DATx_Files\*.datx');

for i = 1:1:length(files)

      pname = files(i).folder;
      fname = files(i).name;
      dataswli(i).name = fname(1:end-5);
      [xs,ys,surfaceData] = importDatx_series(pname,fname);
      dataswli(i).phasedata = surfaceData;
      dataswli(i).xs = xs*10^6;
      dataswli(i).ys = ys*10^6;
end

%% Defining field of view
for file = 1 : length(dataswli)
x = dataswli(file).xs;
y = dataswli(file).ys;

%% Conversion to um
z = (dataswli(file).phasedata)*10^6;

%% Form removal by plane fitting

[fitresult, gof] = createFit_2(x, y, z);
zp = fitresult(x,y);

dataswli(file).zform = z - zp;
```

```
z = dataswli(file).zform;

%lateral.x = x;
%lateral.y = y;

heightmap(file).data = z;

% Evaluation of roughness parameters
parameters(file).Sa = mean(nanmean(abs(z)));
parameters(file).Sq = sqrt(nanmean(z(:).^2));
parameters(file).Sz = max(max(z)) - min(min(z));

end

%% Estimation of surface topography repeatability
clc;
[STR_Sa, STR_Sq, STR_Sz] = STR_error(heightmap);

%% Result
fprintf('\n\nSurface Topography Repeatability for %d
measurements \n\n ',length(files));
fprintf('STR_Sa = %f \nSTR_Sq = %f \nSTR_Sz = %f
\n\n',STR_Sa,STR_Sq,STR_Sz)

%% End of main code
```

C.2 importDatx_series.m

```
function [xs,ys,surfaceData] =
importDatx_series(pname,fname)

cd DATx_Files;

if isequal(fname,0)
    return
end

filename = [pname '\' fname];

surfaceData = [];
intensityData = [];
colorData=[];
qualityData=[];

info = h5info(filename);
```

```
try
    surfaceData =
rot90(h5read(filename,'/Measurement/Surface'));
    surfNanVal =
h5readatt(filename,'/Measurement/Surface','No Data');
    xConverter =
h5readatt(filename,'/Measurement/Surface','X Converter');
    yConverter =
h5readatt(filename,'/Measurement/Surface','Y Converter');
    zConverter =
h5readatt(filename,'/Measurement/Surface','Z Converter');

    surfaceData(surfaceData >= surfNanVal)=NaN;

    switch zConverter.BaseUnit{:}
        case 'NanoMeters'
            zScale = 1e-9;
        case 'MicroMeters'
            zScale = 1e-6;
    end

    surfaceData = surfaceData * zScale;

    xRes = xConverter.Parameters{:}(2);
    yRes = yConverter.Parameters{:}(2);

    [sizeY,sizeX]=size(surfaceData);
    x=(0:sizeX-1)*xRes;
    y=(0:sizeY-1)*yRes;
    [ys,xs]=ndgrid(y,x);
catch
    disp('No surface data')
    return
end

try
    intensityData =
rot90(h5read(filename,'/Measurement/Intensity'));
    intensNanVal =
h5readatt(filename,'/Measurement/Intensity','No Data');
    intensityData(intensityData >= intensNanVal)=NaN;
catch
end

try
    qualityData =
rot90(h5read(filename,'/Measurement/Quality'));
```

```
    qualNanVal =
h5readatt(filename,'/Measurement/Quality','No Data');
    qualityData(qualityData >= qualNanVal)=NaN;
catch
end

try
    colorData =
rot90(h5read(filename,'/Measurement/ColorData'));
    [sizeY,sizeX]=size(colorData);

    r=colorData(:,1:3:end);
    g=colorData(:,2:3:end);
    b=colorData(:,3:3:end);
    colorData = zeros(sizeY,sizeX/3,3);
    colorData(:,:,1)=r;
    colorData(:,:,2)=g;
    colorData(:,:,3)=b;
    colorData = colorData/max(max(max(abs(colorData))));
catch
end

cd ..
end

%% End of subfunction
```

C3. createFit_2.m

```
function [fitresult, gof] = createFit_2(x, y, z)

% Function to perform Least squares Plane fit
[xData, yData, zData] = prepareSurfaceData( x, y, z );

% Set up fittype and options.
ft = fittype( 'poly11' );
opts = fitoptions( 'Method', 'LinearLeastSquares' );
opts.Robust = 'LAR';

% Fit model to data.
[fitresult, gof] = fit( [xData, yData], zData, ft, opts );

end

%% End of subfunction
```

C4. STR_error.m

```
function [STR_Sa, STR_Sq, STR_Sz] = STR_error(heightmap)

[xp,yp] = size(heightmap(1).data);
files = length(heightmap);

sum_heightmap = zeros(xp,yp);

for i = 1:files
    sum_heightmap = sum_heightmap + heightmap(i).data;
end

avg_heightmap = sum_heightmap/files; % Average map

for i = 1:files
    z = heightmap(i).data - avg_heightmap; % Difference map
    diff_heightmap(i).data = z;

    Sa_error(i) = mean(nanmean(abs(z)));
    Sq_error(i) = sqrt(nanmean(z(:).^2));
    Sz_error(i) = max(max(z)) - min(min(z));
end

% Evaluation of surface topography repeatability in Sa, Sq,
Sz
STR_Sa = mean(Sa_error);
STR_Sq = mean(Sq_error);
STR_Sz = mean(Sz_error);

end

%% End of subfunction
```